Second Annual Report for RWM participation in DECOVALEX-2015 Tasks A and C1

Technical Report

RWM Coupled Processes Project

Second Annual Report for RWM participation in DECOVALEX-2015 Tasks A and C1

Alex Bond, Kate Thatcher, Neil Chittenden – Quintessa Ltd.
Chris McDermott, Andrew Fraser-Harris – University of Edinburgh

AMEC Report Reference	18040-TR-003
Client Reference	RWMD/03/020
Client Name	RWM
Issue Number	Version 3.0
Report Date	19/05/2015

Document Issue Record

Document title	RWM Coupled Processes Project: Second Annual Report for RWM participation in DECOVALEX-2015 Tasks A and C1
Project Reference	18040
Quintessa Reference	QRS-1612A-R2-v3.0

Purpose of Issue	Final version for approval
Security Class	Official

Issue	Description	Originator	Checker	Approver	Date dd/mm/yy
Draft 0.4	First draft for comment. (Unapproved)	AE Bond	C Watson	N/A	06/06/2014
Issue 1	For RWM Review	AE Bond	C Watson	A Guida	09/07/2014
Issue 2	Revised following RWM review	AE Bond	C Watson	A Guida	13/11/2014
Issue 3	Revised following RWM (Jon Martin) review	KE Thatcher	C Watson	A Guida	19/05/2015

Previous issues of this document shall be destroyed or marked **SUPERSEDED**.

This report has been prepared by AMEC Nuclear UK Ltd under contract to the Nuclear Decommissioning Authority (NDA), Radioactive Waste Management Directorate (RWMD) and forms part of an ongoing programme of research commissioned by NDA RWMD to underpin the long-term safety of a geological disposal facility for higher-activity radioactive wastes. Before it was published RWMD became a wholly owned subsidiary of the NDA (on 1 April 2014) called Radioactive Waste Management Limited.

The report has been reviewed by Radioactive Waste Management Limited. However, references to NDA and RWMD in the text have been retained as they are appropriate for the period when this research was being performed. The views expressed and conclusions drawn in this report are those of AMEC Nuclear UK Ltd and do not necessarily represent those of the NDA RWMD or Radioactive Waste Management Limited.

Conditions of publication

Bibliography

If you would like to see other reports available from Radioactive Waste Management Limited and the NDA, a complete listing can be viewed at our website www.nda.gov.uk, or please write to our Communications department at the address below.

Feedback

Readers are invited to provide feedback to the Radioactive Waste Management Limited on the contents, clarity and presentation of this report and on the means of improving the range of reports published. Feedback should be addressed to:

Head of Stakeholder Engagement and Communications
Radioactive Waste Management Limited
Building 587
Curie Avenue
Harwell Oxford
Didcot
OX11 0RH
UK

Email: rwmdfeedback@nda.gov.uk

Preface

Radioactive Waste Management (RWM), a wholly owned subsidiary of NDA, is responsible for implementing geological disposal of higher-activity radioactive wastes in the UK. RWM's research into geological disposal considers safety during waste transport to a disposal facility, during waste disposal operations, and once the facility has been closed.

RWM's Coupled Processes Project considers thermal, hydraulic, mechanical and chemical processes in situations where one of more of these processes strongly depends on another. In such situations, consideration of a single process in isolation would not be able to account for observations, and thus it is important to consider the interactions of the relevant processes. The project comprises three tasks:

Task A: Participation in DECOVALEX-2015 Case Study A.

Task C1: Participation in DECOVALEX-2015 Case Study C1.

Task 3: General Support to RWM on Coupled Processes

Tasks A and C provide for the contractor team to work with RWM on two case studies that form part of the DECOVALEX-2015 international applied research project. DECOVALEX – DEvelopment of COupled models and their VALidation against EXperiments – has been running continuously since 1992 in a series of six phases, and the current phase (2012-2015) encompasses modelling of thermal-hydrological-mechanical-chemical (THMC) process couplings based on results from *in situ* and laboratory experiments.

Task 3 provides for the contractor team to work with RWM to understand and document what work has been done on coupled processes as part of the UK programme, to understand approaches for treating coupled processes in performance assessments in overseas programmes, and to make recommendations for the RWM forward programme.

Work on RWM's Coupled Processes Project is being undertaken by a team of organisations that together have substantial experience of the UK programme for management of higher-activity radioactive wastes and the evaluation of coupled processes associated with geological disposal of these wastes.

AMEC is responsible for project management of the contractor team. Galson Sciences Ltd is responsible for managing the technical work programme and leading technical activities on Task 3, review of coupled processes in the UK programme and in overseas performance assessments, and advice on research requirements. Quintessa Ltd is responsible for managing the technical work programme and leading technical activities on Tasks A and C1, which involves participation in case studies A and C1 of the international DECOVALEX project on coupled processes.

Quintessa Ltd prepared this report with support from the University of Edinburgh (including the PhD student at the University of Edinburgh); it records work completed during the second year of the DECOVALEX-2015 project by the team funded by RWM. All of the work presented in the following sections has been presented and critically discussed in detail at DECOVALEX-2015 workshops.

Executive Summary

Radioactive Waste Management (RWM) is responsible for implementing geological disposal of the UK's higher-activity radioactive wastes. RWM's research into geological disposal considers safety during waste transport to a disposal facility, during waste disposal operations, and once the facility has been closed.

Coupled processes have been acknowledged by RWM and the wider international radioactive waste management community as being of potential major significance in the assessment of post-closure safety for geological disposal facilities (GDFs) for radioactive waste. The aim of RWM's Coupled Processes Project is to support RWM in addressing coupled process sets and understanding their potential significance to the assessments of post-closure safety that underpin the environmental safety case (ESC), site investigations, and design of a GDF in the UK.

RWM's Coupled Process Project comprises support for the contractor team to work with RWM on two case studies that form part of the DECOVALEX-2015 international applied research project on coupled processes, and a third task to provide general support to RWM on coupled processes.

This report provides an overview of the technical work completed by the RWM team during the second year of DECOVALEX-2015 under Task A (coupled hydraulic-mechanical behaviour of bentonite seals) and Task C1 (coupled thermal-hydraulic-mechanical-chemical evolution of single fractures). However it is not a general record of the progress made under Tasks A and C1, which is recorded in internal reports of the DECOVALEX project and made available publically through conference and journal publications. The report shows that good progress continues to be made against the DECOVALEX Task specifications, and the overall objectives of the project are expected to be met over the three-and-a-half year duration of DECOVALEX-2015.

Production of annual progress reports throughout the DECOVALEX-2015 project ensures that the work funded by RWM is presented in the open literature in a timely manner as the project progresses. This enhances transparency and enables the reader to understand the capabilities available to RWM in relation to the treatment of coupled processes in GDF-relevant studies.

Contents

List of Terms and Abbreviations

BBM	Barcelona Basic Model for swelling clays
Cam-Clay	A standard mechanical model for clays
Darcy Flow	Flow of a fluid through porous media where the flow rate is proportional to the pressure gradient
DECOVALEX	DEvelopment of COupled models and their VALidation against EXperiments
EDZ	Engineered Damage Zone – region around a sub-surface excavation where rock damage has occurred
FEBEX	Full-scale Engineered Barriers EXperiment at Grimsel, Switzerland
FLAC	Software for mechanical modelling
GDF	Geological Disposal Facility
HLW	High-level (heat generating) Waste
ILC	Internal Limit Curve. Function of the limit of elasticity used in the ILM.
ILM	Internal Limit Model. Candidate hydro-mechanical model for bentonite currently undergoing development and testing.
ILW	Intermediate-level (low-heat generating) Waste
Indurated	Hardened. In this report used in the context of clays becoming hardened over geological timescales.
LLW	Low-level Waste
IRSN	Institute for Radiological Protection and Nuclear Safety in France
MCC	Modified Cam-Clay – a standard mechanical model for clays
MX-80	A commercial formulation of bentonite-rich clay
MRWS	Managing Radioactive Waste Safely programme
MPF	Multi-Phase-Flow: QPAC module
Novaculite	Rock formation consisting dominantly of micro-crystalline quartz found in the Ouachita Mountains of Arkansas and Oklahoma and in the Marathon Uplift of Texas
Oedometer	Laboratory tool for loading soil samples and measuring deformation
OpenGeoSys	Open source coupled modelling code
OGS	OpenGeoSys
QPAC	Coupled-modelling code developed by Quintessa
Saturation	Fractional volume of pore space occupied by a given fluid.
Suction / Capillary Pressure	Difference in pressures between immiscible fluids in a partially saturated porous medium. The variation with saturation is termed the [Water] Retention Curve or Capillary Curve.

SEALEX	Long term engineered seal experiment at the Tournemire URL
SEM	Scanning Electron Microscope
Technological Void	A term from Task A referring to the gap between the seal and the containing structure caused by the limitations of technology when constructing the test
THMC	Thermal-Hydraulic-Mechanical-Chemical coupled processes
UoE	University of Edinburgh
URL	Underground Rock/Research Laboratory
Void Ratio	Ratio of voids volume to solid volume in a given rock or soil sample
Water Content	The mass of water divided by the mass of solid in a given volume of porous medium
Wood's Metal	Metal alloy with a low melting point of approximately 70°C

1 Introduction

1.1 Background and Objectives

As part of its Managing Radioactive Waste Safely (MRWS) programme, the UK Government issued a White Paper in June 2008 setting out a framework for implementing geological disposal of the UK's higher-activity radioactive waste (Defra *et al.* 2008). In 2014 a further White Paper was published outlining an updated approach to the siting of a potential disposal facility (DECC, 2014), reflecting learning from the previous siting process which ran until February 2013. Radioactive Waste Management (RWM), a wholly owned subsidiary of the Nuclear Decommissioning Authority (NDA), is responsible for managing the delivery of geological disposal of higher-activity radioactive wastes. Higher-activity radioactive wastes include high-level waste (HLW), intermediate-level waste (ILW), and the small fraction of low-level waste (LLW) that cannot be managed under the UK Government policy for the long-term management of the UK's solid LLW. In addition to these wastes, spent fuel (SF), separated plutonium (Pu) and separated uranium (U) may need to be managed through geological disposal.

Coupled processes involve situations where different classes of physical or chemical processes (e.g. thermal, hydraulic etc.) interact with each other to create emergent phenomena. This often adds considerable complexity to the system being considered, usually making the mathematical relationships strongly non-linear and requiring a multi-disciplinary approach. Coupled processes have been acknowledged by RWM and the wider international radioactive waste management community as being of potential major significance in assessing the post-closure safety of a geological disposal facility (GDF). In addition, the Government's Committee on Radioactive Waste Management (CoRWM) has commented on the research requirements associated with coupled processes (e.g. CoRWM 2009, paragraph A.74) and has questioned the sufficiency of the UK skills basis in this area (CoRWM 2009, paragraph 4.45). The issue of coupled processes has also been commented on by several other reviewers of the RWM work programme, and considerations about coupled processes are an important component of several of the "issues" identified within RWM's issues register (NDA, 2012), as follows:

- Engineered barrier resaturation.
- Long-term cement backfill evolution.
- Impact of coupled thermal, hydrogeological, and chemical processes.
- Evolution of the geosphere.

With this as background, the aim of RWM's Coupled Processes Project is to support its efforts in addressing coupled process sets and understanding their potential significance to the assessments of post-closure safety that underpin the environmental safety case (ESC). The Coupled Processes Project comprises three tasks:

Task A: Participation in DECOVALEX-2015 Case Study A.

Task C: Participation in DECOVALEX-2015 Case Study C1.

Task 3: General Support to RWM on Coupled Processes.

Tasks A and C provide for the contractor team to work with RWM on two case studies that form part of the DECOVALEX-2015 international applied research project. DECOVALEX – DEvelopment of COupled models and their VALidation against EXperiments – has been running continuously since 1992 in a series of six phases, and the current phase (2012-2015) encompasses modelling of thermal-hydrological-mechanical-chemical (THMC) couplings based on results from *in situ* and laboratory experiments.

The present phase of the DECOVALEX project (2012-2015) was launched in 2012. RWM is involved in Tasks A and C of DECOVALEX-2015:

- Task A focuses on the SEALEX project, which involves emplacement of a clay-based seal at the Tournemire underground research laboratory (URL). The objectives are to investigate the hydraulic performance of the seal for different chemical and physical forms of the clay; the impact of construction on hydraulic properties; and the impact of incomplete saturation on swelling pressure. The task considers a series of 'steps' starting with smaller, laboratory-based experiments, before moving on to modelling the full-scale experiment. The steps involve attempting to understand and represent experimental results using numerical models, and then using those models in blind predictions at the laboratory and field-scale.

- The objective of Task C (specifically Task C1) is to examine THMC process couplings in single fractures in low permeability, low porosity ('high strength') host rocks, with a data set based on two historical laboratory experiments. The experiments consist of single fractures where mechanical loading, groundwater chemistry and thermal characteristics were varied, and water outflow rates or pressure gradients, out-flowing geochemistry, and mechanical load response were measured. Models produced as a result of this work are some of very few attempts at replicating THMC coupling in fractured media (e.g. Taron *et al*. 2009).

Task A is of interest to the UK programme because it deals with understanding the practicalities of designing, installing and the early evolution of clay-based sealing structures. Depending on the GDF concept being considered, such sealing structures can be very important in the role of limiting gas and water migration post-closure and hence have important safety functions, especially in low-permeability host rocks. For the seals to perform as designed, they will typically have to reach a certain stress and/or water hydration state within a specified timeframe, therefore being able to successfully predict the hydro-mechanical evolution of these seals may be an important line of evidence to support a sub-set of safety functions.

Task C1 is a much more fundamental investigation, primarily concerned with whether the current phenomenological understanding of THMC fracture evolution is consistent with the available experimental data. If not, the role of the task is to attempt to use modelling to help improve that process-based understanding by testing a range of process and conceptual models. In the context of the UK programme, this work is primarily relevant to the potential evolution of newly created fractures in Engineered Damage Zones (EDZs) for crystalline 'high strength' rock formations and the phenomena relating to a potential change in permeability for those fractures. The work may also be of relevance to the properties of natural fractures and the potential impact of temperature changes and the consequences of groundwater chemistry evolution, as a result of the construction of the GDF. Both of these issues have the potential to impact on the flow of water to and from a GDF, and hence

impact transport of radionuclides away from the facility, as well as general evolution of the facility itself, for example resaturation times for buffer, backfill, seals and voids.

1.2 Approach and Scope

This report provides an overview of the technical progress made through the second year of DECOVALEX-2015 (April 2013 to April 2014). The information presented here represents the status of the work as presented at the DECOVALEX workshop hosted by IRSN in France, April 2014. It should be noted that the report does not attempt to present a chronological progress report, but rather discusses the present status of work against the separate project components ('Steps') under each Task at the time of writing. The report also only discusses the work of the RWM team and does not attempt to discuss the work from other contributors to the respective Tasks. To minimise duplication and to keep the report as brief as practicable, the report is incremental on the first year annual report (Bond *et al*., 2014) and the reader is expected to have read the first annual report in order to have the full context necessary to understand the second year of work. However, the general descriptions of the tasks from Bond *et al*. (2014) are retained to assist the reader.

It should be noted that the two tasks are, at present, relatively independent in terms of their technical work and so are discussed separately in the following sections.

1.3 Report Structure

The remainder of this report is structured as follows:

- Section 2 provides an overview of Task A and the technical work conducted under it, specifically the continuing work under Steps 0 and 1 and the new experimental data under Step 1. This is then followed by an outline of the expected way forward for the following twelve months.

- Section 3 provides an overview of Task C1 and the technical work conducted under it, primarily continuing work on Steps 1 and 2. This is then followed by an outline of the expected way forward for the following twelve months.

- Section 4 provides a summary of progress and the main themes for work going forward and highlights any issues of potential significance to RWM.

2 Task A – SEALEX Experiment

2.1 Task Overview

2.1.1 SEALEX Experiment

The SEALEX experiment is a field-scale investigation into geological disposal facility (GDF) engineered seal performance, currently underway at the Tournemire Underground Rock Laboratory (URL). The Tournemire URL is a railway tunnel constructed approximately 125 years ago through the Larzac Plateau in the south of France close to Rochefort and Tournemire (see Figure 2-1 and Figure 2-2). No longer in use as a railway tunnel, since 1992 the tunnel has been owned and operated by IRSN (a French public authority which acts as a public service expert in nuclear and radiation risks), as an experimental facility.

The URL is primarily constructed in the Toarcian argillite, an indurated clay formation consisting of shales and marls, with a very low permeability to saturated water flow. The formation shares many characteristics of other indurated clays being considered for radioactive waste disposal, such as the Callo-Oxfordian argillite in France and the Opalinus Clay in Switzerland, being of low intrinsic permeability (~10^{-21} – 10^{-18} m^2), significant porosity (~9%) and with a strong tendency to show hydraulic 'self-sealing' characteristics post excavation.

The SEALEX experiments are being conducted in a new drift (Figure 2-3) away from the main tunnel.

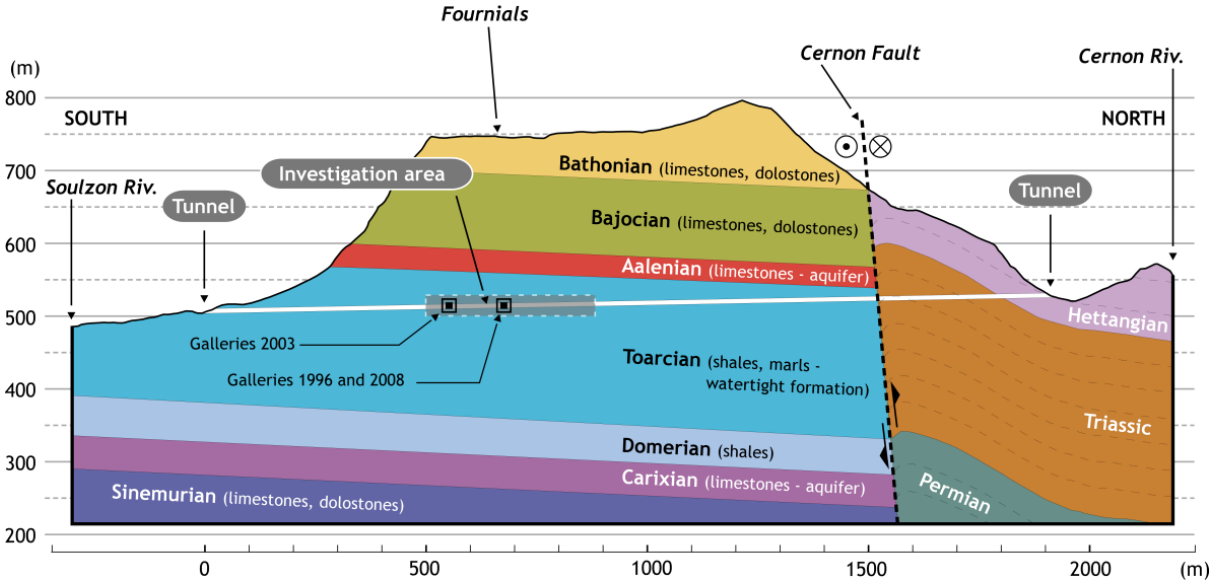

Figure 2-1 Geological section along the line of the Tournemire URL tunnel (IRSN, 2012).

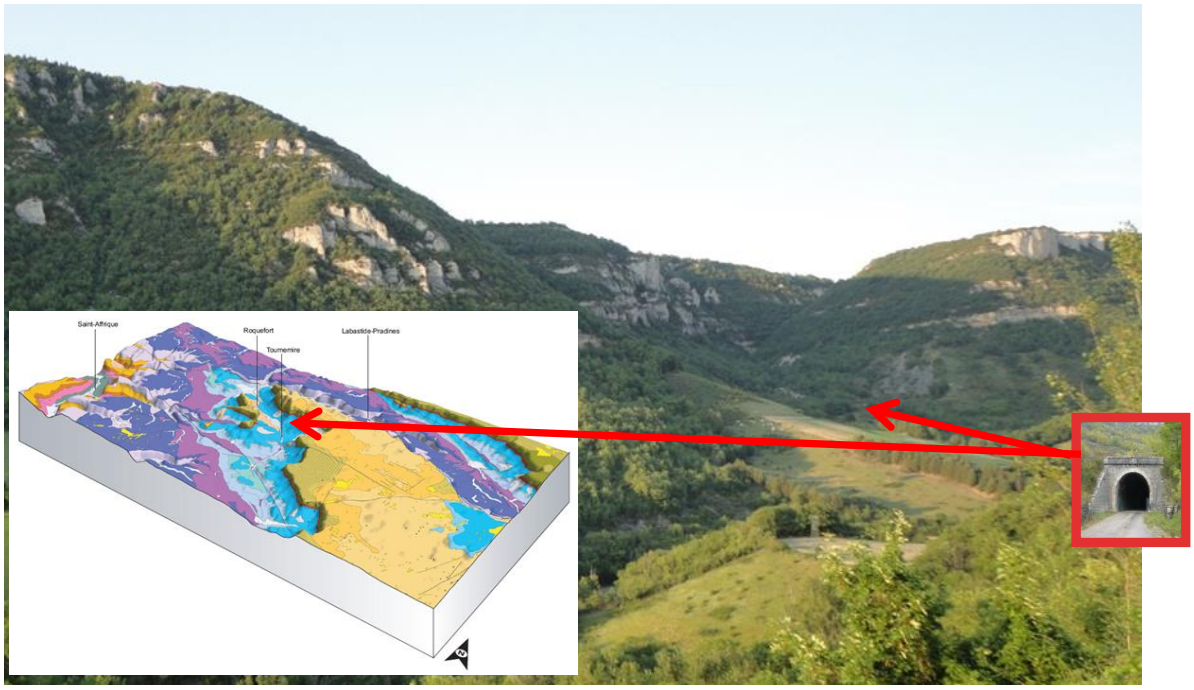

Figure 2-2 View of the southern side of the tunnel and (inset) the geology exposure of the Larzac Plateau, southern entrance marked in both cases (IRSN, 2012).

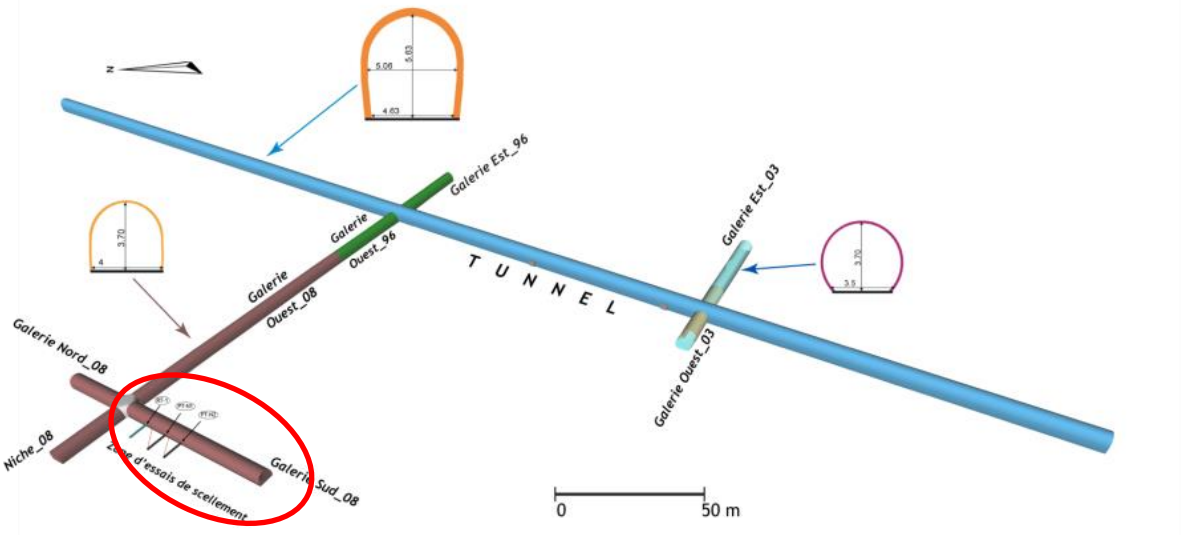

Figure 2-3 View of the Tournemire URL with the SEALEX experimental gallery marked with the red ellipse (IRSN, 2012).

The main motivations for the experiment are as follows:

- Evaluation of the main perturbations caused by the installation of the seals and their influence on the radioactive waste confinement properties of the other geological disposal components, in this case primarily the host rock.
- Evaluation of the technical feasibility of seals with respect to their:
    - Safety functions
    - Expected performance level (e.g. overall hydraulic conductivity).

The desired outcome of the experiment is to be able to understand and predict the overall performance of the clay seals, over the long-term, for a range of different evolution and installation conditions:

- Using the reference seal design and expected evolution
- For different technological choices (e.g. bentonite mix, installation method)
- In altered situations (e.g. loss of mechanical confinement).

The experimental approach involves the installation of a series of mocked-up seals in 60 cm diameter, 5 m long boreholes drilled horizontally into the sides of the gallery. The seals were chosen to be this size in order that they are large enough to be considered 'field scale' and also because they are of a similar size and geometry to the seals currently considered in the ANDRA concept for plugging the end of HA (high activity, heat generating waste) horizontal deposition holes.

Two configurations of seal installation and instrumentation are considered in the experiments – the so-called 'Reference Test' and the 'Performance Test'. The purpose of reference tests is to examine the interaction of the bentonite seal with the argillite host rock using conventional wired sensors. In contrast, following flooding of the 'technological voids' (engineered gaps) around the seals with water, and enhanced resaturation with a constant supply of water at the tunnel end of the seal, the performance tests were designed to enable the application of an induced hydraulic gradient across the seal in order to test the hydraulic performance of the installed seal. To this end, the performance tests use wireless sensors to avoid disturbing the installed seal, while the reference tests use a higher number of wired sensors.

For both tests the seals are isolated hydraulically and mechanically from the main tunnel drift via the use of hydraulic packers and fixed concrete, steel and epoxy confining structures (Figure 2-4, Figure 2-5). Initial resaturation of both types of test is achieved through flooding of the annular void around the seal with water (the void is required in order to get the seal in place) and then supplying water through one or both axial faces of the seal. The permeability of the intact host rock is such that natural resaturation would take too long for experimental purposes, hence the need for artificial resaturation. For the performance tests, once water saturation has advanced sufficiently, the hydraulic testing of the seal can then take place.

The original installation plan is shown in Figure 2-6. Monitoring of the installed experiments is expected to last at least a decade from the installation date.

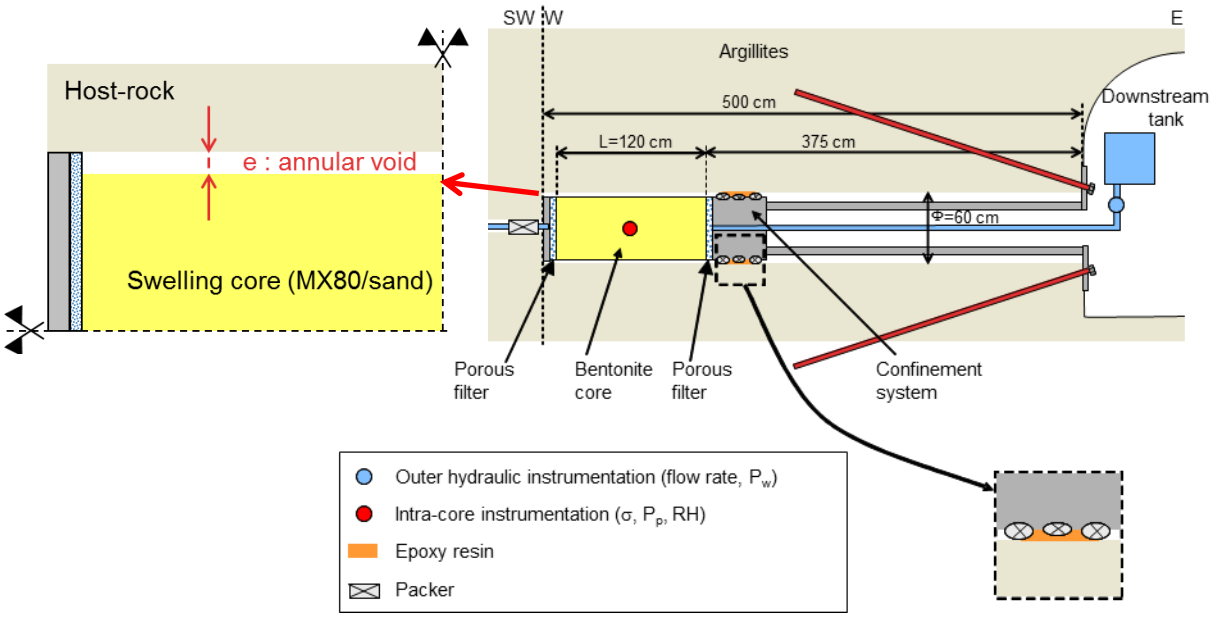

Figure 2-4. Schematic illustration of the experimental arrangement for a single seal (IRSN, 2012).

Reference Test configuration

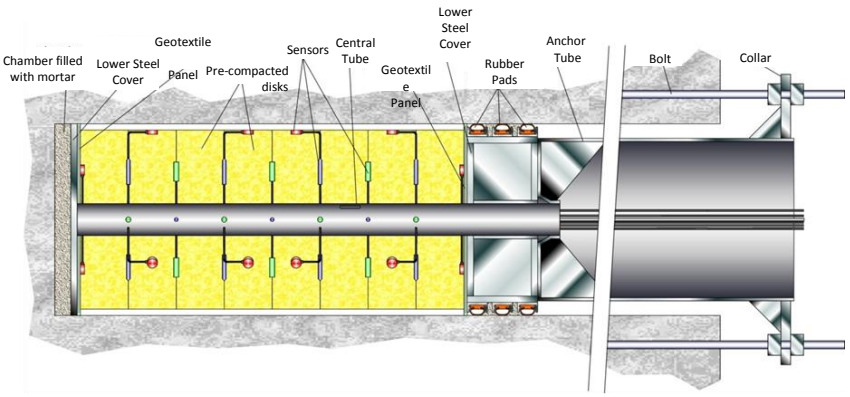

Performance Test configuration

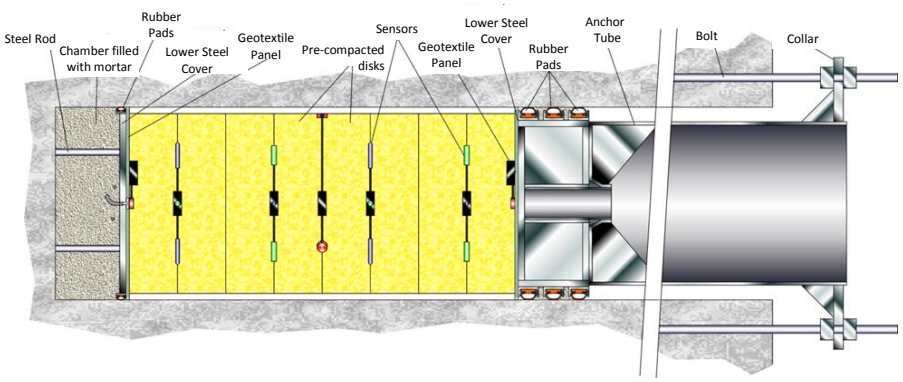

Figure 2-5. Arrangements for the reference tests (top) and performance tests (bottom) (modified from IRSN, 2012).

	Reference Tests	Performance Tests	Intra-core geometry Core conditioning Composition (MX80/sand)	Core view	Altered conditions	Emplacement date
Base case	RT-1	PT-N1	Monolithic disks Precompacted (70/30)		No	12/2010 06/2011
Variations / Base case	-	PT N2	Disks + internal joints (4/4) Precompacted (70/30)	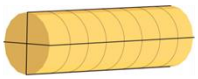	No	12/2011
	-	PT A1	Monolithic disks Precompacted (70/30)		Confinement loss	06/2012
	-	PT-N3	Pellets/powder In situ compacted (100/0)		No	01/2013
	-	PT-N4	Pellets/powder In situ compacted (100/0)		Confinement loss	*09/2013*

Figure 2-6. Experimental schedule for the SEALEX experiment (IRSN, 2012). Black text indicates base case experiments and red text show variant experiments.

One further experiment was also conducted; WT-1, the water injection test. This experiment hydraulically seals and then injects water directly into the end of one of the mocked-up deposition holes, monitoring the injected quantity of water and pressure response between the confinement system and the host rock; no bentonite is involved in this test. The data can then be interpreted to derive field-scale hydraulic properties for the argillite. The determination of such hydraulic properties using these experimental results (intrinsic permeability and potential variation with time, storativity) is one of the exercises within Task A, with particular interest in evidence for temporal evolution of hydraulic properties.

2.1.2 Task A Structure

The present structure of the task is itemised below. In essence, the task is divided into a series of steps, each of which represents a significant change of emphasis or increase in complexity. The structure of the steps is specified such that participating teams can build experience and improve modelling tools on more constrained data before culminating in attempting to model the large-scale, complex cases in the final part of the project. The task structure (as administered by IRSN) is as follows.

- **Step 0**: Modelling of the bentonite/sand mixture hydro-mechanical (HM) behaviour, parameter identification from various laboratory 'unit' tests:
    - Water retention curve (free swelling and confined)

  - 1D confined infiltration test
  - Oedometer swelling and compaction testing

- **Step 1**: Modelling of the 1/10th mock-up (laboratory test). Blind prediction using model & parameters obtained in Step 0 (Sections 2.2 to 2.4).
- **Step 2**: Modelling of the hydraulic behaviour of the rock surrounding the bentonite-sand plug, based on results of the WT-1 in situ test (Section 2.5).
- **Step 3**: Modelling of the in situ PT-N2 test.
- **Step 4**: Modelling of the in situ PT-A1 test.

It should be noted that Steps 3 and 4 have now been merged into a single Step 3, and only the PT-A1 test will be considered.

The RWM team is one of 5 teams contributing to the progress of the task. The presence of such a wide range of experience, approaches and expertise working on the same task in a cooperative manner is a key benefit of the DECOVALEX-style project approach in that it maximises the opportunity for genuine progress in addressing such complex cross-disciplinary problems. The current participants under Task A are:

- IRSN (internal technical team and also managers of the task);
- CNSC (Canada), funded by IRSN;
- Quintessa and the University of Edinburgh, funded by RWM;
- UGN (Czech Republic), funded by RAWRA; and
- US NRC (internal technical team).

This document only reports the work of the RWM team, but some comments will be made on other teams' approaches where appropriate.

The current schedule for this work is shown in Figure 2-7.

A PhD programme of work has been designed to complement the RWM effort in supporting Task A, but will be largely independent of the milestones shown in Figure 2-7. It is intended that key outputs from the PhD will be incorporated into the Task A work as appropriate and presentations of progress will be given to the DECOVALEX project at key points throughout the PhD programme.

	Apr 2013	Nov 2013	Apr 2014	Nov 2014	Apr 2015	Nov 2015
Step 0						
Step 1						
Step 2						
Step 3						

Figure 2-7. Current schedule for Task A, Decovalex-2015. The red line indicates end of April 2014, which is the point of progress in the project reported herein.

2.2 Year 1 Status Summary and Approach

At the end of year 1, QPAC (Quintessa, 2013) and OGS (Kolditz *et al*. 2012) models looking at different aspects of Step 0 had been built by the RWM team and two candidate models, using a variant on the Modified Cam Clay (MCC) mechanical model[1], had been developed in QPAC to give blind predictions for Step 1. Work had also been conducted in parallel by the University of Edinburgh PhD student in considering alternative, simpler hydro-mechanical formulations that might have similar or better predictive power than the 'standard' approaches seen elsewhere in the literature (Bond *et al*., 2014).

A key conclusion from the work in year 1 was that the limited data available under Steps 0 and 1 limited the testing of certain aspects of alternative models. As such, significant effort should be put into implementing and understanding the Barcelona Basic Model (BBM)[2] form of models, in order to be able to benefit from model parameterisation in the literature. This would help the RWM team understand other modelling approaches, help underpin potential novel methods and also build a capability for BBM-like modelling.

Again it is emphasised that all of the work presented in the following sections has been presented and critically discussed in detail at DECOVALEX-2015 workshops, constituting a form of peer review sufficient for an annual progress report. Full journal publications for most of this work are expected over the coming two calendar years, which will give an opportunity for additional peer review. The material presented is very much work in progress, but once complete, will be published as part of the DECOVALEX work or independently.

[1] This is a variant of the Cam-Clay model optimised for numerical implementation. It addresses both elastic and plastic deformation of soils (particularly clay) under three dimensional loads.
[2] The BBM is essentially an extension of the Modified Cam-Clay model to include a fluid suction dependence on many of the Cam-Clay key properties. The BBM also includes specific formulations for water flow and suction changes under plastic volume change.

2.3 Further Work on Step 1

2.3.1 Post blind-prediction update

Following the DECOVALEX workshop in Korea, 2013, it became clear that of the teams (RWM and IRSN) that submitted blind predictions for Step 1, only the RWM results were genuinely blind. The results of the blind and calibrated comparison for the various teams are given in Millard *et al*., (2014) and are not discussed here further. The key point was that the two sets of QPAC results were intended to bracket the expected behaviour with the MCC results (as shown below) expressing the upper plausible range of stress and water uptake behaviour.

With this additional interpretation in mind, the MCC model used in the blind prediction was re-calibrated using the Step 1 data. The results of the calibration are given in Figure 2-8 to Figure 2-10. The comparison is clearly better than the blind prediction; however there remains some difficulty in getting the required response in Phase 2/3 (Phase 1 being the fully confined phase; Phase 2 considering free vertical swelling; and Phase 3 being the second confinement period at 20% vertical strain). The only changes to the parameterisation were to use the porosity-dependent permeability from the infiltration test in Step 0 and to adjust the parameterisation of the free suction curve to the following

$$\varphi_f = F\left(\exp\left(a - b(W - \alpha)\right) + \exp(c - d(W - \alpha))\right) * 1 \text{ [MPa]} \quad (1)$$

where φ_f is the free suction (MPa), F is the mass fraction of bentonite (kg/kg), W is the water content by mass (mass of water per mass of solids - kg/kg) and a-d and α are fitting parameters (all dimensionless) with the following values.

a=8.07, b=32, c=-0.5, d=1.5, $\alpha = 0.03$ (2)

The key aspect of the experimental results that was not captured by the MCC model was the very high elastic response after unloading. Such a response is a product of one potential interpretation of the Step 0 zero suction oedometer data, which were the only mechanical data at the 'correct' 1.97 Mg/m^3 initial dry density. The very large recovery of void ratio in unloading (unlike the other higher suction tests) can be ascribed either to dominant elasticity in loading and unloading, or dominant plasticity on loading and the uptake of water (and hence swelling) as unloading proceeds, i.e. the deformation can be either elastic or plastic dominated. Comparing these results it appears that plasticity and water uptake is the dominant mechanism for recovery and the MCC and other future models could usefully be adjusted to take this into account, rather than the elastically dominated model and low suctions that had been assumed. This result illustrates the potential for ambiguity in oedometer data where the transient associated with each loading and unloading step has not been captured.

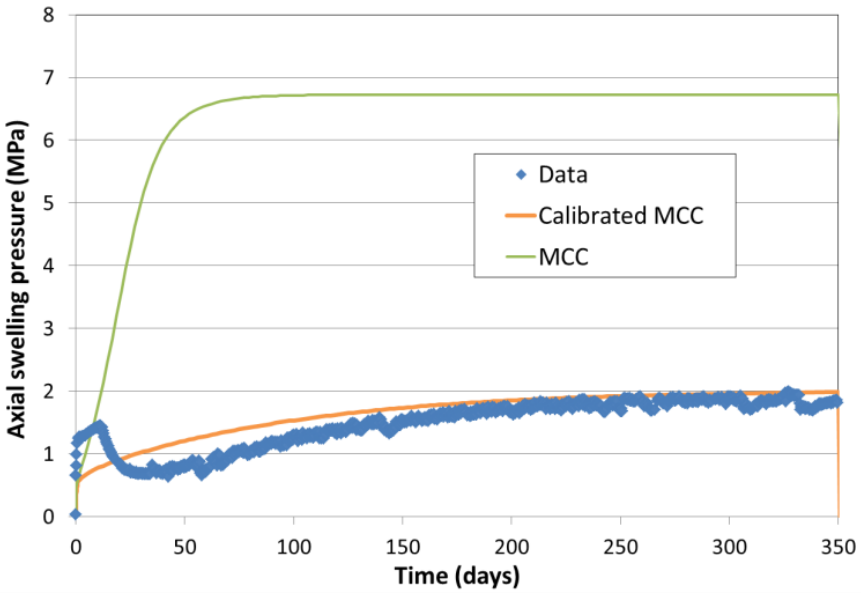

Figure 2-8. Comparison of the predicted (MCC - green) and calibrated (Calibrated MCC - red) axial swelling stress for the QPAC MCC model in Phase 1

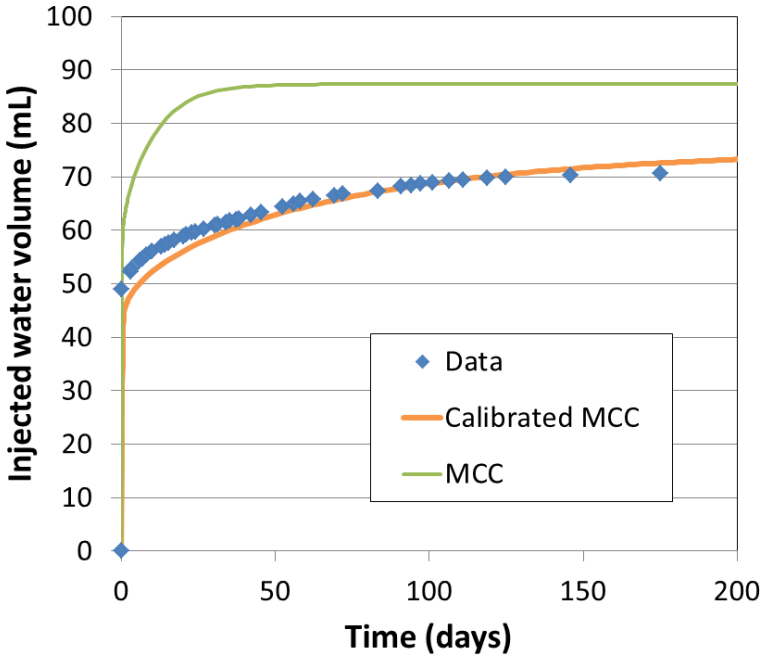

Figure 2-9. Comparison of the predicted (MCC - green) and calibrated (Calibrated MCC - red) water uptake in Phase 1.

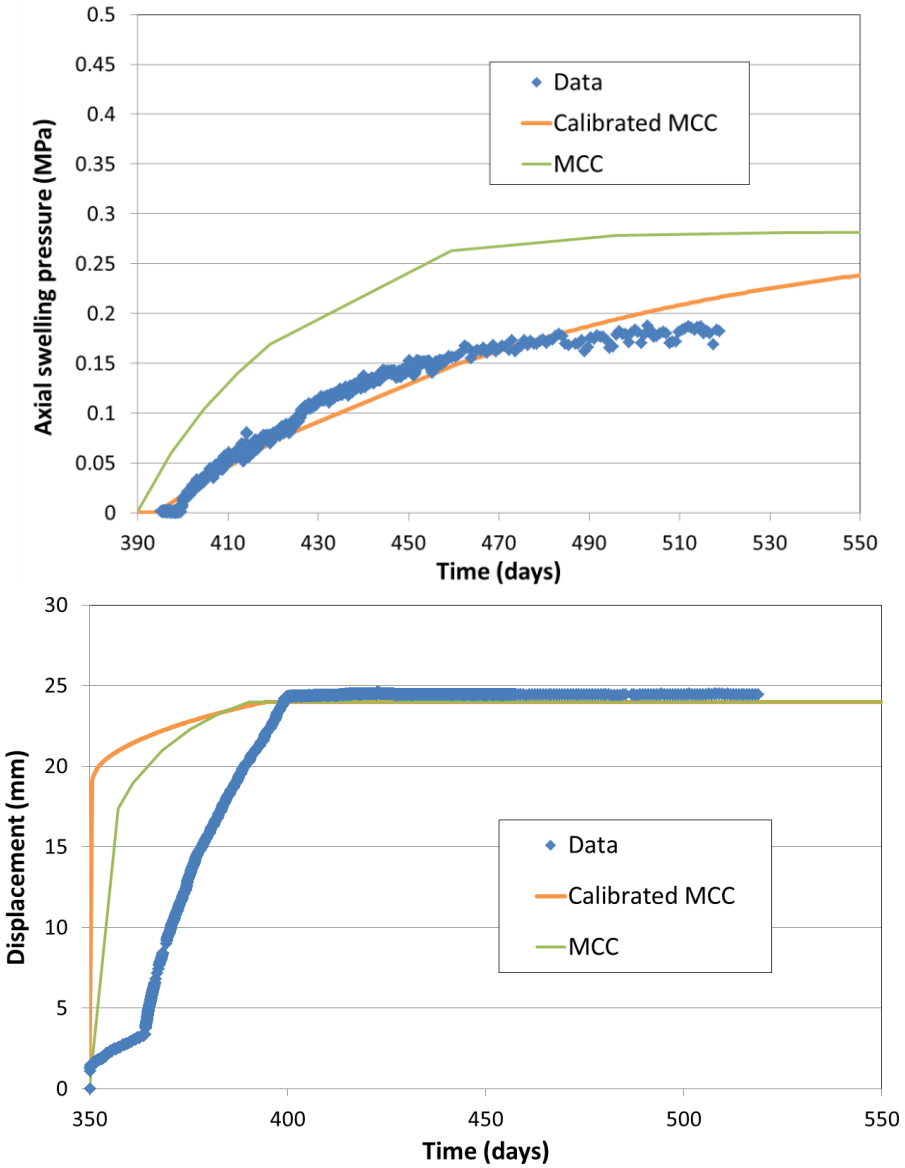

Figure 2-10. Phase 2 and 3 axial swelling pressure (top) and axial displacement (bottom) for the calibrated MCC model (Calibrated MCC - red) and the blind prediction (MCC - green).

2.3.2 Implementation of the BBM in QPAC

Following the initial work on the MCC model, while the model gave broadly correct behaviour, it was recognised that the lack of data available within the task was potentially a major limitation to moving forward. While the MCC could doubtless be improved, especially through the adjustments to the elasticity model to fit both the Step 1 and Step 0 data, it was agreed that time would be better spent exploring other options.

Therefore it was decided to investigate the Barcelona Basic Model (BBM) more thoroughly and attempt an implementation in QPAC to take advantage of the various descriptions of implementations and parameter sets in the literature. Another driver was that, while certainly not perfect, the IRSN BBM model perhaps gave the best overall results post-calibration for Step 1 (Millard *et al*., 2014), and hence it would be sensible to investigate their approach. It should be noted that the implementation of the BBM in QPAC was through the definition of input files and did not involve any development of the software itself.

The implementation of the BBM in FLAC (Rutqvist *et al*., 2010; 2011) was particularly useful as it gave a recent account of the practicalities of implementing such a model, and appears to be the only example of a coherent BBM implementation in 3D within the published literature. Performing this work would also act as a learning exercise to better understand the background and limitations of the BBM approach. It was noted that across the range of papers examined, various changes to the BBM were made depending on the application, leading to potential issues of consistency in comparing BBM-like models.

Using Rutqvist *et al*. (2011), a full implementation was created and tested in QPAC, termed the 'qBBM'. For brevity, the details of the implementation are not included here, however some important aspects bear discussion that came out through the testing process. A full journal publication of this work is expected in due course.

The BBM is formulated using an incremental method to evaluate the elasto-plastic deformation. This is a well-established approach, discussed in great detail by Biot (1965). In QPAC, while it is straightforward for the plastic and swelling components of strain to be expressed incrementally using the visco-plastic flow formulation advocated, it is more convenient and efficient to express the elastic component in an integral fashion (Bond, 2013a), i.e. for the elasticity in QPAC:

$$\bar{\sigma} = \bar{\bar{S}}(\sigma, \varepsilon, \ldots)(\bar{\varepsilon_e} - \bar{\gamma}) \tag{3}$$

where $\bar{\sigma}$ is the stress vector (MPa), $\bar{\bar{S}}$ is the non-linear stiffness tensor (MPa) which can be a function of stress and strain, $\bar{\varepsilon_e}$ is the elastic strain vector and $\bar{\gamma}$ is the vector of the sum of the non-elastic strain components (plasticity and swelling). In the BBM approach a series of steps, or increments, is solved for at each timestep, until equilibrium is reached. Expressed as above, and considering partial derivatives, one would expect the elastic increments to take the form:

$$d\bar{\sigma} = d\bar{\bar{S}}(\sigma, \varepsilon, \ldots)(\bar{\varepsilon_e} - \bar{\gamma}) + \bar{\bar{S}}(\sigma, \varepsilon, \ldots)(d\bar{\varepsilon_e} - d\bar{\gamma}) \tag{4}$$

where d denotes a small increment. However the BBM elastic increments are of the form of

$$d\bar{\sigma} = \bar{\bar{S}}(\sigma, \varepsilon, \ldots)(d\bar{\varepsilon_e} - d\bar{\gamma}) \tag{5}$$

although, following normal soil mechanics conventions, they are expressed in terms of *p*, *q*, stresses and bulk (*K*) and shear modulus (*G*) as follows:

$$d\varepsilon_{p,e} = \frac{1}{K^*} dp, \quad d\varepsilon_{q,e} = \frac{1}{3G} dq \tag{6}$$

$$d\varepsilon_{p,T} = d\varepsilon_{p,e} + d\varepsilon_{p,P} + d\varepsilon_{p,s} \tag{7}$$

$$d\varepsilon_{q,T} = d\varepsilon_{q,e} + d\varepsilon_{q,P} + d\varepsilon_{q,s} \tag{8}$$

where p and q are the volumetric and deviatoric stresses respectively (MPa). Subscripts *T*, *e*, *P* and *s* denote total, elastic, plastic and swell components of strain (ε) respectively, while subscripts *p* and *q* denote the volumetric and deviatoric components of strain respectively.

Clearly the BBM formulation uses a simplified form where the elastic increments associated with the moduli change (and hence the stiffness tensor) are neglected; these components are not neglected in the qBBM integral form. Further evidence of the consequences of this simplification is available from Houlsby (1985), and under small strains the impacts of these missing components will be small. As expressed in '*p*' '*q*' space the key differences between the BBM-FLAC and qBBM models are illustrated schematically in Figure 2-11. Essentially, as strain accumulates, most especially plastic strain which tends to be quite large, the two models deviate giving rise to different p-q gradients under loading and unloading in the qBBM. In contrast the BBM shows the same p-q gradient for both loading and unloading paths when plastic strain is not being incremented. The behaviours of the two models are identical if the bulk modulus is kept constant, and this was demonstrated through simple qBBM - FLAC benchmarking. Experimental data of the type that can be plotted in p-q space are limited, but there is some evidence of p-q lines changing gradient (Rutqvist *et al.*, 2011).

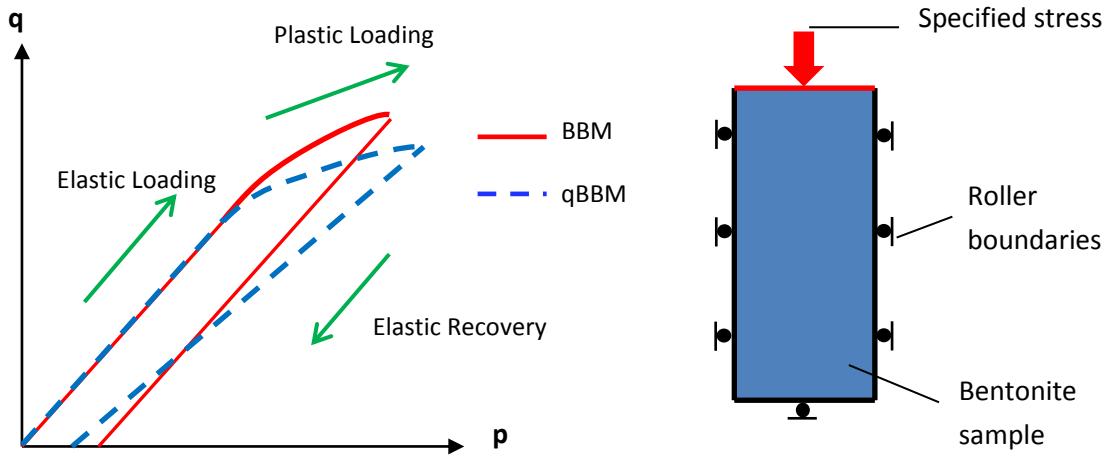

Figure 2-11. Illustration of the effect of the integral method versus the conventional BBM approach for a simple oedometer test in p-q space.

A further issue is that the BBM elastic model implies non-zero strain at zero stress and a very small bulk modulus at low strains, neither of which seems physically plausible when expressed as an integral problem. Furthermore, when expressed in an integral form, the BBM elastic model is extremely unstable, tending to infinity at very low strains, dropping to a minimum value and then increasing at larger strains. For this reason an alternative bulk modulus model was implemented that approximates the BBM and is very similar to the form of model used in the MCC and was found to give a good fit to the Step 0 oedometer data; both the 'true' BBM bulk modulus model and a series of alternatives that all approximate the BBM model are available in the qBBM implementation.

In terms of the hydraulics, the BBM and qBBM were defined to be functionally identical. It should be noted that the key difference between the qBBM and MCC approach used (Bond *et al*., 2014) is that the suction is a function of only the notional water saturation and the porosity (and hence dry density) of the bentonite. This is a more conventional soil mechanics approach, but it means the hydraulic parameterisation is completely independent of the mechanical parameterisation, despite evidence to the contrary (e.g. Wang, 2012). Overall the hydro-mechanical qBBM model, like the BBM, requires 21 or more free parameters (depending on the options chosen) to implement a single model.

Literature searches also revealed a disappointingly large range of parameterisation using the BBM for apparently similar bentonites (e.g. Rutqvist *et al*., 2010, 2011; Kristensson and Åkesson, 2008). This suggests that, for the data available, the BBM tends to be over-parameterised (i.e. functionally identical model responses can be obtained for different combinations of parameter values) and possibly dependent on the details of the particular variant of BBM being used in that modelling study and the experiment used to estimate the parameterisation. This potentially leads to issues whereby the calibrations of models to the available data are consistent, but different behaviours might be seen under different conditions, e.g. longer time scales or different loading scenarios.

The qBBM model was initially calibrated to the Step 0 oedometer data and infiltration test data. Then a further calibration round was performed to the Step 1 data. The key results are given in Figure 2-12 to Figure 2-14. These results were presented and discussed at the DECOVALEX Mont Terri meeting in November 2013.

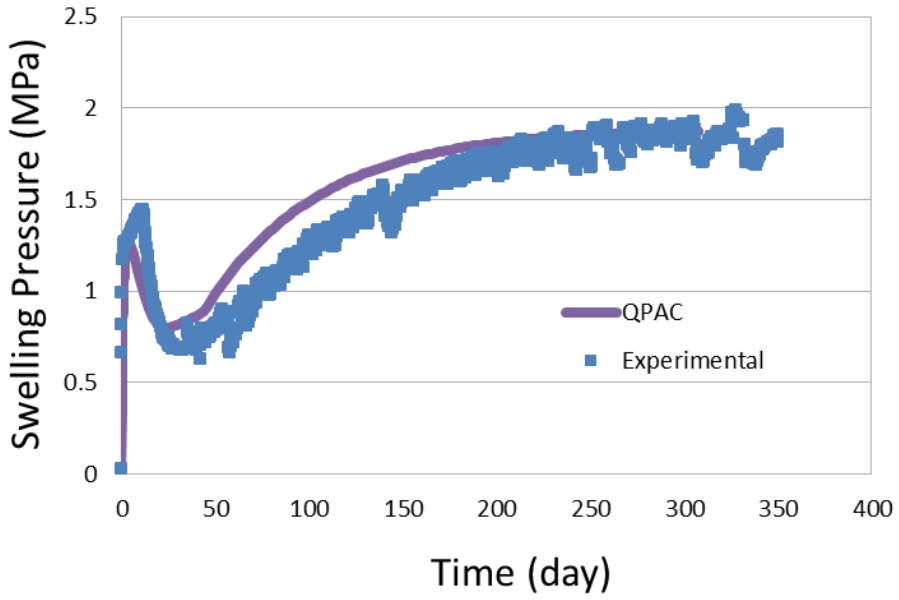

Figure 2-12. Comparison of axial swelling pressure versus the QPAC qBBM model for Step 1 during Phase 1.

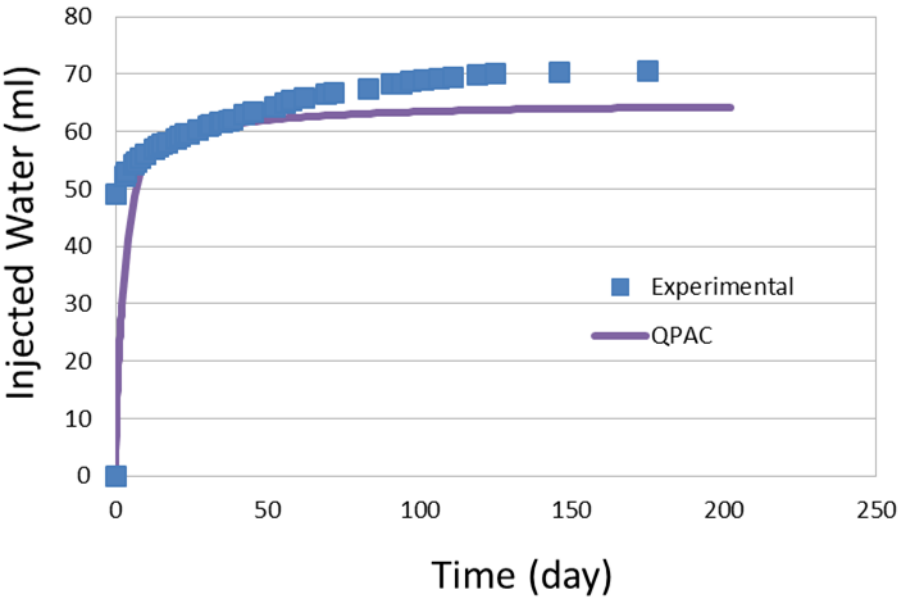

Figure 2-13. Comparison of injected water data versus the QPAC qBBM model for Step 1 during Phase 1.

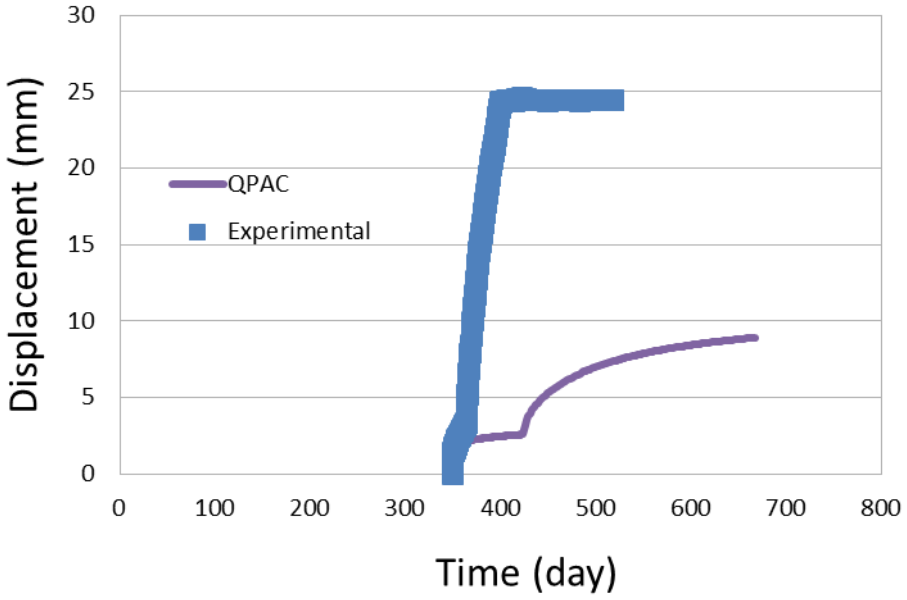

Figure 2-14. Comparison of axial displacement data versus the QPAC qBBM model for Step 1 during Phases 2 and 3.

The key observation was that it was impossible, consistent with the IRSN BBM results, to reproduce both the Phase 1 and Phase 2/3 behaviour well. Phase 1 data are reproduced well, capturing the 'softening' of the sample as the bentonite swells into the annulus. The key area for improvement is in the Phase 2/3 response where the initial elastic response due to unloading is correct, but the modelled system does not re-hydrate quickly enough (Figure 2-14). It was interesting to note that the IRSN BBM model has a slightly better representation of this phase – see Millard *et al*. (2014). In discussion with IRSN, it was revealed that they had made a number of non-standard changes to their model, mainly in relation to the swelling and permeability model, which led to the introduction of further free parameters. There is now the opportunity to represent these additional non-standard changes to the BBM in qBBM - however, there is a danger that these changes are creating ever more complexity and semi-arbitrary fits that have little to do with the physical and chemical behaviour of bentonite. On the other hand, however, the adjustments may be useful to inform future models. As such, it was decided that further development of the qBBM would be halted and more thought given to reducing the number of independent free parameters and producing a more convincing physical model of the system, following the initial work done by the University of Edinburgh PhD student (Bond *et al*., 2014)

Overall, development of a version of the BBM in QPAC has been extremely useful in generating an additional capability to investigate bentonite hydro-mechanical behaviour The work has also helped in understanding the strengths and weaknesses of the BBM approach, which is cited in the scientific literature sufficiently frequently that it could be regarded as the 'standard' bentonite hydro-mechanical model. However, given some of the uncertainties that have been highlighted and the IRSN experience of applying the BBM to SEALEX, on-going modification and development of the BBM (and related models) is likely to be needed if

detailed hydro-mechanical models are to be employed to demonstrate the required safety functions of bentonite within a GDF programme.

2.3.3 An alternative approach – the Internal Limit Model

2.3.3.1 Context

As discussed in the previous sections, hydro-mechanical modelling of bentonite in QPAC has been undertaken using standard models from the literature (MCC and BBM). This section proposes a new approach to modelling bentonite which has been implemented in QPAC and is based on observations of the swelling behaviour of bentonite. The model that is proposed and described here is called the Internal Limit Model (ILM).

The principal motivation behind the approach outlined here is to develop a simpler model for the bentonite hydro-mechanics where the parameterisation can be more closely tied to the macroscopic experimental observations. The approach also attempts to link more closely the suction behaviour of the bentonite, mechanical deformation and the swelling pressure that can develop under hydration. If successful, such an approach would reduce the amount of experimental data needed to parameterise a bentonite system and potentially lead to a more robust hydro-mechanical model as a result.

The following sections outline a series of steps that together give rise to the ILM. The model is initially motivated by a series of observations on swelling pressure and bentonite dry density (Section 2.3.3.2) which are used to relate these mechanical processes to the suction behaviour of the bentonite (Section 2.3.3.3). These correlations with the initial observations are used to suggest a relatively simple mechanical and swelling model (Section 2.3.3.4) and an appropriate hydraulic model (Section 2.3.3.5) which are coupled together to give a hydro-mechanical model that reflects the macroscopic physical observations, but with a considerably simpler parameterisation than adopted for the qBBM and MCC models. This model also uses the experimental data on dry density and swelling pressures directly in the parameterisation, greatly simplifying the calibration process.

2.3.3.2 Observations

The data from DECOVALEX-2015 Task A are taken from PhD work by Wang (2012), in which experiments on MX-80 bentonite in mixtures with sand and claystone, as well as pure bentonite, were performed. A number of interesting results arise from this work, alongside the data that are being used in Task A.

Wang *et al*. (2012) report work on the swelling behaviour of a bentonite/claystone mixture, where it was found that the swelling pressure depends on the final dry density of the mixture. Furthermore, this result is generalised such that for different mixtures of bentonite and sand/claystone (and different initial water content), the swelling pressure depends on the final dry density of the bentonite component of the mixture (Figure 2-15). The swelling pressure was found to be independent of the deformation or swelling history of the sample. There is clearly scope for minor calibration for individual bentonites, but it gives an extremely useful starting point.

In Wang *et al*. (2012), the swelling pressure as a function of the bentonite dry density is defined as:

$$P_{swell} = \alpha \exp(\beta \rho_{db}) \quad (9)$$

where ρ_{db} is the bentonite dry density (kg/m^3) and α and β are empirical constants. Wang *et al*. (2012) define ρ_{db} as follows:

$$\rho_{db} = \frac{M_b}{V_T - V_{nb}} \quad (10)$$

where M_b is the mass of bentonite (kg), V_T is the total volume of the sample and V_{nb} is the volume of the non-bentonite solids (including their associated water). In Wang *et al*. (2012), the dry density is then reported as

$$\rho_{db} = \frac{B\rho_m G_{sa}}{G_{sa}(1+w_m) - \rho_m(1-B)(1+w_a)} \quad (11)$$

where B is the mass fraction of bentonite (-), ρ_m is the density of the mixture (kg/m^3), G_{sa} is the specific gravity of the additive grains (non-bentonite component) (-), w_a is the initial water content of the additive (-) and w_m is the water content of the mixture (-). However, this relationship is not dimensionally consistent and the equation was corrected in Wang *et al*. (2013). The correct version of the equation is:

$$\rho_{db} = \frac{B\rho_m G_{sa}\rho_w}{G_{sa}\rho_w(1+w_m) - \rho_m(1-B)} \quad (12)$$

where ρ_w is the water density (kg/m^3). This error does not affect the general result but it means the calibration that Wang *et al*. (2012) proposes has to be refitted using different values of α and β. If one does not wish to use a general correlation, for a given composition of bentonite one can perform the same correlation using dry density (rather than bentonite dry density) against swelling pressure (equation 9), but the result will not be general across different mixtures of bentonite with non-swelling minerals (e.g. Figure 2-16 – same data as Figure 2-15 but using dry density – from Wang *et al*., 2012).

It has also been noted that the effective density of water in bentonite is heavily dependent on the suction state, i.e. on entering the inter-layers of the diffuse double-layer, the water does not necessarily have a density consistent with a free water phase (see Figure 2-17 - Jacinto *et al*., 2012) and may be significantly higher. It is also the case that, to a good approximation, the unconstrained swelling volume is equal to the volume of water that has been added.

Furthermore, the data from Step 1 show that under unloading following previously constrained conditions there is a relatively fast response of the system in taking in water, coupled with a very small elastic rebound. This suggests that a stress dominated control on suction may be present (as used by Dueck, 2004), rather than saturation controlled as is typically assumed in the BBM. This is because with a very small elastic rebound there is only a small change in saturation and hence a small change in suction state to drive the inflow of water. The Step 1 experiment also suggests non-Darcy behaviour, where flow of water shuts down at low pressure gradients (see Bond *et al*., 2014). It is also considered that some data suggest that swelling is not purely volumetric, i.e. that the orientation of bentonite grains means that swelling in different directions is at least partially controlled by the normal stress to the inter-layer orientation.

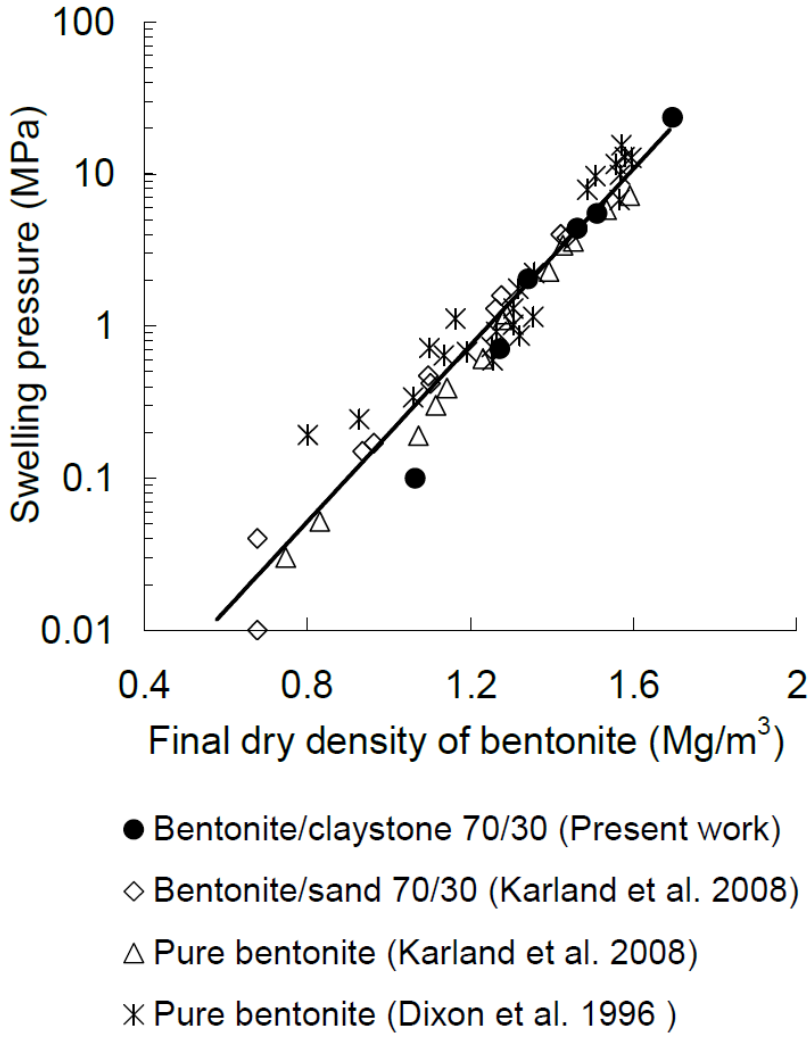

Figure 2-15. Swelling pressure versus bentonite dry density, for a range of bentonites (from Wang, 2012) with broadly similar initial water contents.

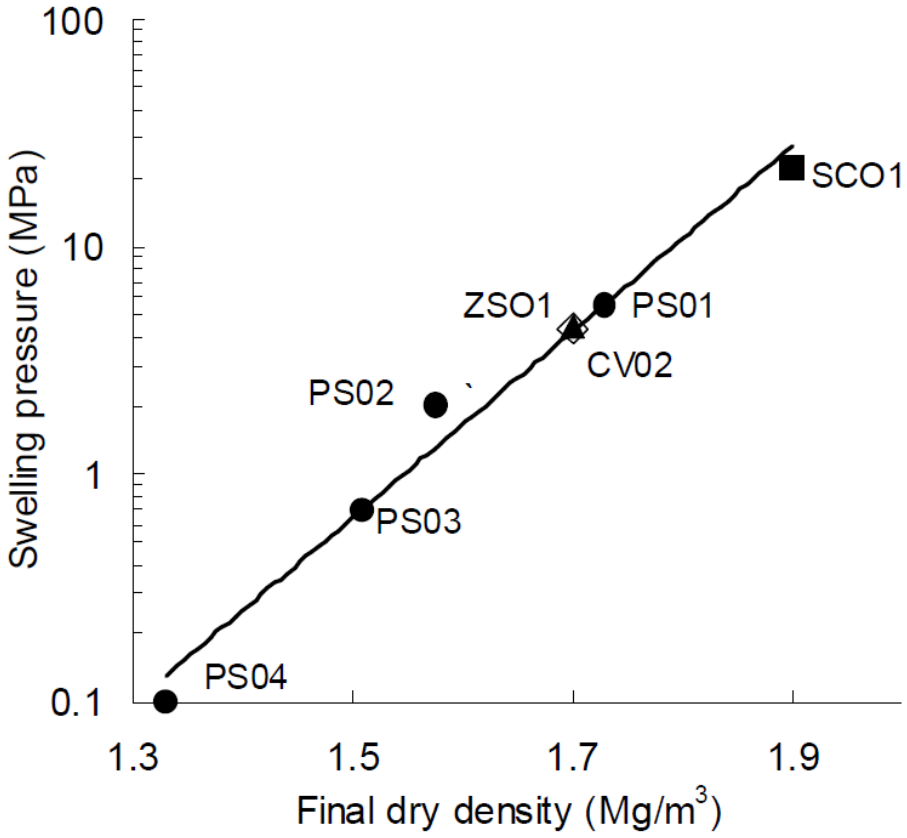

Figure 2-16. Swelling pressure versus dry density (rather than bentonite dry density), for the data in Wang (2012) – to compare with the black circles in Figure 2-15.

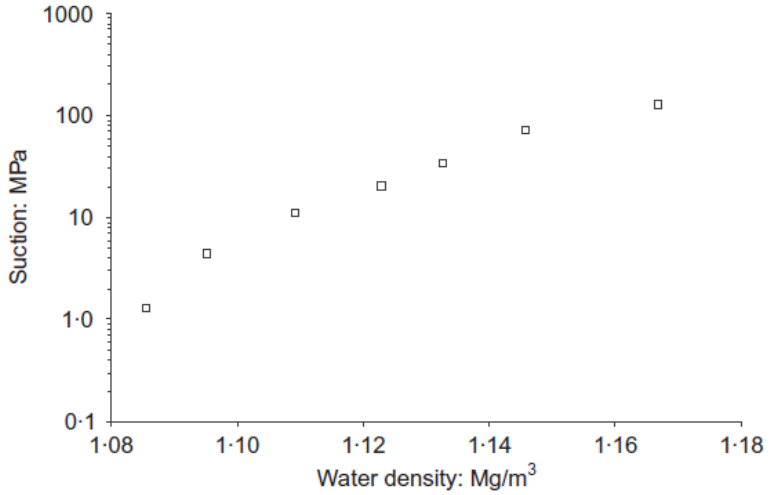

Figure 2-17 Suction versus effective water density from Jacinto *et al.* (2012).

2.3.3.3 Correlations

The correlation between swelling pressure and final dry density can be recast, for a given bentonite composition, to be a relationship between void ratio and stress (swelling pressure):

$$\theta = \frac{\rho_d}{\rho_g}$$

$$VR = \frac{\theta}{1-\theta} \quad (13)$$

where VR is the void ratio, θ is the porosity, ρ_d is the bulk dry density and ρ_g is the bulk (mixture) grain density.

The Dueck model for suction is assumed (Dueck, 2004), i.e.

$$s_{net} = s_f - \sigma \quad (14)$$

where s_f is the free swelling suction as a function of water content, and σ is the confining stress. By assuming that the model for swelling pressure versus final dry density (i.e. after any unconstrained swelling) is correct (equations 11 or 12), it follows that the bentonite cannot take up any more water when at this fully swollen condition, i.e. s_{net}≈0 MPa. Using equation 14, the free swelling pressure should be approximately equal to the confining pressure at this state. Further assuming that this state corresponds to the notional voids in the bentonite being completely filled with water, the saturated water content can be calculated as follows:

$$w_{m,sat} = \frac{\theta \rho_{w,0}}{\rho_d} \quad (15)$$

This allows us to calculate an expected free suction with water content profile (i.e. free swelling suction curve), purely based on the confining pressure with final dry density data. Taking the Wang (2012) model and re-deriving a fit to the 70/30 bentonite/non-swelling clay mixture data reported in Wang *et al*. (2012) one can compare the derived free suction curve (Figure 2-18) with the Step 0 data and also plot the implied void ratio (Figure 2-19).

The fit is shown in Figure 2-20 and is consistent with the fit that Wang adopted, i.e. the two lower dry density values sit below the correlation line rather than on it (black circles in Figure 2-16). The equivalent fit is shown schematically in Figure 2-21 to compare with the Wang (2012) fit.

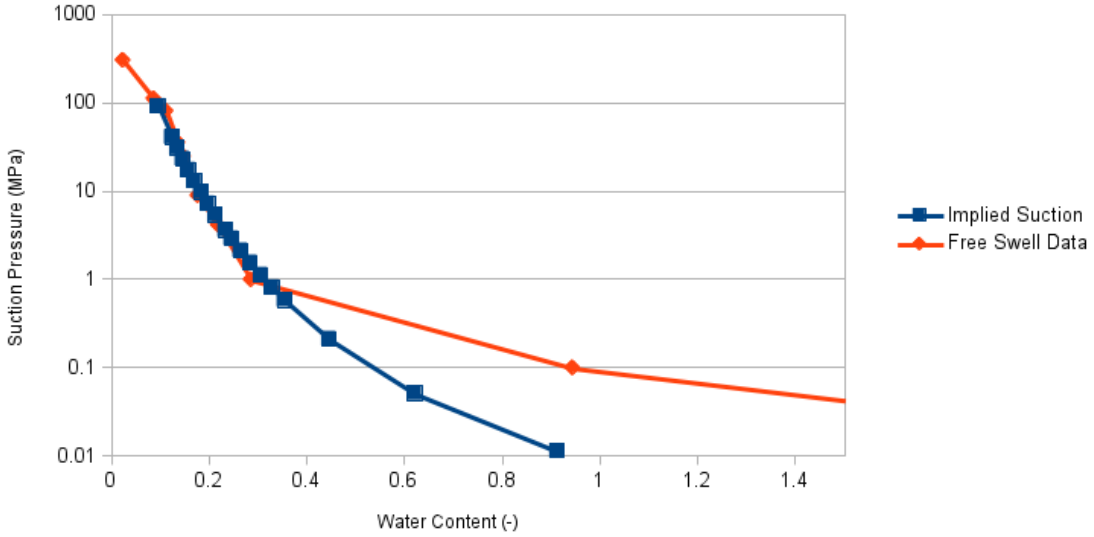

Figure 2-18. Comparison of the measured free suction data versus the equivalent data recovered from the swelling pressure versus dry density correlation.

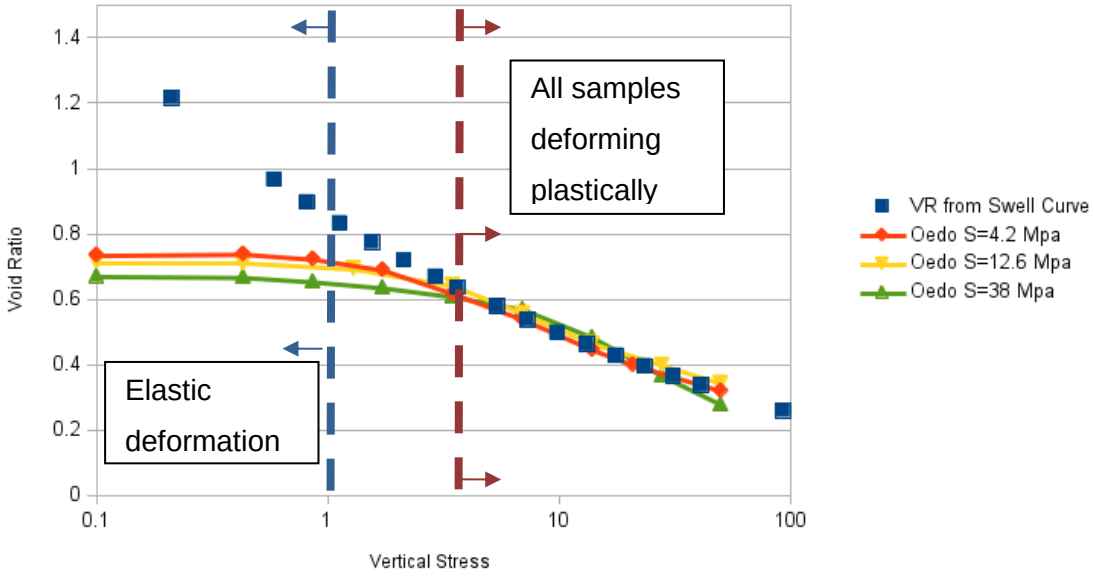

Figure 2-19. Comparison of the void ratio versus confining stress curve recovered from the swelling pressure versus dry density correlation, compared with the Step 0 higher suction oedometer results (compression cycle only).

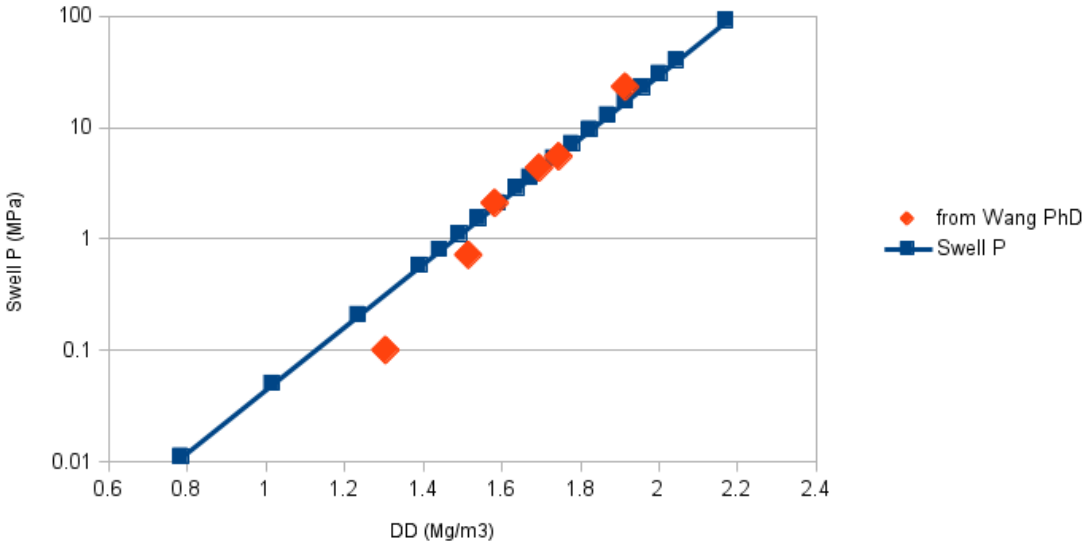

Figure 2-20. Dry density versus swelling stress correlation using 70/30 bentonite/non-swelling argillite data in Wang (2012).

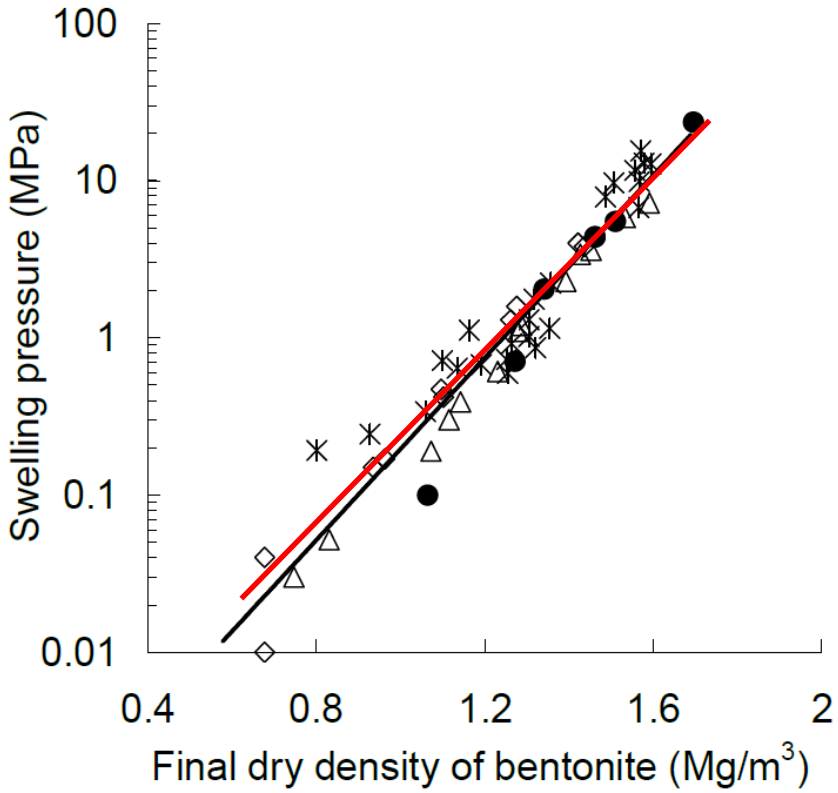

Figure 2-21. As Figure 2-16 but with the current correlation model added for comparison (red line).

The free swelling suction curve derived from the Wang *et al*. (2012) swelling pressure model is functionally identical to the independently measured free swelling suction curve (Figure 2-18) down to very low suctions – potential reasons for the deviation are discussed later. Similarly, when compared against the three more reliable oedometer data from Step 0 (only the compression path curves are shown for clarity), one can see that the implied void ratio-stress plot matches the assumed plastic deformation line on the oedometer plots (Figure 2-19).

If correct, this gives rise to some very interesting conclusions:

- The compaction curve is a fundamental limit in bentonite systems controlled almost entirely by the initial state of the bentonite and the final bentonite dry density.
- The path to reaching this limiting stress/density condition is not important - essentially the same result would be obtained for a swell followed by compaction as for fully constrained swelling.
- Any decrease in suction that occurs when the bentonite is on the compaction line does not result in a change in void ratio (either through swelling or collapse due to the failure surface being made smaller); rather, any expansion is either internal (reducing macro-porosity) or results in the presence of free water – this is a major difference to the BBM.
- The development of swelling stress is intimately controlled by the free suction.
- The majority of the suction model, the compaction line and the swelling pressure can all be defined using a simple two parameter model in addition to the basic information regarding the bentonite density and composition. This is a major difference to the BBM and related models, where the parameterisation of the compaction, swelling and suction models are almost completely independent of each other.

It is clear that clays and solids which do not exhibit such strong swelling do not behave in this way, and that the BBM was originally developed to model such low swelling systems. It appears that the strong swelling nature of bentonite overwhelms many of the subtleties in the BBM formulation and therefore a simpler representation may be possible. A possible implementation for such a model is discussed in the following sections.

2.3.3.4 Mechanical Model for the ILM

The suggestion is that the observations concerning the apparent relationship between swelling, suction and consolidation are combined to create a new model that would be more robust over a wider range of bentonite densities and less dependent on a large number of calibrated free parameters. Following the observation of the consolidation limit with stress, this new model is referred to as the Internal Limit Model (ILM).

In order to address the complexity of the orientations of the interlayer structure a high-level conceptual simplification is taken and it is assumed that bentonite interlayer normals are equally distributed in each of the three principal directions and that the sample is homogenous and isotropic.

Volumetric Expansion

Following the analysis of the Step 0 data, it is assumed that the volumetric expansion due to addition of water in an unconfined state is approximately equal to the volume of water added. As a starting assumption, it was assumed that a water density of 1 Mg/m^3 was

representative, although more sophisticated models may be considered in the future (e.g. Jacinto, 2012). This volumetric expansion is applied on a directional basis by calculating the water content in each of the principal directions; i.e. the water content associated with those interlayers aligned in the associated principal direction. This in turn allows us to calculate the free suction in each of the principal directions ($s_{f_{ii}}, s_{f_{jj}}, s_{f_{kk}}$). Net water content can be calculated trivially from the three components.

Swelling, Suction and Stress

In this model the view is taken that swelling, suction and stress are all intimately linked and, to a large degree, are manifestations of a common set of processes.

Within a volume a suction is considered in the three different principal directions (each directional suction being associated with 1/3 of the bentonite volume) such that:

$$\begin{aligned} s_{ii} &= s_{f_{ii}} - \left(\omega\sigma_{ii} + (1-\omega)\sigma_p\right) \\ s_{jj} &= s_{f_{jj}} - \left(\omega\sigma_{jj} + (1-\omega)\sigma_p\right) \\ s_{kk} &= s_{f_{kk}} - \left(\omega\sigma_{kk} + (1-\omega)\sigma_p\right) \\ s_{net} &= s_{ii} = s_{jj} = s_{kk} \end{aligned} \qquad (16)$$

where ω is a coefficient to determine the relative strength of the volumetric stress versus principal stress in controlling the suction; i.e. non-aligned stresses versus aligned stresses. The volumetric stress, σ_p, has the following definition:

$$\sigma_p = \frac{1}{3}\left(\sigma_{ii} + \sigma_{jj} + \sigma_{kk}\right). \qquad (17)$$

The important element in this proposed model reflects the conceptual understanding that bentonite swells dominantly due to the expansion of interlayers and those interlayers will be sensitive to stress dominantly in their normal direction. This is different to the standard BBM assumption that swelling is dominantly volumetric; here deviatoric swelling is permitted. Conceptually this is a much more appealing model, because it links the physical understanding of main swelling mechanism (uptake of water into the bentonite interlayers) directly to the stress state.

An important consequence of this model is that changing the stress on the sample under constant suction conditions will cause the equilibrium water content and hence the equilibrium swelling state to change. This means that aspects of the 'elastic' response seen in the oedometer experiments may simply reflect the addition and expulsion of water and have very little to do with true elastic compression of the macro porosity. Again, this is conceptually sensible and consistent with the Task A observations to date, and was an important aspect of the MCC implementation in QPAC.

In contrast, the BBM normally relates suction to saturation, not water content, and as such under constant suction conditions the compaction must come about due to a combination of elasticity and plasticity, not directly from the loss of water, unless the suction relationship is also made a function of porosity.

Mechanical Model

The mechanical model comprises two components.

Firstly, a non-linear elastic model with a bulk modulus of the following form:

$$K_{ii} = K_0 + \zeta\left(\gamma\sigma_{ii} + (1-\gamma)\sigma_p\right)$$
$$K_{jj} = K_0 + \zeta\left(\gamma\sigma_{jj} + (1-\gamma)\sigma_p\right) \quad (18)$$
$$K_{kk} = K_0 + \zeta\left(\gamma\sigma_{kk} + (1-\gamma)\sigma_p\right)$$

where K is the bulk modulus (MPa) (subscript 0 denoting the isotropic reference value and the other subscripts denoting the components in each principal direction) and ζ is the hardening parameter with stress (-). If γ=0 then the bentonite behaves isotropically. Because of a lack of data on radial stresses available under Task A, this will be the starting assumption, but it is not necessarily expected to be realistic.

Secondly, the plastic model will define an Internal Limit Curve (ILC) for each of the principal directions defined by the Wang (2012) dry density versus swelling pressure relationship (equation 9). The ILC in each direction is calculated from a directional effective dry density calculated using the strain from the rest state (ϵ) and the reference dry density e.g.

$$\rho_{d,ii} = \frac{\rho_{d,0}}{1-\epsilon_{ii}} \quad (19)$$

noting that the total dry density under strain ($\rho_{d,v}$) for small strains (as typically written for the BBM) can be written as

$$\rho_{d,v} = \frac{\rho_{d,0}}{(1-\epsilon_{ii})+(1-\epsilon_{jj})+(1-\epsilon_{kk})} \quad (20)$$

Plastic strain is accumulated using a visco-plastic flow in the respective principal direction when the ILC is reached or exceeded.

For larger strains, equation (20) is better written as

$$\rho_{d,v} = \frac{\rho_{d,0}}{(1-\epsilon_{ii})(1-\epsilon_{jj})(1-\epsilon_{kk})} \quad (21)$$

This is a very simple model, essentially a density-dependent version of the Tresca model (Jaeger *et al*., 2007). Deviatoric plastic strain can be accumulated through a simple plastic Poisson's Ratio, such that a proportion of plastic strain being accumulated through compaction in one principal direction can manifest as expansion in the other principal directions. For the purposes of examining the available experiments, there are no data to constrain such a parameter so the plastic Poisson's Ratio is set to zero, i.e. the effect is neglected.

Implementation

The model described in the previous section has been implemented in QPAC and compared against the Step 0 oedometer data. The additional parameterisation beyond the basic bentonite information is given in Table 2-1.

Table 2-1. Parameterisation used for the ILM for Step 0.

Parameter	Value	Comment
K_0	50 MPa	Reference Bulk Modulus
ζ	30	Bulk Modulus Increment
υ	0.27	Poisson's Ratio
γ	0	Plastic localisation factor
ω	0.95	Swelling localisation factor
α	7.0×10^{-5} MPa	Using total dry density in equation (9) not bentonite dry density
β	6.5 m^3/Mg	Using total dry density in equation (9) not bentonite dry density

The results for the three non-zero suction cases are given in Figure 2-22.

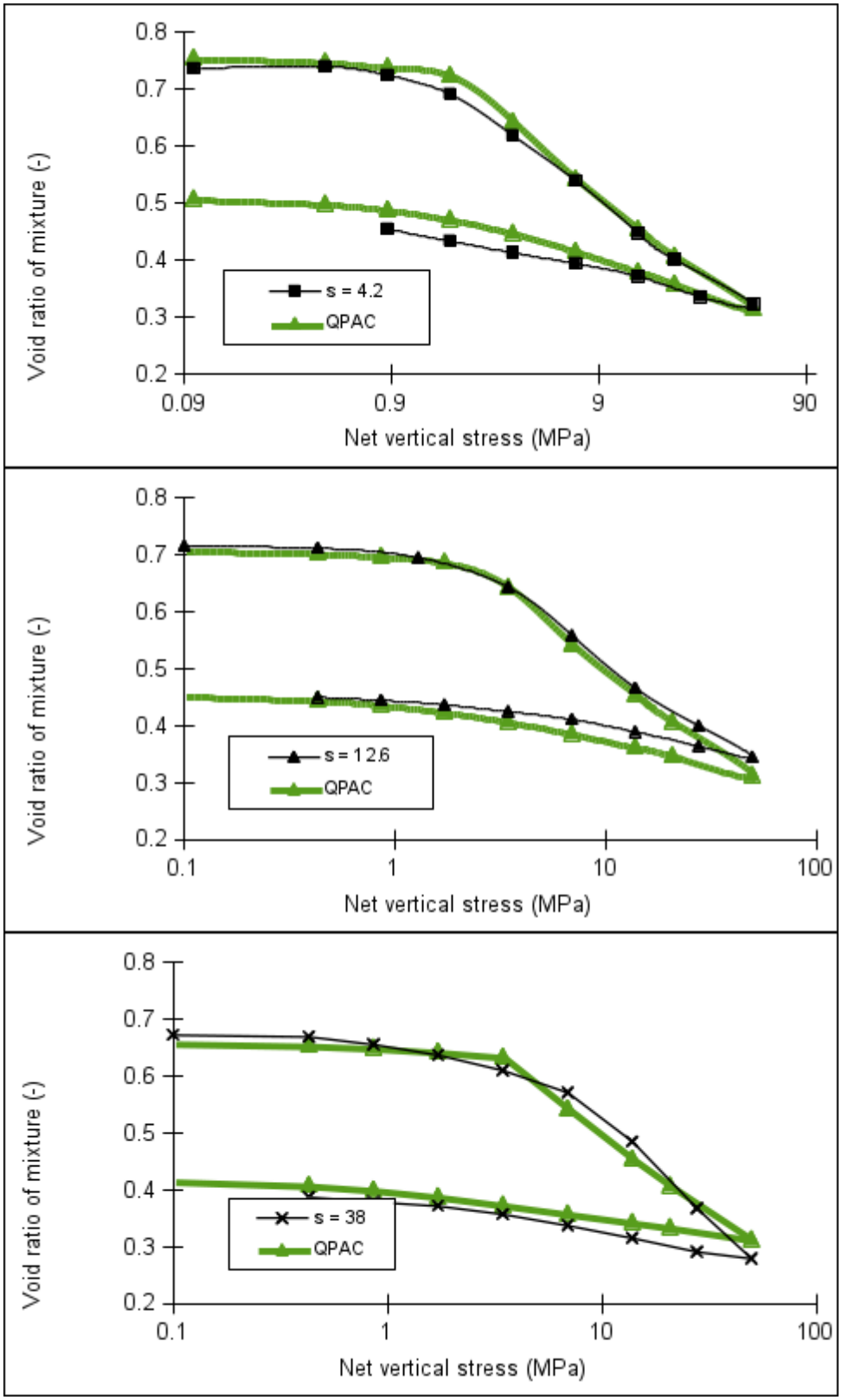

Figure 2-22. Comparison of the ILM model in QPAC (green) and data for the Step 0 oedometer tests. 4.2 MPa suction (top), 12.6 MPa (middle) and 38 MPa (bottom) shown.

Given the simplicity of the model, and the fact that the **same parameterisation** is used for all three models, the comparisons against the data are excellent. A better calibration could be obtained by further parameterisation, but given expectations relating to heterogeneity of the bentonites and experimental error, there seems to be little benefit in further calibration while retaining a simple model.

The same model was also applied to the zero suction oedometer case, again using **exactly the same parameterisation** (Figure 2-23). Some concern has been noted as to whether the sample had truly homogenised after each application of stress; this comparison should therefore be treated with caution. For this model the radial expansion was assumed to have already occurred, so there was no explicit treatment of the radial expansion, although as discussed previously, this makes no difference given how the ILM model is parameterised in this case.

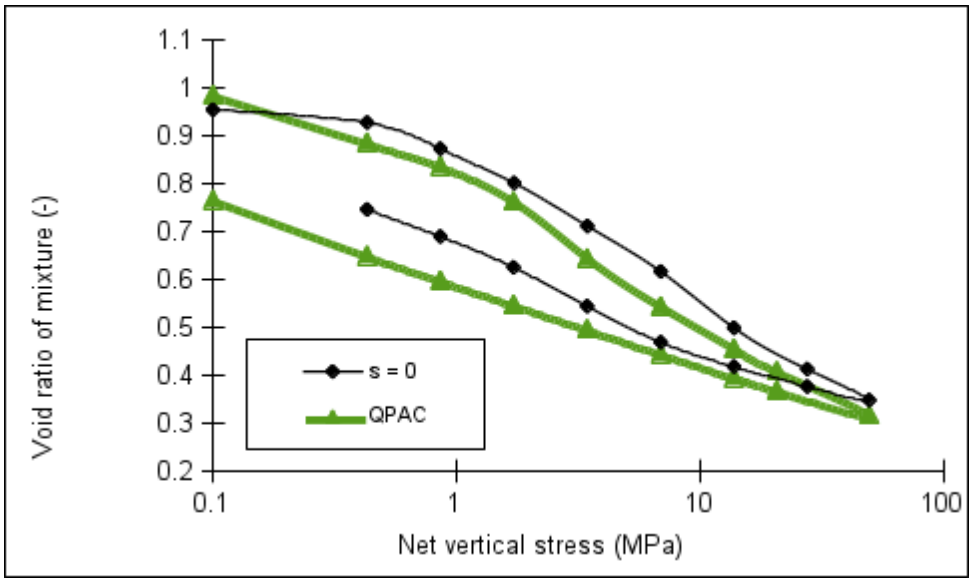

Figure 2-23. Comparison of the ILM model in QPAC (green) and data for the Step 0 oedometer tests. 0 MPa shown using the same parameterisation as for the other cases.

Given that a bentonite with a different initial density was used, the model results are remarkably close to the experimental results. The most interesting aspect of the response is the high degree of 'elasticity' shown by the model when the stress is removed, which is very similar to the experimental data. This is caused by the water coming out of the interlayers as stress is removed, rather than elasticity in the macro-pores.

Only a small change to the Wang (2012) correlation model is required to give an excellent fit to these data (moving the ILC curve slightly to the right), but this change makes the fit to the suction curve slightly worse (suction is increased for a given water content). However, this increase is consistent with some experimental data, itself implying that some calibration to starting dry density may be required. The Wang (2012) correlation is a very simple model but it appears to give an excellent starting point.

An alternative explanation for the difference between the model and the experimental results relates to the possibility that the zero suction sample might not have reached full equilibrium

with each stress step, tending to give a measured void ratio that is too high when compacting the sample. The high water saturation of the bentonite may limit vapour migration in the bentonite and therefore potentially make it more difficult to homogenise. As such, it is possible that the experimental results do not show the full equilibrium condition under compaction, however this is slightly speculative.

2.3.3.5 Coupling to hydraulics and Step 1 Results

The ILM mechanical swelling model was coupled to a variation of the standard QPAC Richards' Equation (RE) module (gas phase is assumed passive, i.e. constant gas pressure), used in testing the MCC and BBM calculations, in order to create a fully coupled hydro-mechanical model for bentonite. The key changes made to the RE module were to remove the limitation on water saturation being less than or equal to one and to express the mobility of liquid water and vapour through a single non-linear 'diffusion' term, i.e. using a simple vapour diffusion-like model to represent the mobility of water in bentonite. Such an approach has been used in the literature to successfully model bentonite hydration (Krohn, 2003), so adopting this form of approach is not without precedent:

$$Q = D(S_w)\nabla\rho_v \quad (22)$$

where Q is the water mass flux (kg m^{-2} s^{-1}), D is a diffusion coefficient (m^2 s^{-1}) that can be a function of water saturation (S_w) and is akin to permeability in this case, and ρ_v is the vapour density, which itself is a function of suction and hence fluid pressure. Overall the form is very similar to the previous Darcy flow implementation (see Bond *et al*., 2014).

These simple changes made to the RE module were intended to represent the possibility of net water density not being equal to the expected free water density, hence permitting the bentonite to hold more water than expected at full water saturation (Figure 2-17).

A further sophistication of the model is possible in that the swelling and transfer of water can be kinetically limited. There are few data to parameterise such a process, so for the initial work an instantaneous swelling and release model is adopted.

The hydraulic model was calibrated using the Step 0 infiltration test (see Bond *et al*., 2014) and the mechanical model used from calibration against the Step 0 oedometer tests (Table 2-1). The same boundary conditions and grid as adopted for the Step 1 calculations were employed again and results compared against the experimental data. These predictions were clearly better than the predictions made using the MCC model, and a subsequent step of minor calibration (Table 2-2) produced the fits to the experimental data shown in Figure 2-24 to Figure 2-26.

A key modification from the MCC model was the scaling of diffusivity (effectively permeability when compared with the MCC and BBM models) directly as a function of dry density, rather than a minor scaling using porosity. This approach follows the general conclusions of Stewart *et al*. (2003) and the customised changes made to the BBM by IRSN in Step 1, where intrinsic permeability is seen to vary by orders of magnitude with differing dry densities of bentonite. This is a pure calibration effect, but it appears to circumvent the problems of the lack of uptake of water in Phase 2 (removal of vertical confinement after the Phase 1 confined rehydration) and 3 (halting further vertical expansion of the bentonite at 20% vertical strain) seen using the qBBM and MCC models. With hindsight, the requirement of additional terms to compensate for the very large dry density changes should not be a surprise, especially given that the Step 0 infiltration test, on which the hydraulics were

calibrated, only shows small changes in local bentonite dry density and overall is a constant volume. Addition of such a scaling to the qBBM and MCC models would doubtless improve the fit to the problematic Phase 3, and may be considered for future variants in support of Step 3, given that it is a trivial change to make to the models.

Cross-checking back to the oedometer tests showed that the fit to the zero suction oedometer test remained good and not appreciably worse than that shown in Figure 2-23.

Table 2-2. Parameterisation used for the ILM for Step 1.

Parameter	Value	Comment
K_0	200 MPa	Reference Bulk Modulus – increase from Step 0 required to match Phase 2 recovery.
ζ	30	Bulk Modulus Increment
υ	0.27	Poisson's Ratio
γ	0	Plastic localisation factor
ω	0.95	Swelling localisation factor
α	1.5x10^{-6} MPa	Using total dry density in equation (9) not bentonite dry density
β	8.5 m^3/Mg	Using total dry density in equation (9) not bentonite dry density
D	$0.25 \times 10^{DD}(S_w)^6$ [m^{2}s^{-1}]	S_w is the notional water saturation calculated using a water density of 1 Mg m^{-3}
DD	1.47 [Mg/m^3] -> -2.5 [-] 1.57 [Mg/m^3] -> -2.8 [-] 1.67 [Mg/m$_3$] -> -4.3 [-] 1.97 [Mg/m^3] -> -5 [-]	Cubic spline interpolated lookup of dry density versus power scaling factor.

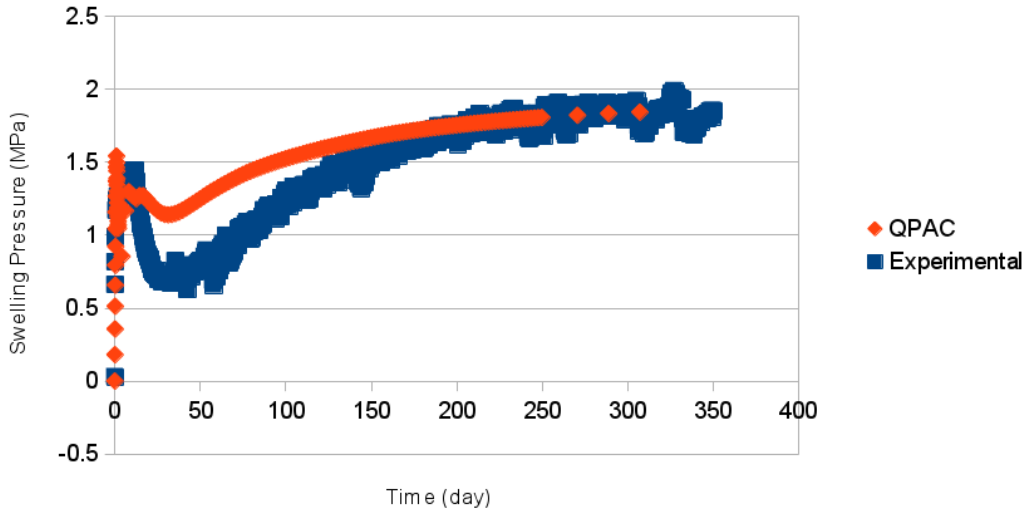

Figure 2-24. Comparison of axial swelling pressure versus the QPAC ILM model for Step 1 during Phase 1.

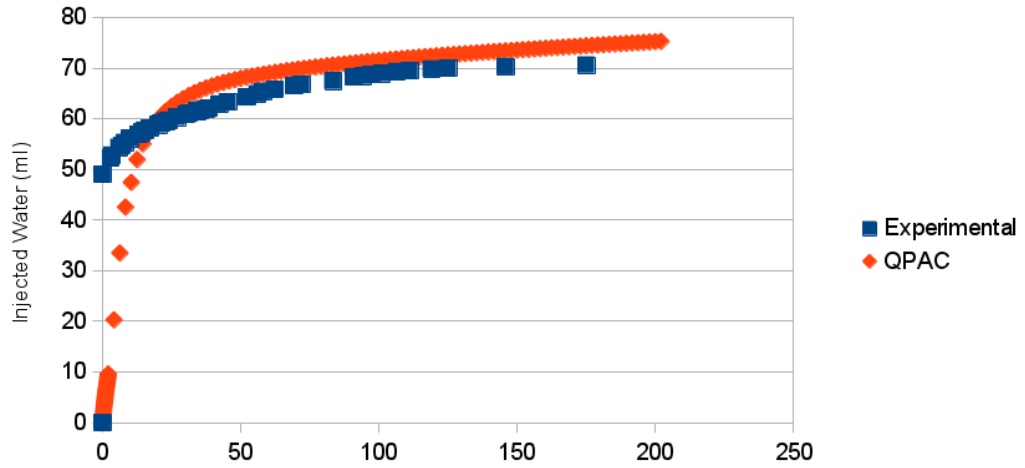

Figure 2-25. Comparison of water uptake versus the QPAC ILM model for Step 1 during Phase 1.

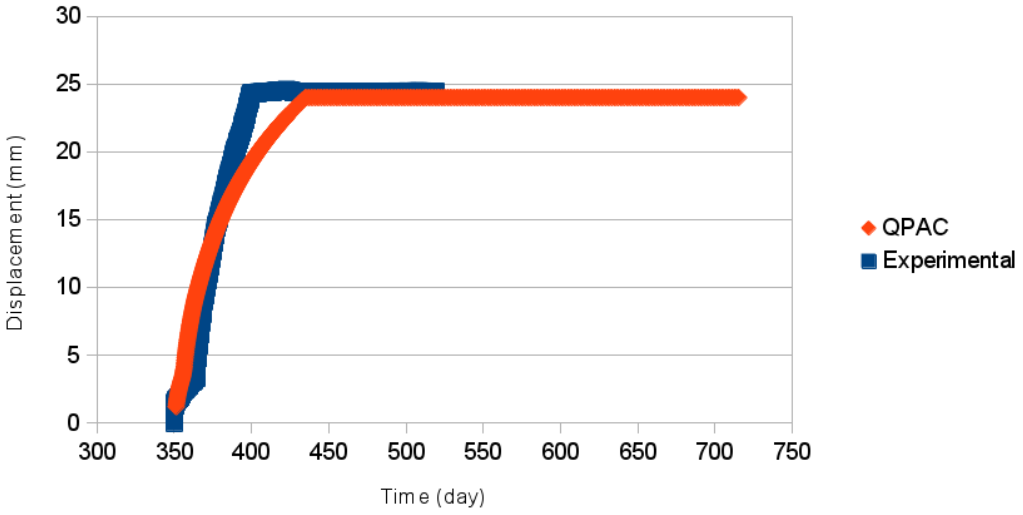

Figure 2-26. Comparison of axial displacement the QPAC ILM model for Step 1 during Phases 2 and 3.

2.3.4 Way Forward for QPAC Bentonite Models

Clearly the results produced by the ILM are good; at least as good as using the other models. However, this model should be regarded as provisional because there is considerable uncertainty, permitting notional saturations to exceed 1 (although there are some limited and indirect data to support this) – this aspect of the ILM needs further consideration. In general the lack of radial stress and strain data, together with no information on the water content under loading and unloading to assess whether the concept of water saturation needs to be strictly applied in bentonite, means that it is not possible to distinguish between these three candidate models (MCC, qBBM and the ILM).

For this reason it is proposed to retain the three models for Step 3, where it is expected that three-dimensional stress data as well as different water content data will be available, giving the opportunity to distinguish between the models.

2.4 Continued Development of the Non-Linear Elastic Model in OpenGeoSys (OGS)

As presented in Bond *et al*. (2014), the non-linear elastic model (the primary area of work for the UoE PhD student) was in the very early stages of development, with results for the consolidation test presented from an Excel model. An understanding of the processes occurring within the bentonite was being formed to help guide the development of the model. The next stages in the work flow were to implement the non-linear elastic model in OpenGeoSys, develop a deforming mesh to record the strain history and also increase the applicability of the model to large strain applications, and to then couple the hydraulics to the mechanics. The proposed approach uses some of the elements described in Section 2.3.3 and should be regarded as another attempt to unify processes that are regarded as separate in models such as the BBM.

2.4.1 Hydraulic-only Model

The hydraulic processes occurring during compacted bentonite resaturation have been modelled in OGS using Richards Flow approximation (see Section 2.4.3.1 in Bond *et al*., 2014). Previously the infiltration test was modelled in OGS using a artificial relative permeability model. This model was a function of three parameters represented by saturation, time and added water in order to help understand the likely process couplings acting on the hydraulics and hence inform the QPAC Step 0 implementation (Bond *et al*., 2014). The results indicated the need for a reduction in permeability with time as the internal swelling of bentonite filled the macro-porosity within the sample at the later stages of saturation. Moving forward with this model to simulate partial free swell conditions and the different phases of Step 1 would require a recalibration of this relative permeability function, because the assumption of confining conditions is not always valid. Consequently, the Dueck suction model (see Section 2.3) has been implemented in OGS in 1D and 2D simulations.

'Dueck' suction uses the concept that confining conditions have a significant influence over the observed/net suction i.e. the net suction is a function of both the free swell suction or a given water content and the confining pressure acting on the sample. Suction pressure is the primary variable in the Richards Flow approximation, and as such a given water content is used to calculate the suction pressure for each iteration. The main steps of the implemented Dueck suction model are;

- Look up the water content for the given suction pressure/capillary pressure. This is the 'free-swell' suction curve determined in laboratory experiments (Millard and Barnichon, 2013).
- Determine the maximum water content for a given dry density and porosity (the dry density for confined conditions is currently kept constant, but will be allowed to change with further development of the code).
- Determine the maximum swelling pressure using Wang's theory (Wang, 2012).
- Use the current water content and maximum water content to calculate the confining pressure.
- Add the confining pressure to the suction pressure, because the confining pressure is working in the same direction as the internal suction.
- This corrected suction is then used to look up the corrected water content.

The implementation of Dueck suction also allows the Richards calculation to proceed with water content input as opposed to degree of saturation. Water content is converted to a saturation in the relative permeability function. The relative permeability is calculated as a simple power function of

$$k_{rel} = (S_w)^5 \qquad (23)$$

with an intrinsic permeability of 2.5×10^{-21} m^2. The results and comparison with the synthetic relative permeability model (Bond *et al*., 2014) are shown in Figure 2-27. The sensor farthest from the base of the sample is well-predicted, the middle sensors are slightly under-predicted (but generally follow the correct trend and are close to the data at the end of the experiment), and the closest sensor under predicts the initial water uptake but gets close towards the end of the experiment. In comparison to the hydraulic-only (H-only) model which

used the synthetic relative permeability curves (Figure 2-27) the furthest sensor shows a slight improvement but the closer sensors are not improved upon. The results are comparable with the values shown by the QPAC H-only model (Bond *et al*., 2014), both in terms of parameterisation and results, which builds confidence in the mutual applicability of both codes and models.

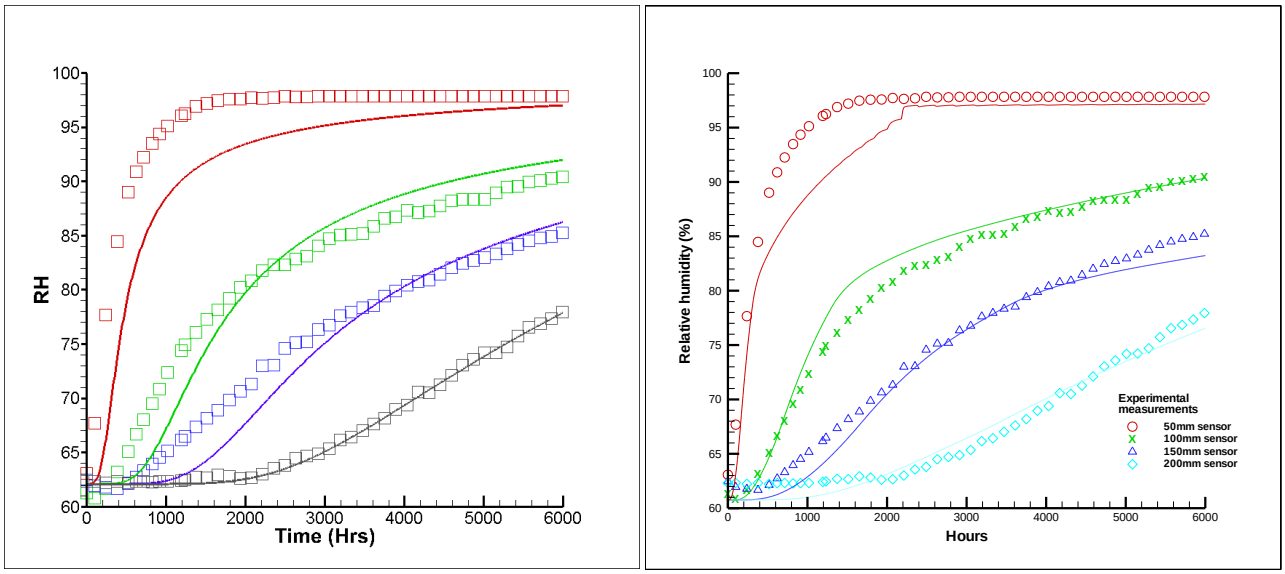

Figure 2-27. Comparison between the RH profile calculated using Dueck suction (left) and previous curve calibration for H only models (right - from Bond *et al.*, 2014).

2.4.2 Including Mechanics

The non-linear elastic approach relates the elastic properties of the material to the strain history of the sample. This is a simple empirical fit to oedometer tests on the MX-80 bentonite samples at different suctions and is described by the following formula. At any point in time (*t*) the Young's Modulus can be calculated as:

$$E_t = E_0 \left(1 - \left(\alpha \sum_{i=t_0}^{t} \varepsilon_i\right)^d\right) \quad (24)$$

where E_0 is the initial Young's Modulus of the material (Pa), α is the strain hardening parameter, ε_i is the total volumetric strain, and d is the dimensionality parameter. A significant advantage of this method is that the mechanical behaviour of the samples in the consolidation tests can be modelled using three parameters, without requiring the calculation and parameterisation of the plasticity matrix.

As a method to record the strain history of the sample, a deforming finite element mesh has been implemented in OpenGeoSys. This has been developed as a simple r-refinement adaptive meshing technique, but is currently controlled purely by the displacement of the nodes at the end of each time-step rather than by solution accuracy, which is the common motivation for adaptive meshing. Further development of the deforming mesh will need to address mesh quality issues associated with large strains. In simple elasticity models, displacement is calculated at each node in each element and summed to give the overall

solution. The non-linear elastic method uses the calculated displacements at each node to update the node coordinates within the mesh at the end of each time-step. This provides a simple method of adapting the mesh within an explicit solution (Figure 2-28).

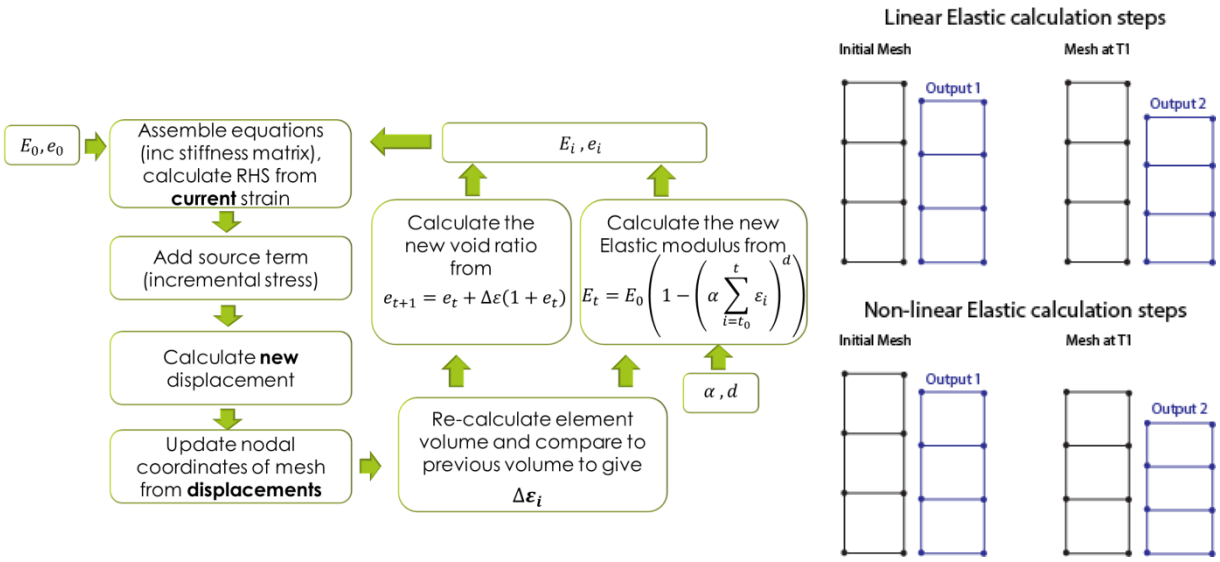

Figure 2-28. A flow chart of the explicit solution used to calculate the non-linearity of the material properties (left) and the mesh calculation steps for the non-linear elastic and linear elastic models (right).

For the mechanical model it is possible to achieve a calibration to the consolidation tests by considering a common starting material for the lower density samples, i.e. 1.67 Mg/m^3 samples at suctions of 4.2 MPa, 12.6 MPa, and 38 MPa. This common starting material was calibrated to have an initial elastic modulus of 54.44 MPa before suction imposition occurred (Figure 2-29). The starting E_0 for the consolidation tests is given by the elastic modulus after swelling using the HM model. A different parameterisation is required to model the zero suction case of higher density bentonite (Figure 2-30).

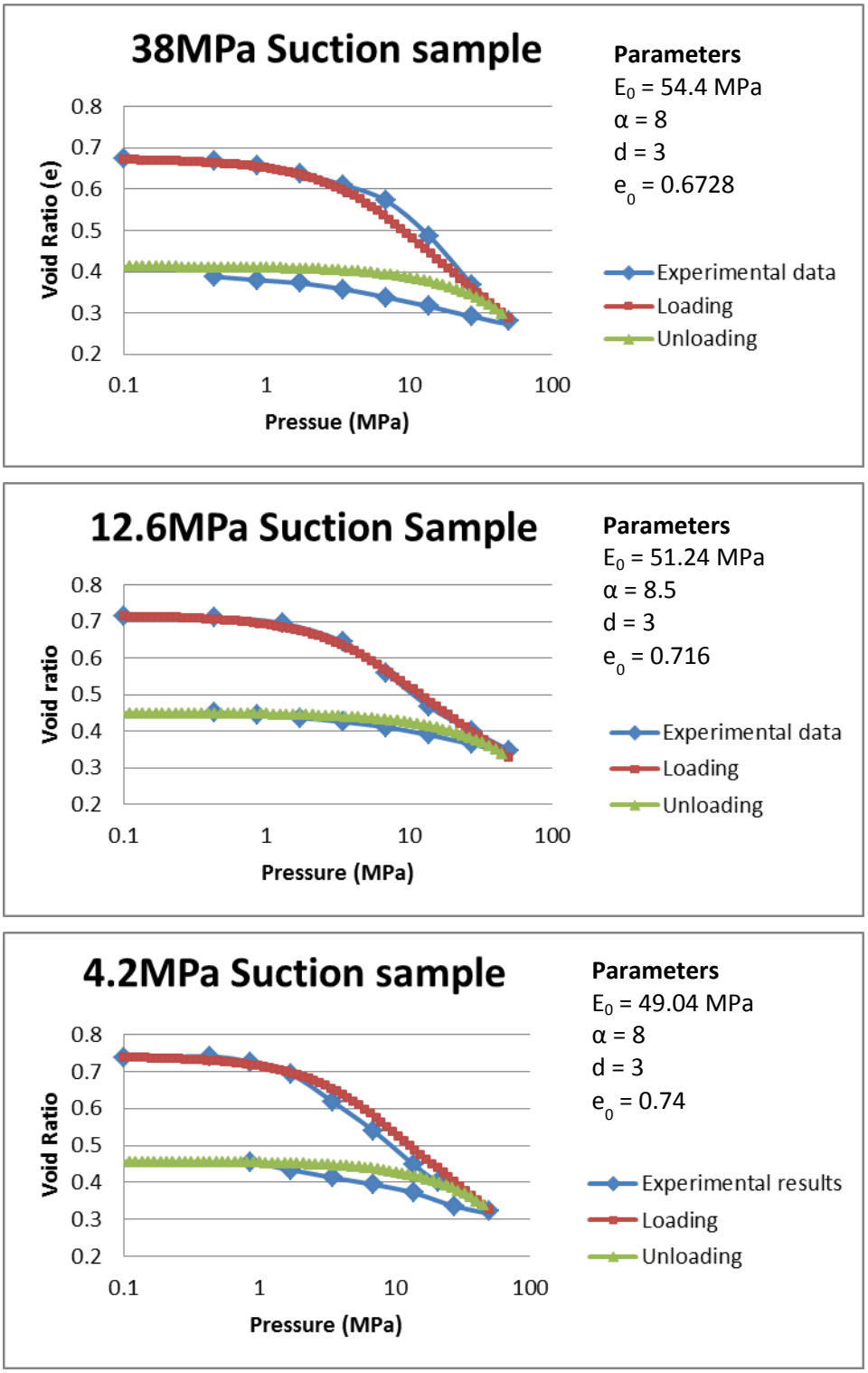

Figure 2-29. Consolidation tests on the lower density samples using E_0 values calculated from a HM coupled model simulation of pre-consolidation suction imposition from a common starting material.

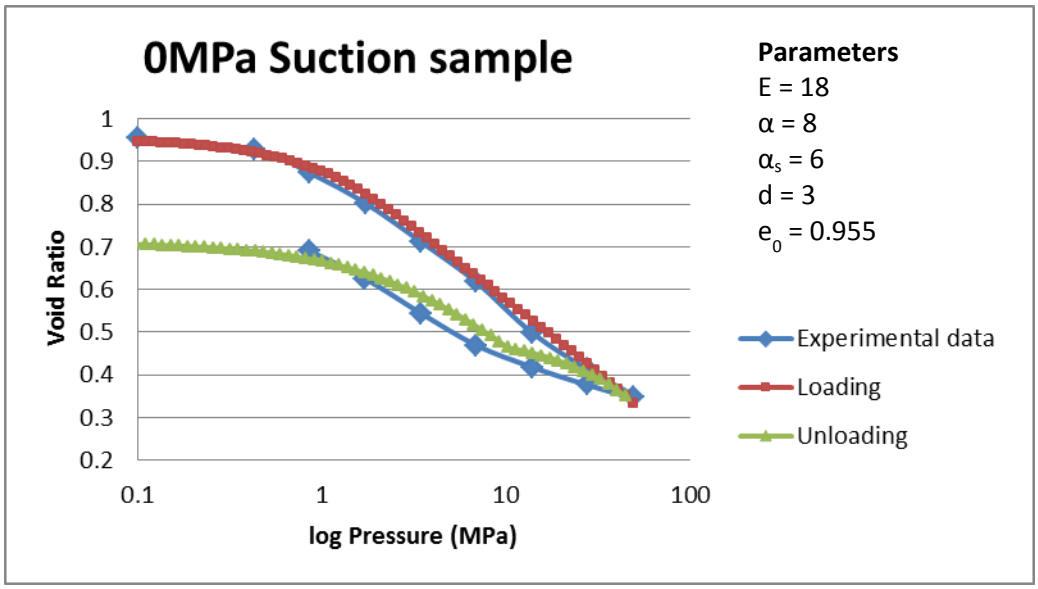

Figure 2-30. Comparison of the mechanical results to the high density, 0 MPa suction consolidation test results.

2.4.3 Initial Hydro-Mechanical coupled model

A fundamental control on the HM behaviour of bentonite has been identified as the hydration of the interlayer cations (Bond *et al*., 2014). The degree to which the cations are partially hydrated controls the suction pressure, driving fluid flow within the system. At low water contents the suction pressure is high, as the cations are dehydrated, but as water content increases the suction pressure reduces. It has been shown that the stress conditions experienced by the sample have a significant impact on the water uptake behaviour of bentonite (Millard and Barnichon, 2013). If stress conditions allow free swelling, then the uptake of water can proceed until the percentage water content by mass is in excess of 250% (as reflected by the liquid limit of sodium bentonites). However, if the stress conditions exert a constant volume control over the sample, then far less water can enter the sample. Water content can be directly related to the suction pressure for free swelling conditions and therefore a change in suction will result in a change in volumetric behaviour.

The proposed coupling is to use a suction pressure-water content look-up curve that is used in the hydraulic parameterisation and derived from experiment - the free-swell curve. The coupling is implemented in a staggered HM scheme such that, after the hydraulics have been calculated using the Richards Flow approximation, the mechanical process is coupled to the hydraulics by looking up the change in water content from the previous time-step. The previous water content corresponds to a suction pressure on the look-up curve which is subtracted from the corresponding suction pressure for the new water content. This differential pressure is then used as a source term for the deformation process.

As the suction change can be very large, and it is known that not all suction change (Δs) results in volumetric expansion (Likos and Lu, 2006), a factor that takes into account the amount of suction pressure change that is accommodated by macro-pore destruction is applied. The deformation source term is therefore calculated as:

$$\sigma = \Delta s\, \beta \quad (25)$$

where β is the internal strain factor.

Porosity is a function of the strain of the sample. At the end of each deformation calculation, the elemental void ratio is calculated for the next time-step. This void ratio is converted to a porosity that is assigned to each element. This allows the porosity to vary within the sample as saturation and deformation proceed. As the lowest part of the sample takes in water, it swells and increases porosity (θ) from the initial porosity (θ_0). In order to achieve a full HM coupling, the intrinsic permeability k (m^2) must also change as a result of this. The coupling method proposed by Quintessa is implemented in OGS (from Bond *et al*., 2014):

$$k = k_0 \left(1 + 10 \frac{(\theta - \theta_0)}{\theta_0}\right) \quad (26)$$

where k_0 and the relative permeability function (equation 23) are recalibrated to give a better fit to the data, i.e.

$$k_0 = 1.5e^{-21} \text{ m}^2$$

$$k_{rel} = Sr^{3.8} \quad (27)$$

The results show the HM coupled model is slightly better at fitting the initial saturation and also the general trends of the data. However, it is still unable to capture the very fast resaturation seen in the closest sensor. This failure to match the data at the lower end of the sample is consistent with the observations from the QPAC model and the other Task A teams' results. This suggests that a significant feature or process is missing from all the numerical calculations of the Step 0 infiltration test relative to the experiment. Given that the upper parts of the experiment fits relatively well, this deviation has not been pursued further, but it is noted as a key uncertainty in the analysis.

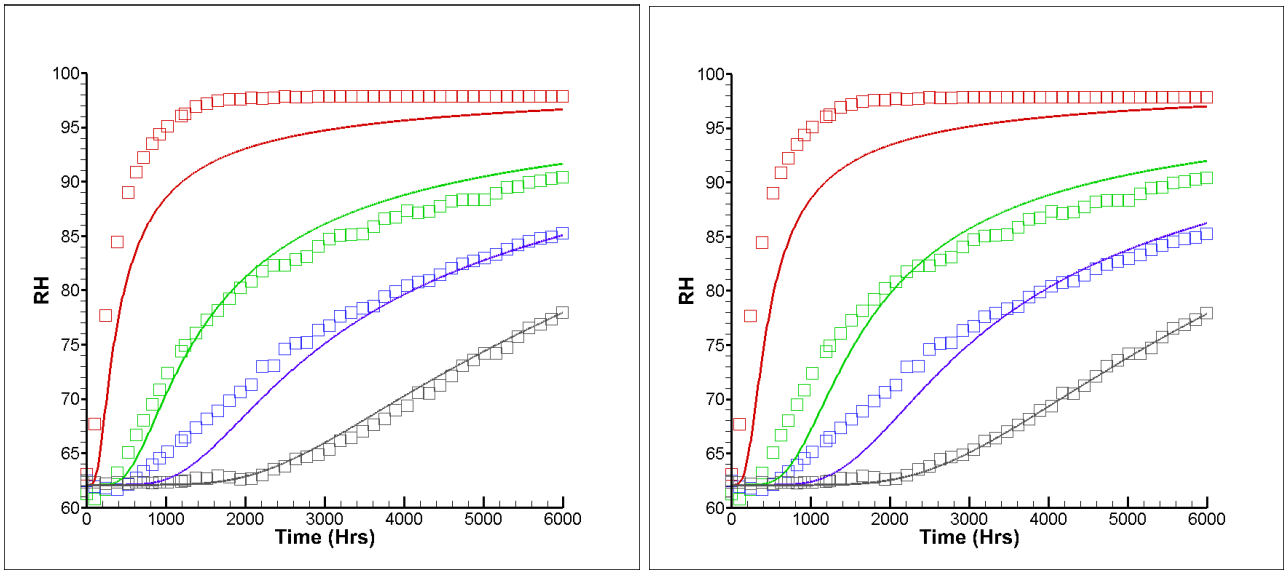

Figure 2-31. Comparison between the HM coupled model (left) and H-only model for the infiltration test (right)

2.4.4 Key Outcomes and Future Work in OGS Component of Task A

Now the basic implementation is complete, work is expected to proceed quickly over the next six months by the UoE PhD student focussing on:

- Coupled HM consolidation tests
- Addressing mesh quality problems at the mesh edges for free swell conditions
- Implementation of complex Step 1 boundary conditions
- Full Step 1 Model

It is expected that this work will inform and complement the candidate ILM model and it is expected that elements from both approaches will be tested in the other modelling framework.

2.5 Step 2

2.5.1 Specification

Step 2 considers a water injection test (WT-1) that is on-going at the Tournemire URL. The aim of this test is to understand how much water might be lost to the host rock in the full SEALEX experiments (to be considered in Step 3), without the complication of the presence of a bentonite seal. Modelling the experiment provides some constraints on the hydraulic properties of the argillite for later steps, but also provides some experience on any particular issues surrounding modelling in this particular geometry, again in preparation for later steps.

In the full SEALEX experiments, a bentonite seal is placed in a 60 cm diameter borehole (Figure 2-32). The bentonite is emplaced inside a confinement system to ensure the length of the seal does not change through the experiment. At either end of the seal, a constant water pressure is applied and a sealing system is in place to ensure water tightness.

The WT-1 test has a simple design that only considers the downstream lid of the full SEALEX experiment, with its water tightness system comprising inflated O-rings and injected epoxy resin (Figure 2-33).

The borehole for the WT-1 experiment is located off the main experimental gallery at the Tournemire URL, to the north of the access gallery (Figure 2-34). The relative humidity and temperature in the experimental gallery have been recorded since December 2008 (Figure 2-35) and show annual cycles with high humidity in the summer and lower in the winter.

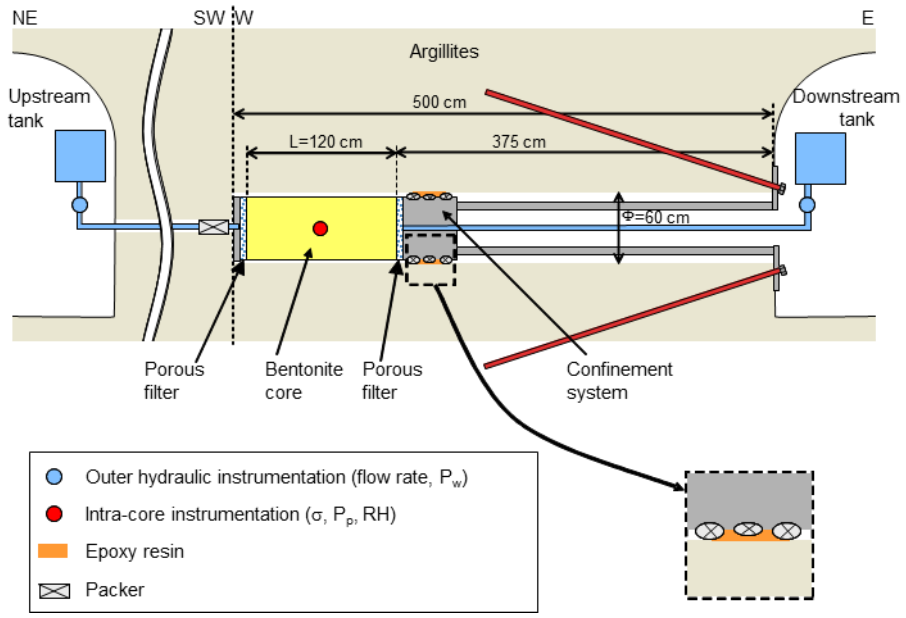

Figure 2-32: Experimental set up of one of the SEALEX experiments, showing the bentonite plug and the surrounding confining and sealing systems (from Millard and Barnichon, 2014).

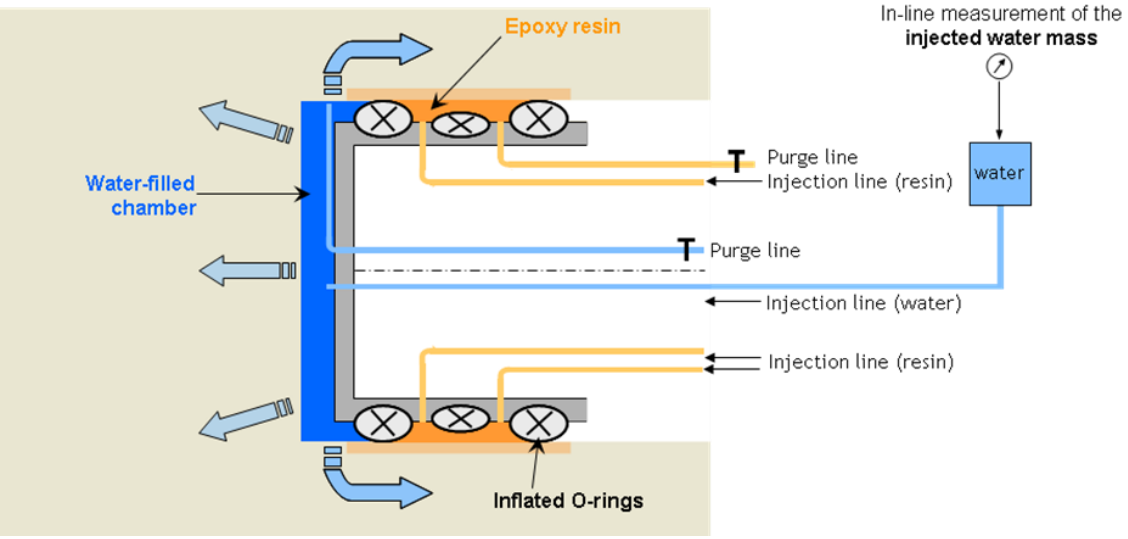

Figure 2-33: Experimental set-up of the WT-1 test (from Millard and Barnichon, 2014).

.

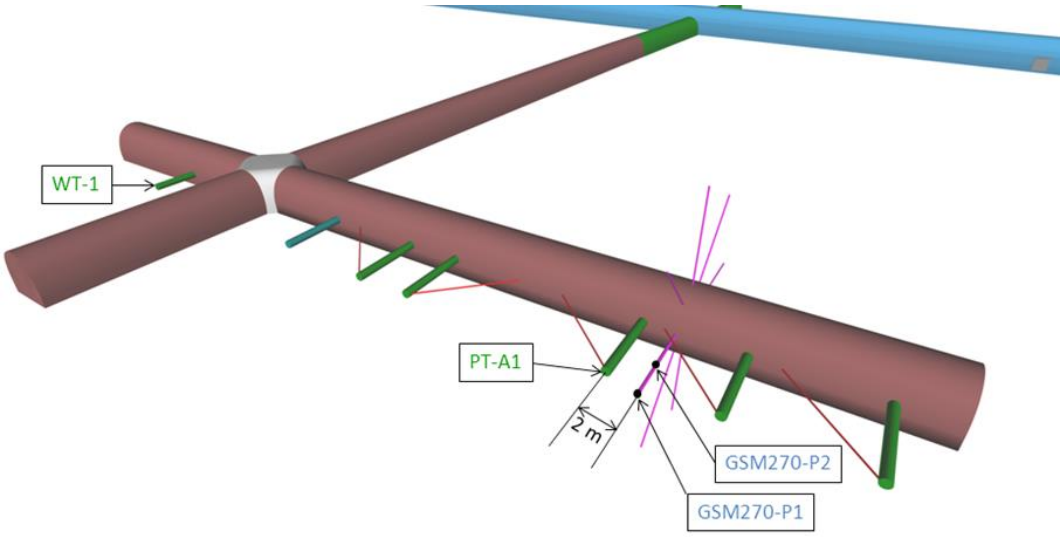

Figure 2-34: Layout of the Tournemire URL with boreholes WT-1 and PT-A1 highlighted (from Millard and Barnichon, 2014).

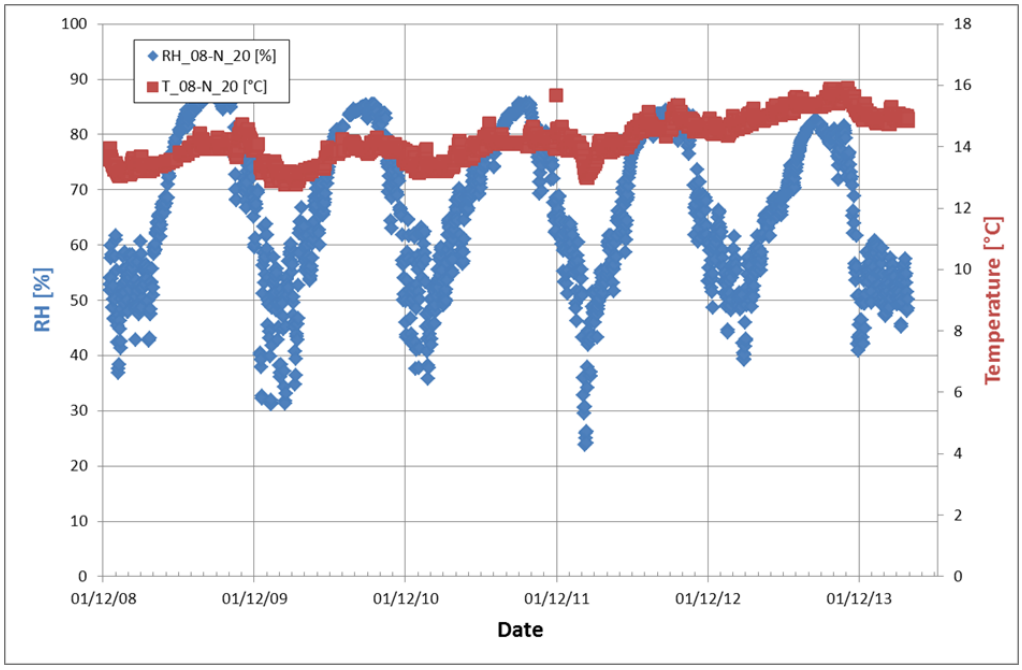

Figure 2-35: Temperature (T) and relative humidity (RH) time series in the experimental gallery (data from Millard and Barnichon, 2014).

There are no pressure readings in the argillite close to the WT-1 borehole, but pressure measurements are available close to the PT-A1 borehole (Figure 2-34). Measurements are available both vertically above and below the experimental gallery and in the horizontal plane at radial distances of 3 m and 6 m (Figure 2-36). Data recording started in 2010 and captures the construction of the PT-A1 borehole. As an optional task, it was suggested that teams might build a model of the hydro-mechanical evolution of the experimental gallery to try to reproduce the observed pore pressures. This task is discussed further in Section 2.5.4.

The WT-1 borehole was drilled in 2011 over four days (1st March until 4th March) at a rate of around 1 m per day and it is 3.75 m long with a diameter of 60 cm. After excavation, the borehole head was closed with a plastic sheet to limit desaturation of the borehole walls. The experimental equipment was installed into the borehole from 29th until 31st March and comprises a 35 cm long steel plug with a 5 cm gap between the steel and the end of the borehole. Resin was injected around the steel to ensure that water cannot escape between the steel and the rock (Figure 2-37).

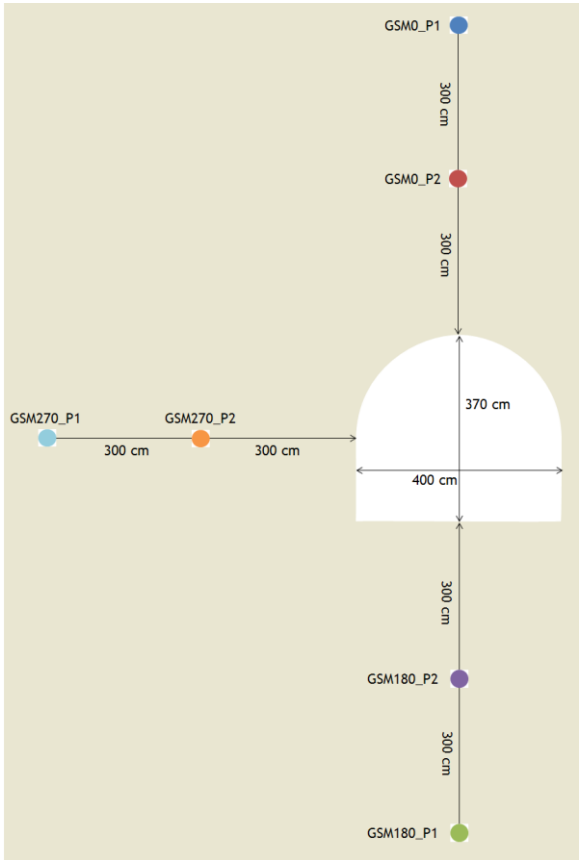

Figure 2-36: Location of pressure measurements close to borehole PT-A1. The locations of points GSM270_P1 and GSM270_P2 are also shown in Figure 2-34.

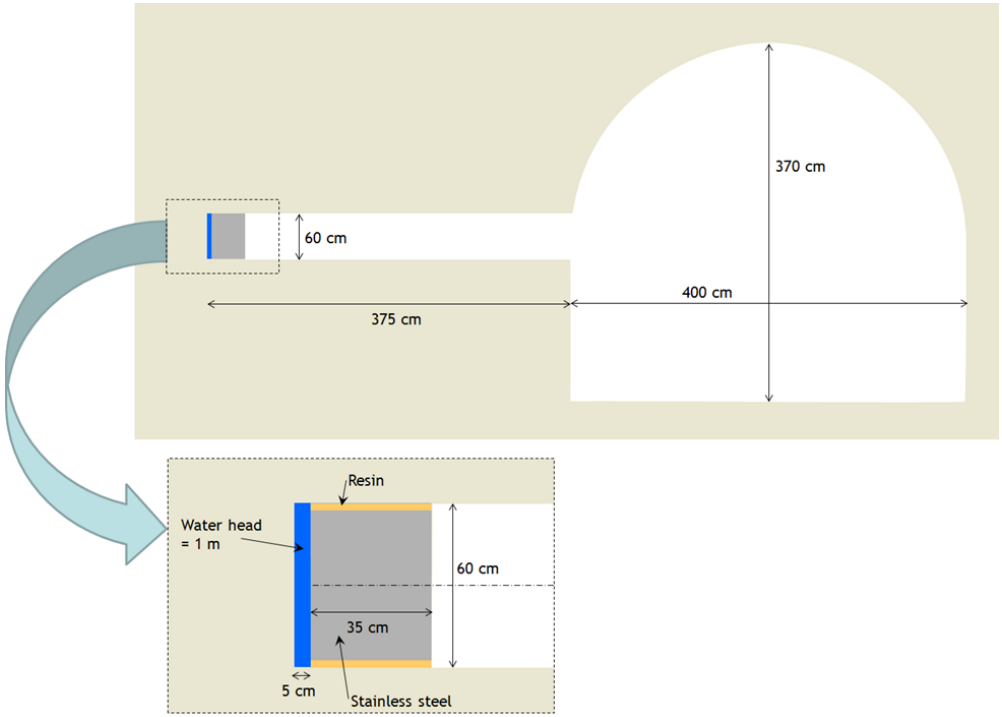

Figure 2-37: Geometry of the WT-1 experiment.

The experiment started on 7th April 2011 with two phases of synthetic groundwater injection from a water tank in the gallery:

- Phase 1 involved a water head of 20 m for two hours and was designed to fill the void between the rock and the steel containment device with water.
- Phase 2 involved application of a 1 m head and is on-going at the present day. The head is maintained at 1 m above the axis of the borehole.

The injected water mass is constantly recorded and no leak has been detected. The full raw data for the injected water mass (Figure 2-38) shows 16.6 kg of water injected during Phase 1, which is similar to the mass of water that would fit in the initial void space. The rate of injection drops significantly in Phase 2, when the driving head is only 1 m and the voids in the experimental setup have been filled.

After the first three months of Phase 2, there is a hiatus in the water injection mass data and when the data continue, the rate of injection is much higher (Figure 2-39). The initial lower gradient has been attributed to a problem in the way data were collected (Millard and Barnichon, 2014), and so a correction has been added to the data so that a single gradient can be used to fit the data over the first year (Figure 2-39). The correction involved adding 200 g to the data after the first three months. Reference curves, which include the correction, have been provided for the total water mass and the water mass minus the initial flooding (Figure 2-40) and it is these curves that the teams were asked to fit.

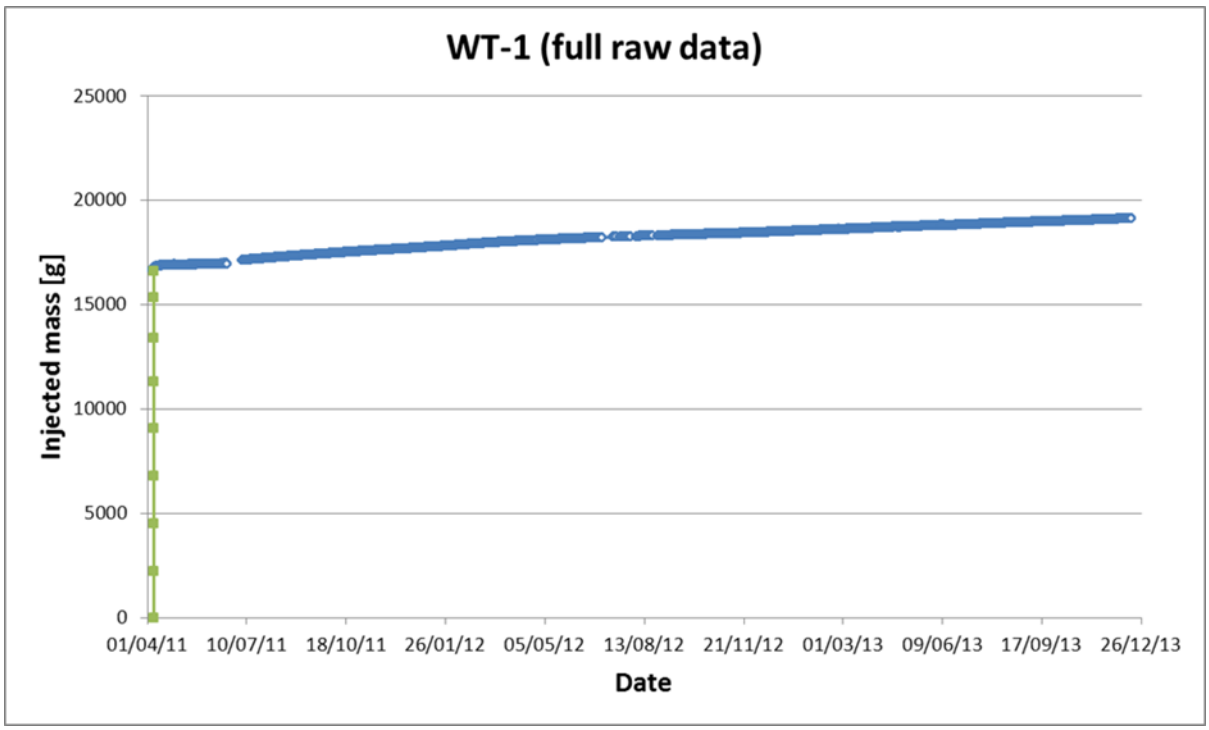

Figure 2-38: Raw data for the mass of injected water during Phase 1 (green) and Phase 2 (blue) (data from Millard and Barnichon, 2014).

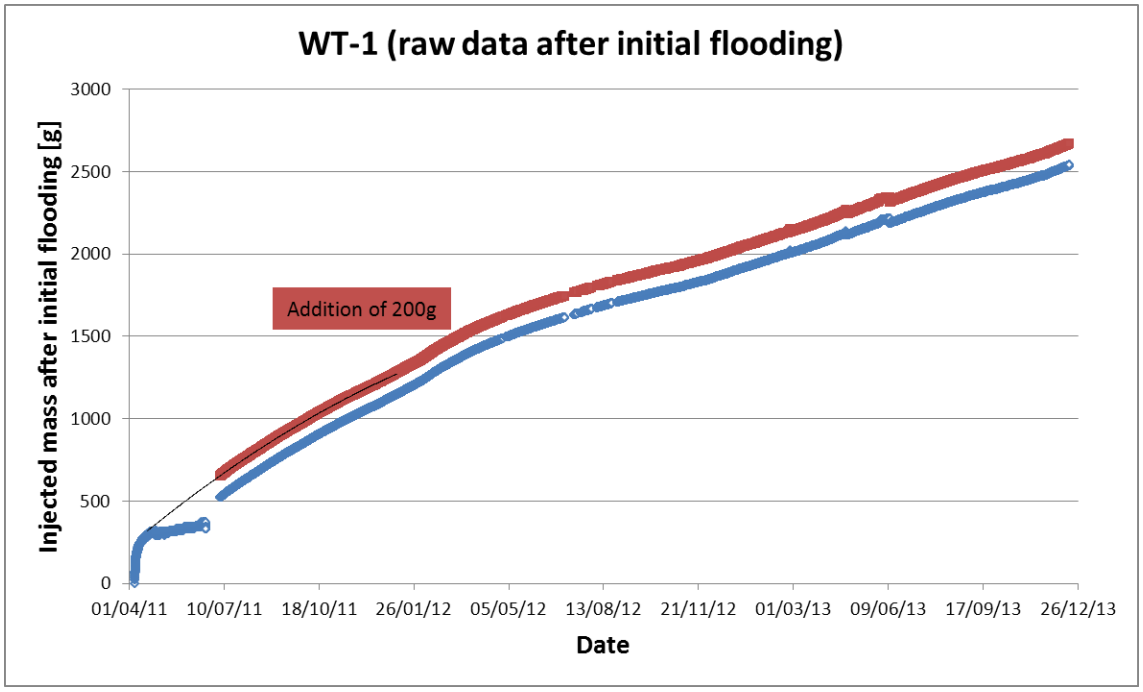

Figure 2-39: Phase 2 injected water mass (blue) and with a correction (red) (data from Millard and Barnichon, 2014).

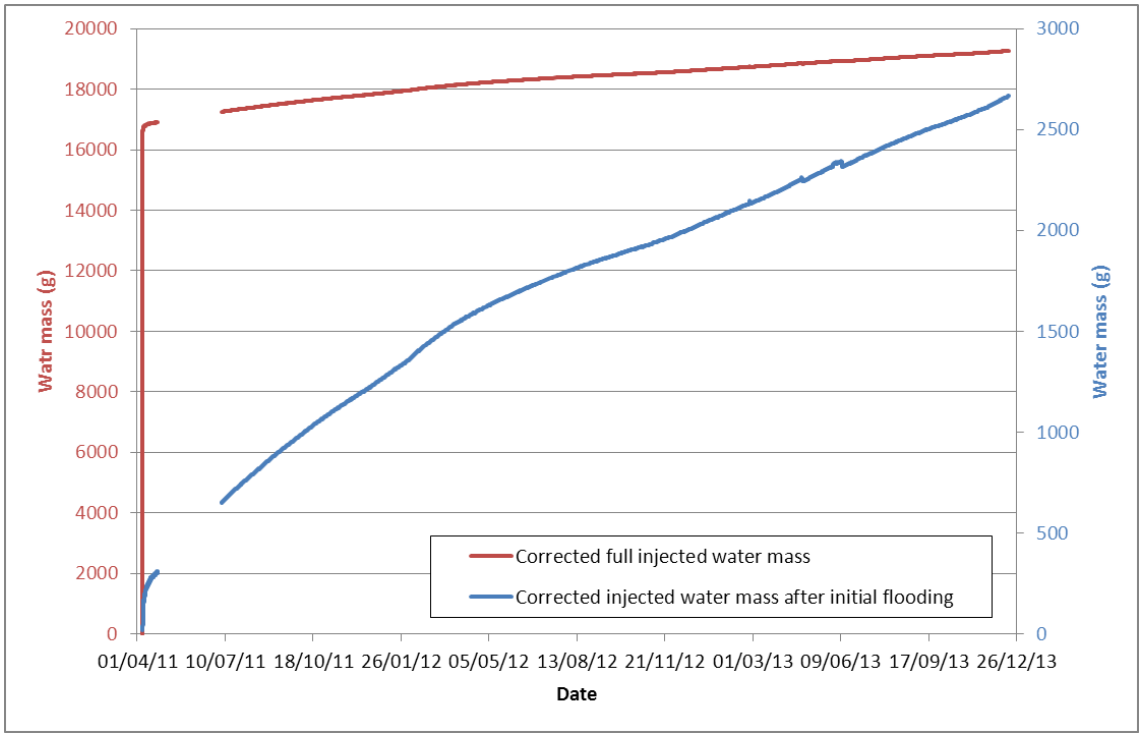

Figure 2-40: Reference curves for the full injected water mass and the injected water mass after flooding (data from Millard and Barnichon, 2014).

Each modelling team was asked to build a model to replicate the water injection test. Alongside a description of the main characteristics of the model used, the time evolution of the injected water mass with and without the initial flooding was requested. It was suggested that teams start with a simple 2D hydraulic model and add complexity as required.

An optional task was to build a 3D model of the hydro-mechanical response of the pore pressure in the host rock to excavation of the gallery and the PT-A1 borehole to try and reproduce the measured data.

2.5.2 Approach

The suggested approach to modelling the water injection test was to construct a simple 2D hydraulic model and make it more complex if necessary. It was suggested by the Task A management that the pore pressure data supplied could be used to inform the initial conditions of the model and a hydro-mechanical model could be set up to model the pore pressures.

In the main, the suggested approach was followed. Firstly, the water injection data were studied to try and gain insight into the processes that might be important to capture in the model. A simple 2D hydraulic model was then constructed using QPAC and found to give adequate results. It was decided that the initial pore pressure distribution was not important for understanding the water injection test, but that it would be useful to spend some time understanding the pore pressure data to help in later steps within Task A. The pore pressure data were examined and a 2D hydro-mechanical model constructed, again using QPAC.

In the following text, the water injection modelling and then the pore pressure modelling are described as two separate stages, and the findings discussed at the end.

2.5.3 Water injection test

2.5.3.1 Data analysis

Phase 1

During Phase 1, the void space was expected to be filled with water. The initial void space in the experiment can mainly be attributed to the 5 cm gap between the end of the borehole and the experimental equipment. The volume of this void is 0.0141 m^3 which would be filled by a mass of 14.1 kg of water (assuming water density of 1000 kg/m^3). The specification details another 1 kg of water expected to fill void space although it is not clear where this additional void space is.

During Phase 1, a total of 16.6 kg was injected into the system, but only 15.1 kg are accounted for by the initial void space. The extra 1.5 kg could be injected into the rock, or could be accounted for by a 10% error in the void space calculations. An error of this magnitude could arise due to the borehole end not being flat or there being cracks in the argillite surface that fill with water.

Phase 2

The total amount of water injected during the first 20 months of Phase 2 (i.e. by 16th December 2012) was 2.67 kg. The rate of injection is several orders of magnitude slower than Phase 1 because the applied head is much lower and the water is flowing into the argillite rather than filling a void space. It seems unlikely that 1.5 kg of water could have

been injected into the rock in 2 hours during Phase 1 as this would imply the flow rate into the rock was over 1000 times faster during Phase 1, despite the applied head being only 20 times higher.

If the initial 3 months of Phase 2 are temporarily ignored because of the data collection problem, the remaining data follow a roughly linear trend, with a change in gradient after 1 year (Figure 2-41). The linear nature of the data suggests that the inflow of water can be represented by saturated Darcy flow between two fixed heads although the reason for the change in slope after one year is not clear. The change in gradient occurs quite rapidly, and doesn't appear to be due to a slowly-evolving process from the start of the experiment. The decrease in influx rate suggests a reduction in permeability, head gradient or flow area rather than any leakage. Possible explanations include a change in the Engineering Damage Zone (EDZ) permeability as any fractures heal or the possibility of activity in the tunnel (e.g. drilling) causing a change in the pressure in the rock (although no such activity has been reported).

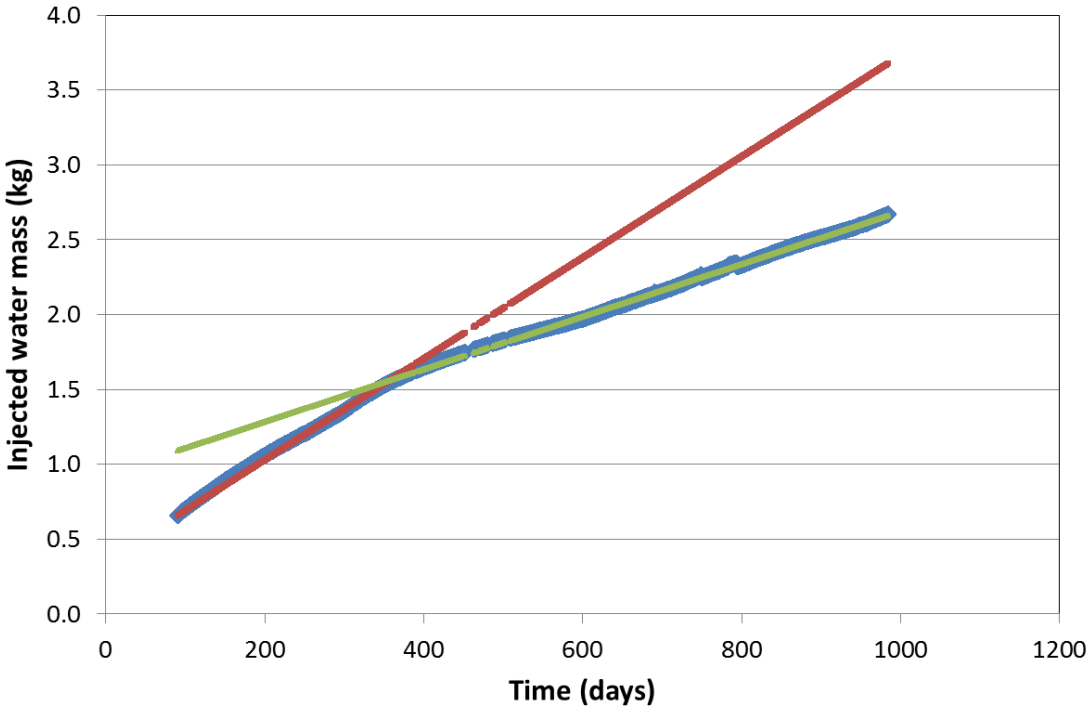

Figure 2-41: Injected water mass with linear trend lines. Raw data blue, trend lines in red and green.

Subtracting the linear trends from the data reveals an oscillation with a period of 1 year, reflecting the oscillating relative humidity in the experimental gallery (Figure 2-42). This demonstrates that the pressure gradient causing flow into the argillite is driven by the difference in pressure between the applied head and the relative humidity causing a suction on the gallery walls. A reduction in relative humidity in the tunnel increases the effective suction on the tunnel wall. Depending on the suction state in the rock adjacent to the tunnel wall, this will either reduce the flow of water vapour into the rock, or cause the vapour to flow into the tunnel, drying the rock.

It is noticeable that, whilst the gradient of the linear trend changes between the first and second year of data, the magnitude of the oscillations about the trend remains similar. This could provide additional information about the cause of the change in rate of injection and will be considered in future work.

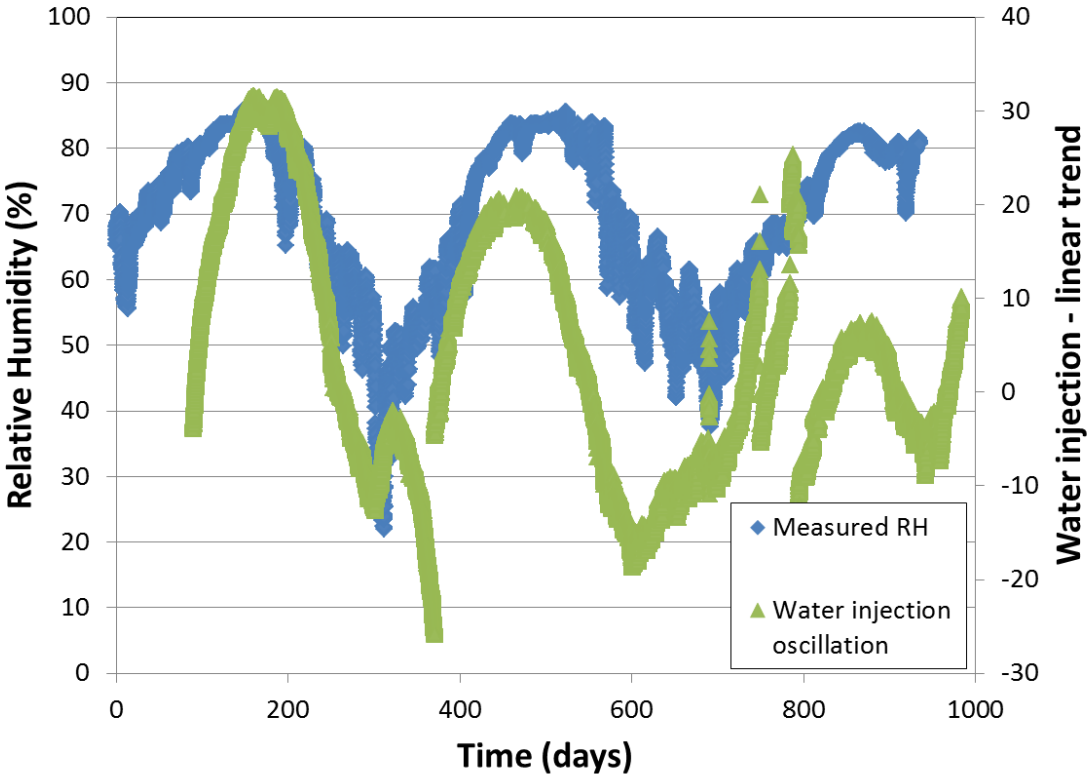

Figure 2-42: Relative humidity in the tunnel compared to the difference between the injected water mass and the linear trend lines.

2.5.3.2 QPAC model

The QPAC model has been set up to reflect the conceptual model of the experiment based on the data. It was assumed that the water flows are governed by Darcy flow in a mostly saturated medium, although some small-scale desaturation in the walls of the gallery and borehole is to be expected. It is not clear to what extent the injected water flows to the walls of the borehole or the main gallery, so both were included in the model. The change in permeability after 1 year was imposed on the model as a change in EDZ permeability after 1 year, although this is an assumption for which there is currently little supporting evidence. This assumption was discussed with other teams participating in Task A as well as with the experimentalists, and despite some teams implementing more complex coupled hydro-mechanical models, no one had a good physical explanation for the change in injection rate.

The QPAC model has a 2D cylindrical (axisymmetric) grid (Figure 2-43) which incorporates the borehole and gallery as boundary conditions and represents the host rock, EDZ and void space into which water is injected.

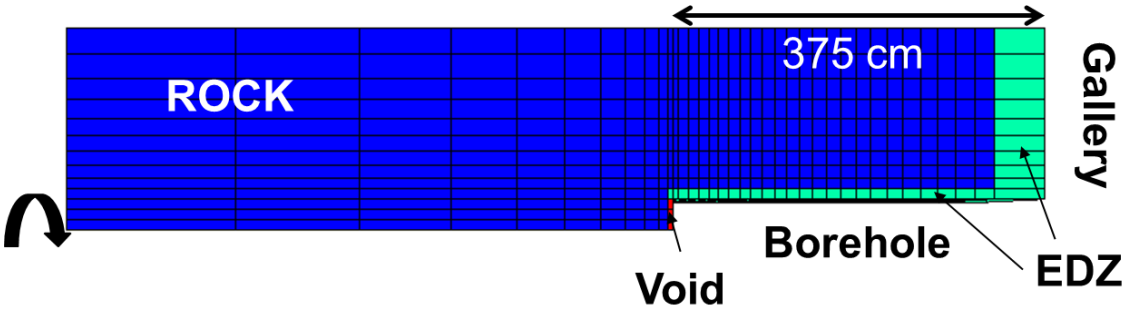

Figure 2-43: QPAC axisymmetric grid for the water injection test.

The hydraulic properties of the argillite and EDZ are assumed to be the same, apart from the assumption that the EDZ has a higher permeability for the first year of the model run and then the permeability evolves linearly over 0.1 years to the same value as the argillite. The permeability is calibrated using the injection mass data. The EDZ is assumed to form instantly on borehole construction, and based on advice from IRSN, the EDZ has a radial extent of half the borehole radius. The time evolution of the properties of the EDZ is a key uncertainty but there are few data at Tournemire to constrain such evolution. As such, the properties and evolution of the EDZ are likely to be key factors in understanding the Step 2 models with respect to the experimental data.

Saturation-dependent suction pressure data were supplied to the teams by IRSN for both wetting and drying pathways. In the water injection test, any change in saturation is likely to be due to drying of the rock close to the tunnel and hence a van Genuchten type curve was fitted to the drying pathway data (Figure 2-44). The same van Genuchten parameters were also used for the relative permeability (Table 2-3).

The initial pressure in the argillite is assumed to be uniform at 600 kPa (gravity is ignored), which is hydrostatic pressure, and the argillite was assumed to be fully saturated. The model run starts when the gallery was constructed and a suction boundary condition is imposed on the gallery wall. According to IRSN, previous experience suggests it is reasonable to neglect disturbance from earlier activities at the Tournemire site, hence only the excavation of the local gallery is considered. As such, initial hydrostatic conditions and full saturation before the construction of the local tunnel was considered appropriate. The borehole boundary condition is turned on at the start of water injection, assuming that until this point, the plastic sheeting covering the borehole has prevented any desaturation of the borehole walls. Three different boundary conditions were applied at the borehole wall to investigate the extent to which the relative humidity in the borehole reflects that of the gallery (Table 2-4).

The void space is explicitly represented in the model with a volume of 0.0141 m^3 and injection commences with a head of 20 m for the first 2 hours and then the head drops to 1 m for the remainder of the simulation.

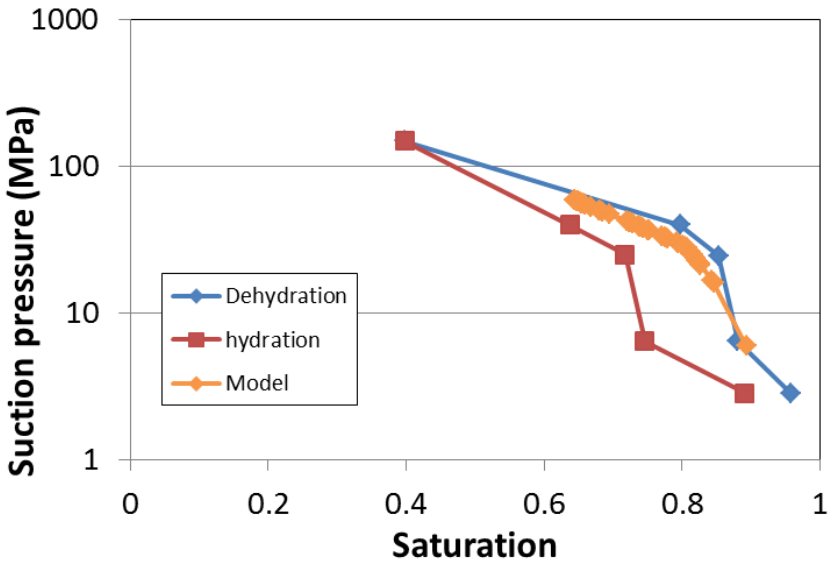

Figure 2-44: Suction pressure data and the van Genuchten curve used in the model runs (data from Millard and Barnichon, 2014).

Table 2-3: Hydraulic properties of the argillite.

Parameter	Value	Notes
Argillite / EDZ porosity	0.08	Millard and Barnichon (2014)
Argillite / EDZ van Genuchten 'n' parameter	1.5	Fit to data
Argillite / EDZ van Genuchten 'Pr' parameter	$3x10^7$ MPa	Fit to data

Table 2-4: Description of boundary conditions on the borehole wall.

Name	Boundary condition
Gallery RH	The borehole has the same suction boundary as the gallery, but is only effective once injection starts.
RH 100%	The air in the borehole is fully saturated so there is no flow of water across the wall of the borehole.
Mixing in borehole	Diffusion of water vapour in the borehole is represented explicitly in the model to calculate the relative humidity in the borehole, and hence the suction on the borehole wall.

2.5.3.3 Model results

The water mass injected into the model over the first two hours is 13.9 kg, which is similar to the amount needed to fill the void space in the model (14.1 kg), but is significantly less than that measured in the experiment (Figure 2-45). Part of the reason for the lower mass in the model is that the volume of void space reflects that given in Figure 2-37, but a second void space is referred to in the specification with no indication of where it is. The QPAC model also does not show any significant amount of water entering the rock during the first 2 hours. The difference in the Phase 1 water mass between the model and the data most likely reflects measurement error of the void space and therefore is not very useful in understanding the hydraulic properties of the argillite. For the remainder of the results discussion, the Phase 1 results are ignored and only the water injected during Phase 2 is considered.

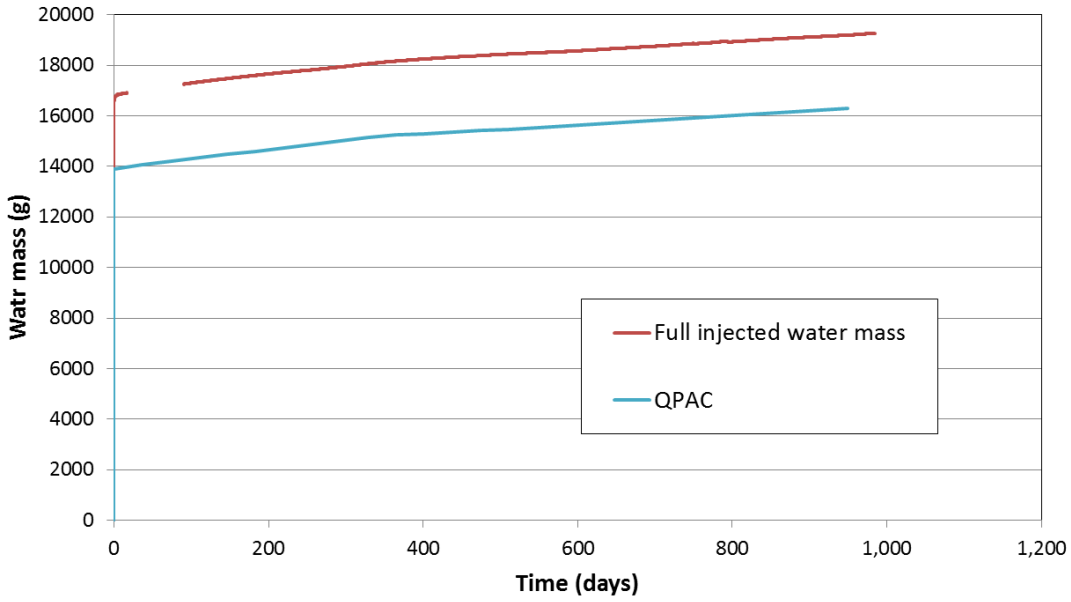

Figure 2-45: Water mass injected into the experiment and the QPAC model results for water flowing into the model from the injection boundary.

The Phase 2 results were calibrated to the data by changing the permeability of the EDZ and argillite. Using visual comparison, good fits were obtained with all three borehole boundary conditions, but the best fit was obtained when there was no flow to the borehole, representing a borehole relative humidity of 100% (Figure 2-46). Given the range of parameters and boundary representations that could be changed, there is no guarantee that the best fit calibrated result is completely unique, but from the analysis performed, it was the closest fit to the data that could be obtained for the physical process model being utilised.

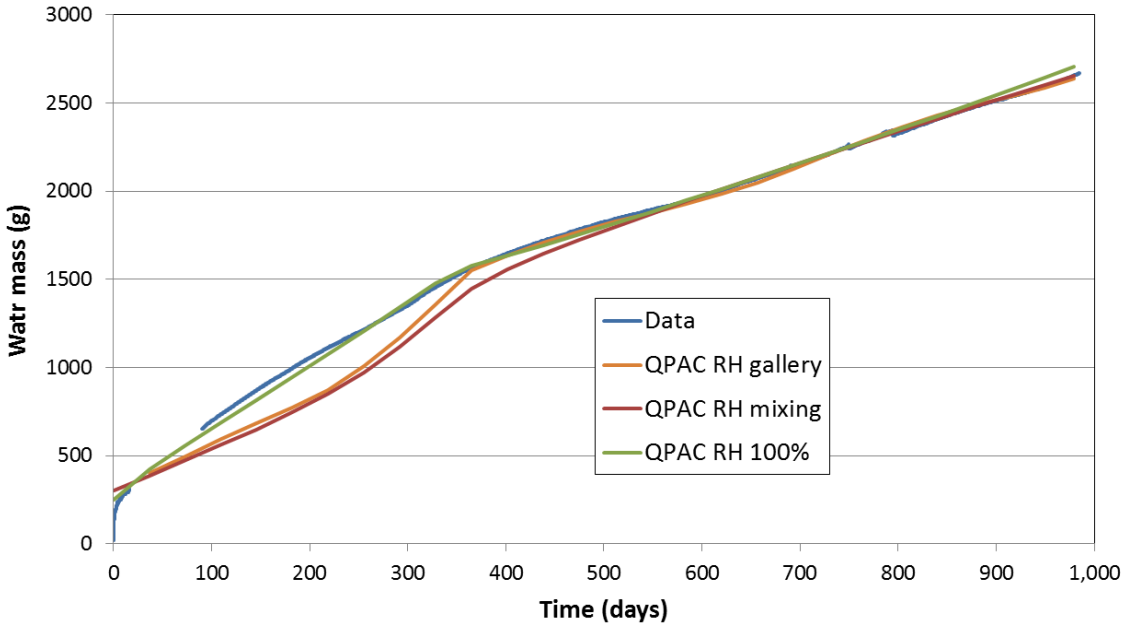

Figure 2-46: Water mass injected in Phase 2 for 3 models with different boundary conditions on the boreholes compared against the experimental data.

The permeability of the argillite and EDZ for each model is shown in Table 2-5. After 1 year, the EDZ permeability changes to the host rock permeability. Although the argillite permeability varies over an order of magnitude, all estimates are within the range of measurement (Millard and Barnichon, 2014). The main difference in the model results is that when the borehole has a relative humidity less than 100%, there is more significant drying in the EDZ around the borehole (Figure 2-47), and the pressure gradient and permeability controlling the flow into the rock are changing through time.

Table 2-5: Permeability of the rock and EDZ derived from the calibrated models.

Case	Rock permeability (m^2)	EDZ permeability (m^2)
RH 100%	$6x10^{20}$	$4x10^{-19}$
RH gallery	$4x10^{-21}$	$9x10^{-21}$
RH mixing	$5.3x10^{-20}$	$3.75x10^{-18}$

The modelling results show the best fit to the data when the relative humidity in the borehole is 100% implying no flow into the borehole. This model was built based on the data in the specification where the conditions in the borehole were not clearly stated. The borehole was covered with plastic prior to the injection, so it was possible that the plastic covering had remained in place. New information acquired after the modelling suggests that in fact the borehole was open to the gallery and it is very likely that the relative humidity in the gallery is significantly less than 100% (Barnichon, 2014, pers comm.). So although the 100% relative

humidity model is the best fit to the data, some more work needs to be done because the boundary condition does not appear to represent the reality of the experiment. The behaviour of the 'RH mixing' and 'RH gallery' cases is consistent with that shown by other teams, and as such, the inconsistency appears to be a conceptual issue, rather than a code or implementation problem. The extent, parameterisation and evolution of the EDZ appears to be an obvious candidate for further consideration because of all the features in the model, this is the least constrained and understood. This will be the focus for any future work under Step 2 for the water injection test.

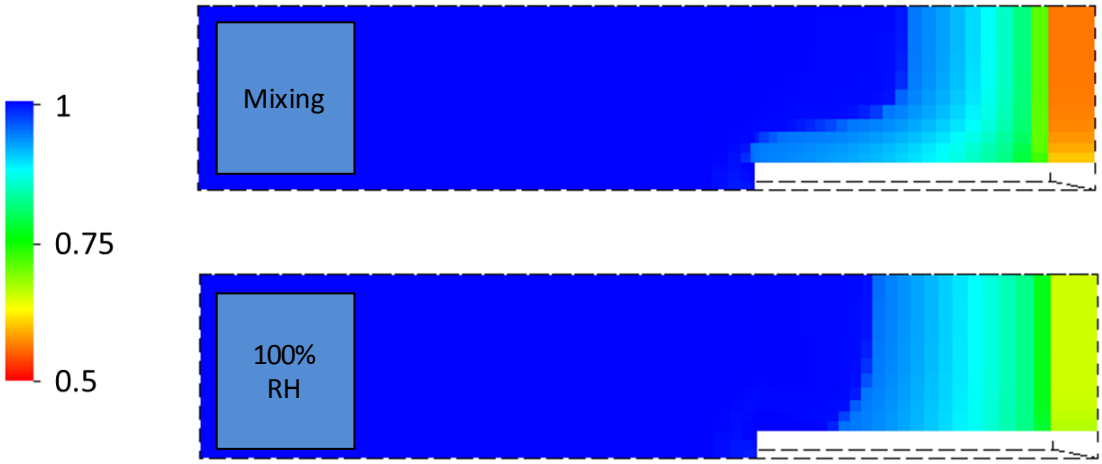

Figure 2-47: Water saturation 1 year after the start of injection for models with two different boundary conditions.

2.5.4 Pore pressure model

2.5.4.1 Data analysis

Measurement of pore pressure started on 12th January 2010, in pressure chambers that had an initial pressure of 400 kPa. The recorded pressures quickly move away from 400 kPa and follow longer time-scale trends that were attributed to the mechanical evolution of the host rock following construction of the gallery in the spring of 2008. The pressure in the argillite prior to construction of the gallery was assumed to have been hydrostatic, with a pressure of 600 kPa at the centre of the gallery.

The pressure data show very different trends in the horizontal plane compared to the vertical plane (Figure 2-48). In the horizontal plane, pressures are around or above hydrostatic, continuing to rise at 6 m radial distance, but falling to around 200 kPa at 3 m radial distance. This sort of pressure distribution is expected due to poro-elastic (hydro-mechanical) coupling when there is anisotropy in the mechanical properties of the rock. It is also noticeable that the oscillations due to the relative humidity in the gallery can be seen in the data from the horizontal plane.

Pressures in the vertical plane are more difficult to understand. It would be reasonable to expect a radial pattern of desaturation and hence pressures dependent on the radial distance from the centre of the tunnel. However, the data show little pressure dependence on the radial distance and instead pressure above the tunnel is around 100 kPa higher than pressure below the tunnel. From the information supplied on the host rock properties, there is no indication as to why the pressures above and below the tunnel should be so different, or why there is relatively little variation in pressure with vertical distance from the tunnel centre.

The data also show that the excavation of P1-A1 affected the pore pressures in the rock, but the main trends in the data collected are due to the excavation of the gallery. It was therefore decided to try and reproduce the general trends of the pore pressures following from excavation of the experimental gallery, before considering the additional complexity of the PT-A1 excavation.

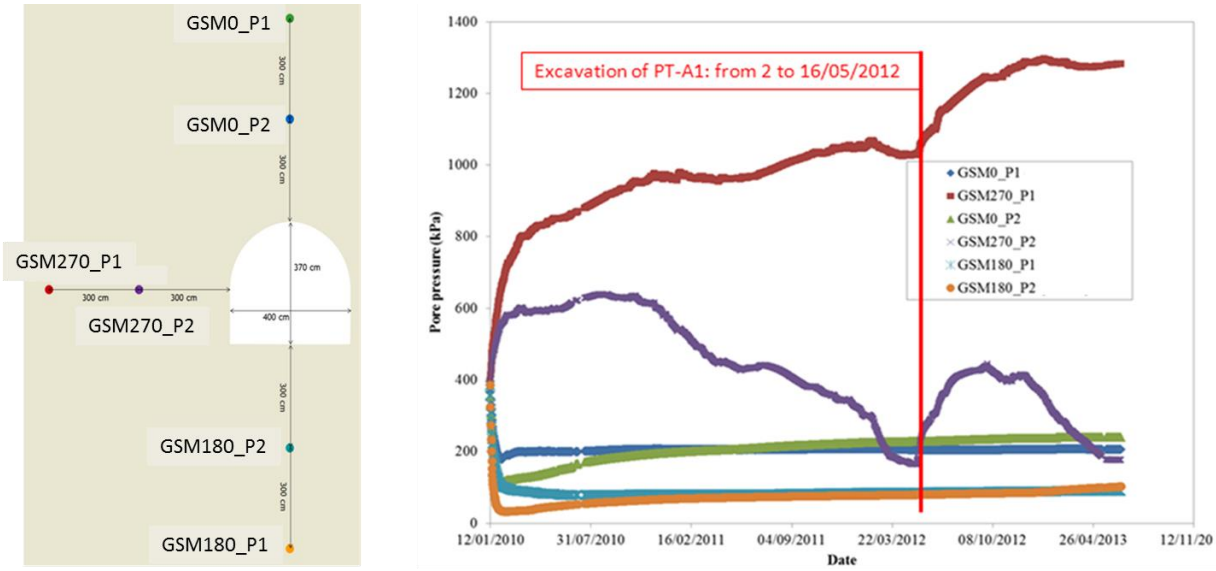

Figure 2-48: Location of pressure measurements relative to the gallery and the pressure data from these points (from Millard and Barnichon, 2014).

2.5.4.2 QPAC model

A 2D cylindrical model of the argillite surrounding the gallery was constructed, with the central part of the grid removed to represent the gallery (Figure 2-49). The rock mass was modelled out to a distance of 60 m because there is only 60 m of saturated rock above the gallery (i.e. hydrostatic pressure is 600 kPa).

The argillite mechanical properties were taken from the task specification (Table 2-6) and intrinsic permeability is used as a fitting parameter. Hydraulic properties are the same as the water injection test (Table 2-3). The argillite was assumed to deform elastically and the elastic properties were set to be anisotropic in the directions parallel and perpendicular to bedding. For simplicity, the bedding was assumed to be horizontal in the model, compared to a dip of 4.5° in the specification; a difference that was not expected to be significant. The confining stress tensor was also assumed to align with the vertical and horizontal directions, whereas in reality, σ_V is at 10° to the vertical. Again, this simplification was not expected to significantly change the model results. The long axis of the gallery is oriented at N 020° and the principle stresses are resolved into the orientation of the model.

The confining stresses are used as the boundary conditions to the model, resolved into the direction perpendicular to the boundary. However, the model actually extends vertically upwards to the ground surface, so a future version of the model might consider having a free surface at the shallowest part of the boundary. Due to the principle of superposition being valid for pure elastic deformations, this detail is only likely to be significant if non-linear elastic or plastic deformation is included in the model. The stress boundary conditions on the inner boundary of the model (i.e. in the gallery) are set to zero. Water pressures on the boundaries are set to hydrostatic pressure on the outer boundary and the cyclic suction based on relative humidity on the gallery boundary.

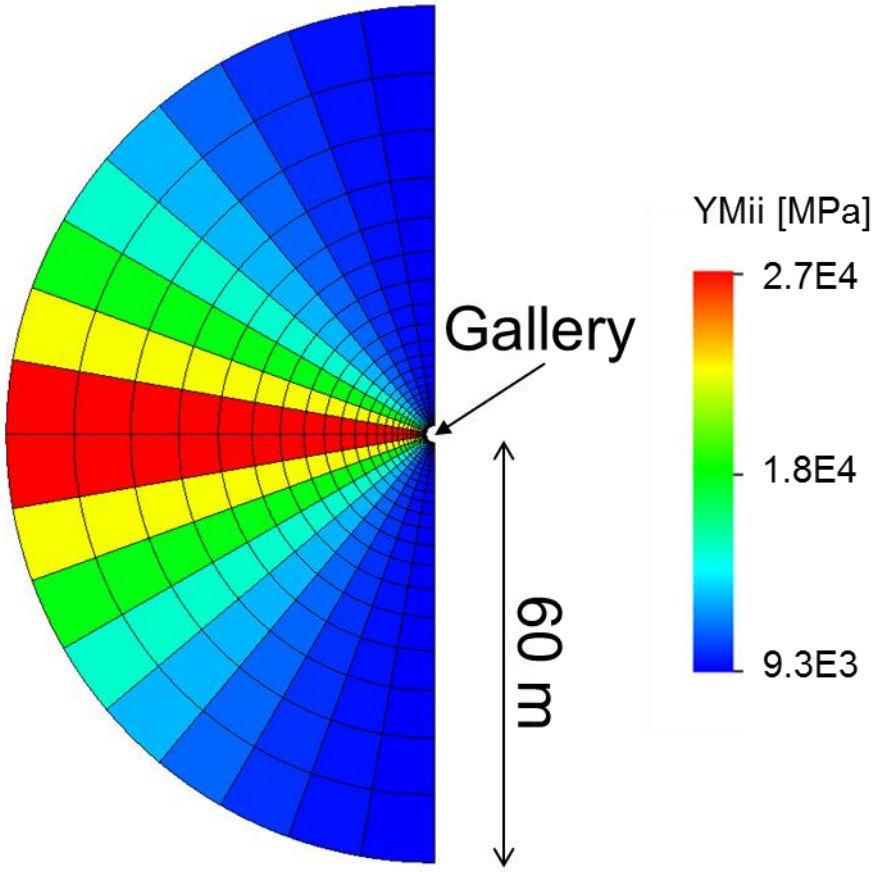

Figure 2-49: QPAC model grid coloured according to Young's Modulus in the radial direction (YMii).

Table 2-6: Mechanical parameters for the argillite.

Parameter	Value	Notes
Young's Modulus parallel to bedding	27.68 GPa	
Young's Modulus perpendicular to bedding	9.27 GPa	
Poisson's ratio parallel / parallel	0.2	
Poisson's ratio perpendicular / parallel	0.17	
Shear Modulus	3.94 GPa	
Biot coefficient	0.75	
σ_H	4 MPa	Oriented N 162°
σ_h	2.1 MPa	Oriented N 072°
σ_V	3.8 MPa	Oriented N 072°

2.5.4.3 Model results

Time zero in the model corresponds to the construction of the gallery in spring 2008. The pore pressure data measurement started in January 2010, so the start of the data should be compared to around 1.8 years in the model. The model produces the right trends in the horizontal plane (Figure 2-50), with pressures rising at 6 m radial distance (GSM270_P1) and falling at 3 m radial distance (GSM270_P2) and the oscillation caused by the yearly relative humidity cycles can be seen in both the data and the model. Some fine tuning of the model is required to improve the fit of the magnitude of the pressures, but the trends are encouraging.

In the vertical direction, the model does not correspond well with the data. This was expected since there are no processes in the model which could replicate the observations. The model results show a radial pressure gradient with the two measurement points at 3 m radial distance having lower pressure than the two measurement points at 6 m radial distance. There is also a vertical pressure gradient due to the hydrostatic gradient, with pressure above the tunnel lower than pressure below the tunnel. In the model, the pressures show yearly oscillations, but these oscillations are not reflected in the data. It is possible that the difference between the model and the data is due to an unexpected permeability structure in the argillite, for example a local vertical zone of high permeability, but there are no data to prove whether this is true or not. This theory will be tested in future model runs. Alternative suggestions put forward by the experimentalists (Barnichon, 2014 pers. comm.)

include some evidence of discontinuities around the vertical piezometers, which may cause the reliability of the data to be called into question.

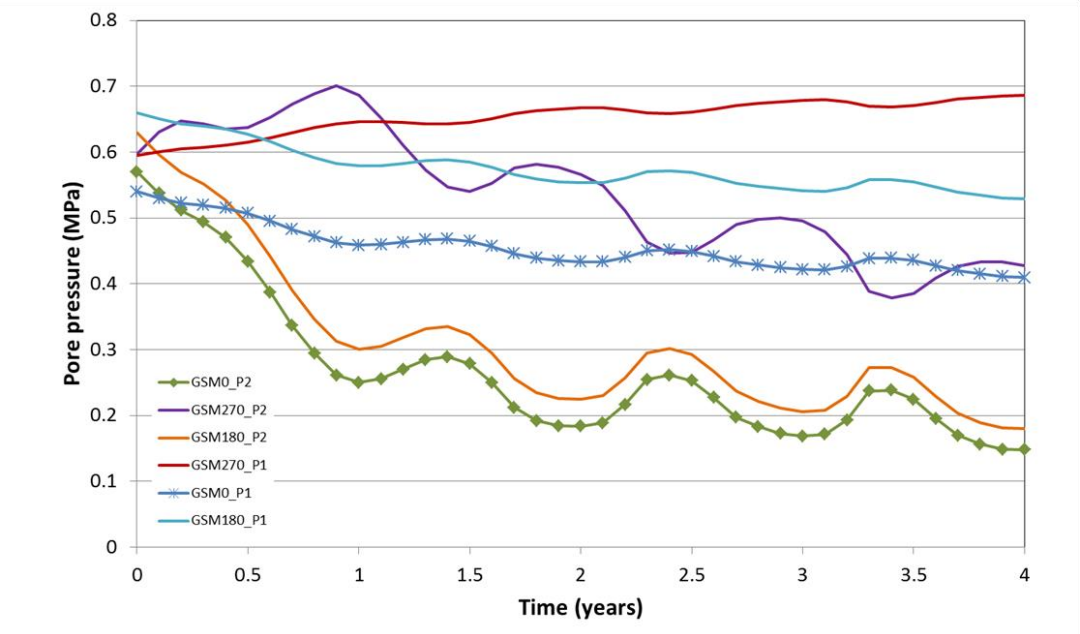

Figure 2-50: Modelled pore pressure in the argillite at the six locations shown in Figure 2-48.

2.5.5 Step 2 Summary

The RWM team has successfully contributed to Step 2 of Task A, including being one of only two teams to consider the optional part of the step (Section 2.5.4). The Task A management was pleased with the contribution of all the teams, as many different approaches were taken enabling interesting comparison of results. Despite the range of approaches, the general conclusions and parameterisation amongst the teams were consistent.

The work demonstrated that whilst the overall trends of the water injection test could be understood, some of the detail of the data is difficult to understand, in particular the cause of the change in injection rate after a year of injection. This work also showed it was possible to produce very good model fits with a relatively simple hydraulic model, although some improvements are to be considered to account for additional information on the condition of the borehole. The lack of constraint of behaviour in the host rock, especially the EDZ, contributes significantly to the conceptual uncertainty for this case.

The pore pressure model was able to reproduce the general character of the pore pressure data in the horizontal plane but did not match the data in the vertical direction, because the data do not show a radial pressure distribution. Some additional modelling will be carried out to introduce a permeability structure into this model, to assess whether this might provide an explanation for the data. There was general consensus amongst the teams and task management that the pore pressure data in the vertical direction are difficult to explain conceptually, and there might be other explanations for the behaviour of the vertical data, such as the presence of discontinuities or currently unidentified vertical structures with enhanced permeability.

As most teams have produced a reasonable fit to the water injection test data, the teams will now be asked to move on to Step 3. As preparation for Step 3, a small amount of additional work on Step 2 will be conducted in light of additional information on the borehole for the water injection test and discussion with the task management about the permeability structure of the argillite. Both of these issues may have a bearing on the Step 3 modelling and hence are useful to consider further.

2.6 Task A Summary and Way Forward

A considerable amount of work has been performed examining and implementing possible constitutive models of bentonite suitable for hydro-mechanical applications. The work has facilitated a greater understanding of the BBM approach with its associated strengths and weaknesses and proposed two alternative hydro-mechanical representations of bentonite that, unlike the BBM (Gens and Alonso, 1992), closely relate the hydraulic and mechanical characteristics of bentonite to give models that attempt to be more physically coherent. These two approaches (one implemented in QPAC (ILM) and one in OGS (Non-linear elastic model)) have approached the problem from different perspectives, but converged on solutions that have many aspects in common, which result in considerably fewer free parameters than exhibited by the BBM. The net result is that the RWM team has a version of BBM implemented in QPAC and two simpler alternative models available for use in Step 3, if required. However, it should be noted that the experience of implementing and applying these models suggests that use of different bentonite mixtures and, to a certain extent, different geometries, will require additional experimental work to calibrate these models. It is also the case that all of these models (including the BBM) are very much research level models and there is a general need to build confidence that these process models can be applied more generally to compacted bentonite.

The work on Step 2 has provided very useful preparation for Step 3 and demonstrated that good, useful models of complex systems can be constructed using relatively simple models.

Overall the RWM work under the task appears to be well placed to attempt Step 3 (modelling a full-scale emplacement test) and the experiment will provide an excellent source of data to test the bentonite models developed under Steps 0 to 1.

3 Task C – THMC in single fractures

3.1 Task Overview

The RWM team is one of 6 teams contributing to the technical work of this task:

- Chinese Academy of Sciences (CAS);
- Imperial College London (PhD student), funded by RWM;
- Quintessa and University of Edinburgh, funded by RWM;
- Technical University of Liberec, funded by RAWRA (Czech Republic);
- UFZ Leipzig, funded by BGR, Germany;
- US NRC (internal team).

Consistent with Task A, only the results of the Quintessa and University of Edinburgh are reported here, but comments and comparisons with other teams' work is made where appropriate.

3.1.1 Experimental Overview

The coupling of chemical, hydraulic, thermal and mechanical processes for fractured rocks is an extremely complex area of scientific research that may have a significant bearing on the potential design and performance of radioactive waste disposal facilities. The purpose of Task C1 under DECOVALEX-2015 is to (from Bond, 2013b):

1. Investigate and mathematically model the results of the two experiments described by Yasuhara *et al*. (2006) and Yasuhara *et al*. (2011), which observe coupled THMC responses in single fractures.

2. Investigate, develop and test robust process models for the representation of coupled THMC processes in fractured rock by using the experimental data and the results of the modelling work above.

The emphasis of this work is to gain understanding of possible physical process models that can be used to explain the results of the experiments. The two experiments are well described in the two references given, hence only a summary is provided in Sections 3.1.2 and 3.1.3.

The experiments consider hydraulic and chemical analysis of water flowing through laboratory samples of novaculite (Yasuhara *et al*., 2006) and granite (Yasuhara *et al*., 2011). In both cases, the fractures had been induced by the experimentalists, deionised water was used as the permeating fluid and the samples were under a significant confining pressure. The 'fresh' nature of the fractures and the use of deionised water ensure a rapid initial chemical interaction between the fluid and the rock. The artificial nature of the fractures also means that mechanical effects may be significant early in the experiment; hence there is a need to be careful to separate the chemical and mechanical effects as far as practicable. It

is also clear that there is significant uncertainty in all aspects of the parameterisation of the system and as such it will be important for the task to be able to understand the significance of different teams' choices regarding approaches to processes and associated parameterisation.

Of the two experiments, the novaculite case is geochemically much simpler than the granite case and is much better constrained in terms of initial and final fracture aperture distribution. In contrast, in the granite case, single measures of bulk 'aperture' are derived from the flow data and very little other fracture structure data appear to be available, aside from some interesting SEM data. As such the granite case has considerably greater uncertainty both from the relatively complex geochemistry and from the relatively sparse fracture structure information.

The experimental setup and results for each experiment are discussed briefly in the following sections.

3.1.2 Novaculite Experiment

The experiment consists of an artificially fractured novaculite (99.5% Quartz) placed in a hydraulically sealed pressure vessel (Figure 3-1), around which a constant confining pressure of 1.72 MPa was applied (at which the boiling point of water is approximately 200°C). Deionised water is applied through the sample and differential pressures measured at the outlet and inlet. The whole apparatus can be heated, hence raising the temperature of the water, sample and pressure vessel.

Prior to assembly, both sides of the fracture were scanned using a 3D laser scanner system, which gave measurements on a square grid of size 0.05 mm across the 50.0×89.5 mm fracture surface. This creates approximately 1.6 million datum points per surface. Statistical analysis of the fracture topography was not performed by Yasuhara *et al*. (2006); however this will be considered in future work as part of DECOVALEX Task C1.

The experimental procedure was relatively complex, involving changes to both temperature and flow rates with time (see Figure 3-2). It can be seen that the early part of the experiment is isothermal, with only variations in water flow rates. The reversal in flow direction allowed consideration of flow with a different stress distribution. The variations in aperture and differential pressure are quite large in the isothermal phase.

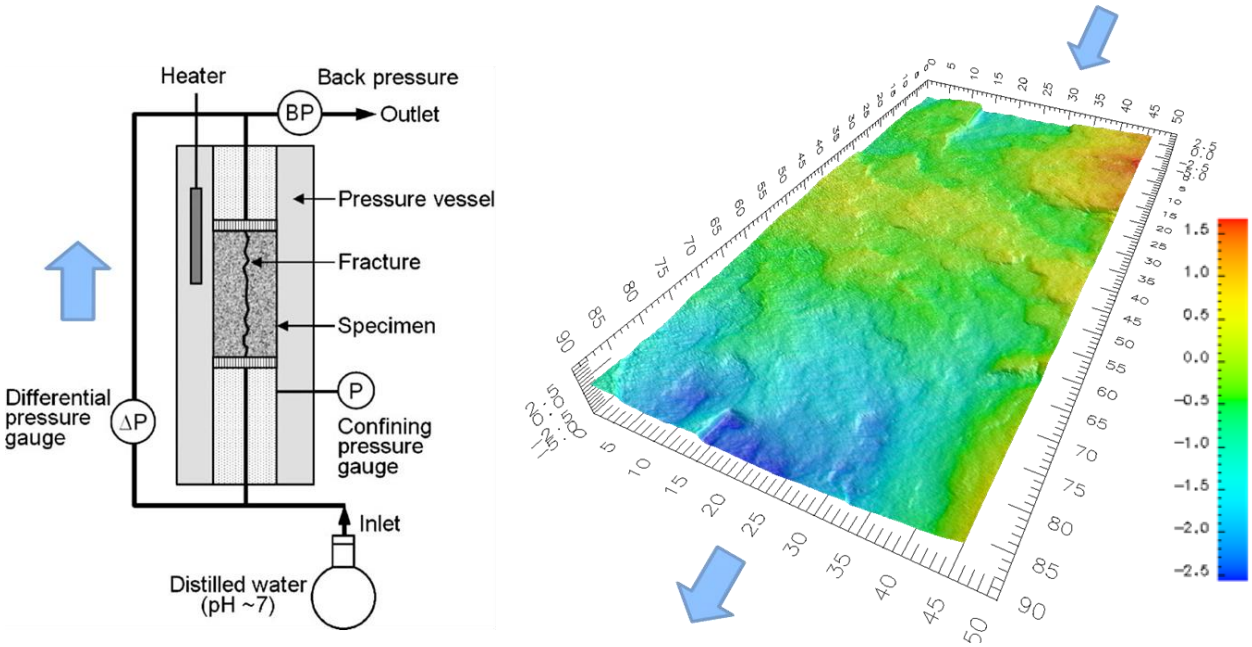

Figure 3-1. Schematic illustration of the experimental apparatus for the novaculite experiment (left, from Yasuhara *et al.*, 2006) and the measured topography of the fracture surface (right, no vertical exaggeration). Blue arrows indicate the normal flow direction of water. Note that the confining fluid is not shown explicitly on the schematic diagram.

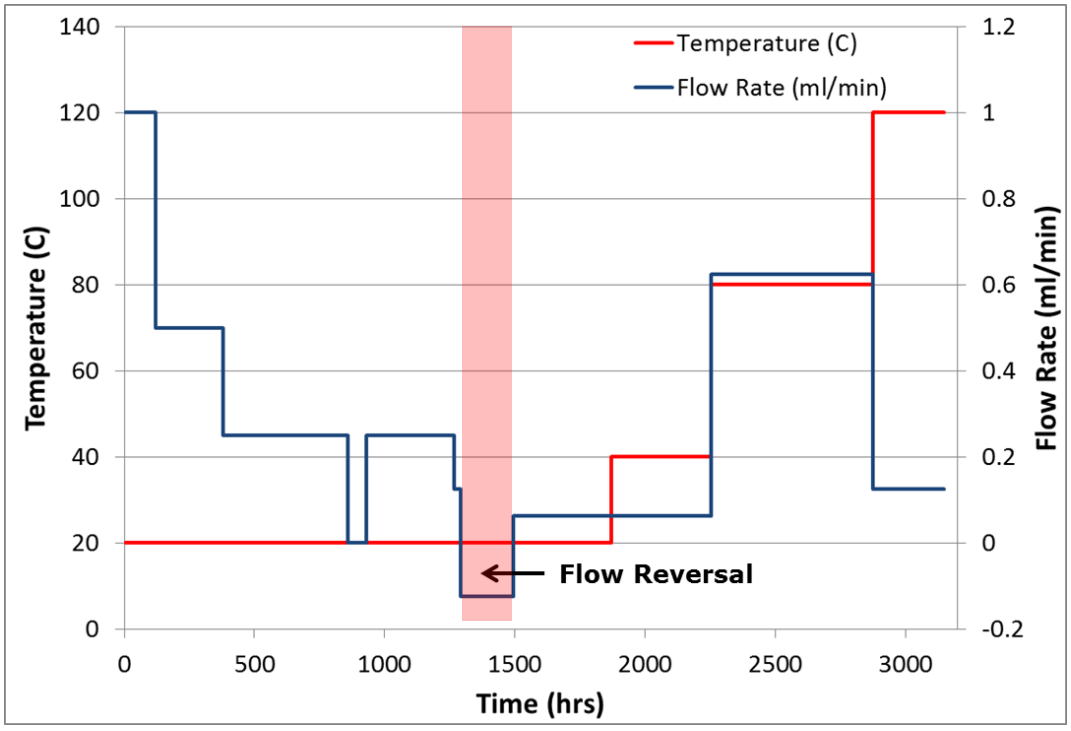

Figure 3-2. Temperature and flow rate across the sample with time. Flow reversal period is highlighted in red.

Overall the available data for the experiment are:

- Initial fracture surface topography (both surfaces – see above).
- Input water flow rates with selected pH measurements.
- Outflow water silicon concentrations (ppm) and selected pH measurements.
- Differential water pressure across the sample.
- Confining pressure (constant at 1.72 MPa).
- Post experiment X-Ray CT scan of the sample.
- Post-experiment aperture information from Wood's Metal injection.

The evolution of differential pressures and silicon concentrations are shown in Figure 3-3 and Figure 3-4. It is clear that there are strong correlations between flow rate changes and the implied hydraulic aperture and that the influence of temperature changes is particularly strong above 40 °C. However there is considerable 'noise' in the silicon concentrations and very little in the way of trend or sharp changes during the initial constant temperature period. It is unclear to what extent this 'noise' masks any changes caused by the flow rate changes when the temperature is held at 20 °C.

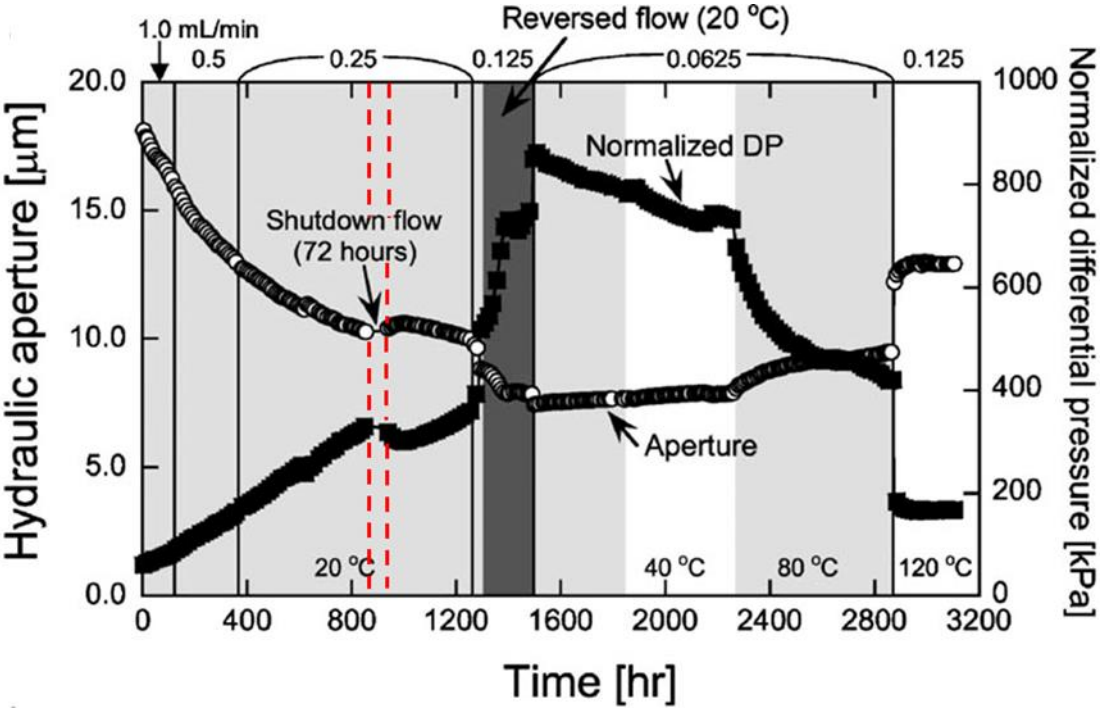

Figure 3-3. Normalised differential pressure across the sample and implied hydraulic aperture (using the parallel plate cubic law) for the novaculite experiment (adapted from Yasuhara *et al.*, 2006). Grey/white shading indicates temperature changes.

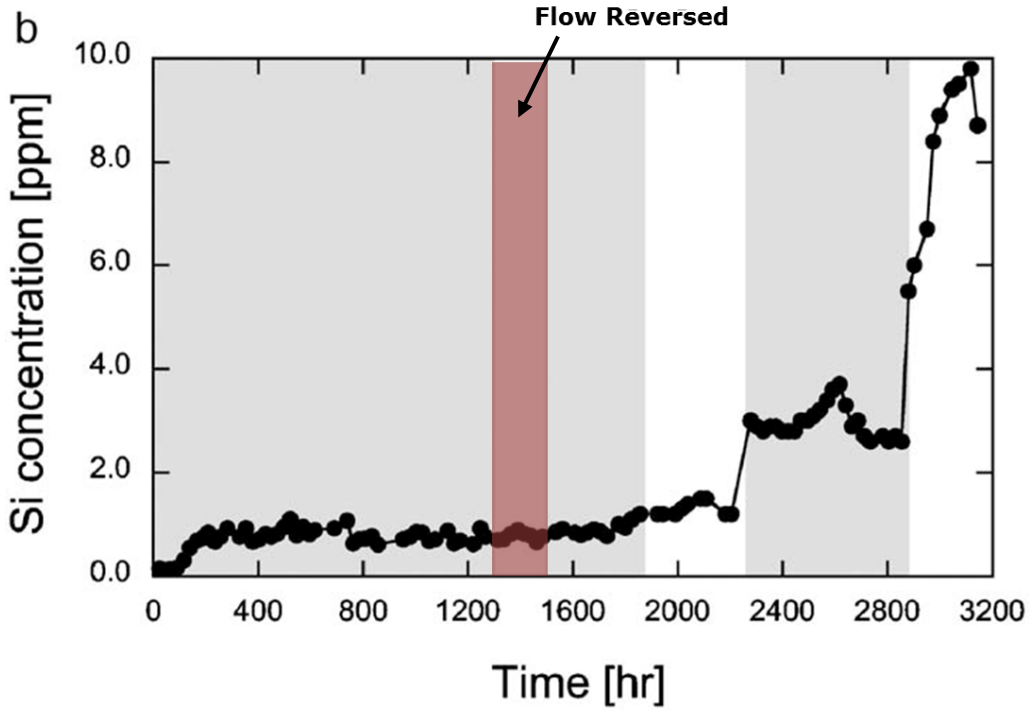

Figure 3-4. Measured Si concentration in the outflowing water for the novaculite experiment (adapted from Yasuhara *et al.*, 2006). Flow reversal period is highlighted in red. Grey/white shading indicates temperature changes as per Figure 3-3.

3.1.3 Granite Experiment

The granite experiment is similar to the novaculite experiment, but with a few important details:

1. The experiment consists of three Mizunami granite samples each with an artificial fracture.

2. Each sample has a different combination of applied thermal load, confining pressure and differential water pressure. Maximum temperatures were 90 °C. Overall the flow and temperature evolution applied to the sample is much simpler than for the novaculite case.

3. There are no topography data for the fracture before the experiment started; only SEM data of the fracture surfaces upon completion of the experiment.

The task leadership decided that, because of the increased geochemical complexity of the granite experiment relative to the novaculite, as well as the absence of fracture topography data, the granite experiments would be deferred for consideration until later in the task (see Section 3.1.4). Hence, these experiments are not described further in this report.

3.1.4 Task Structure

A fuller discussion of the task structure and the reasoning behind the approach is given in Bond (2013b). In summary, the following structure has been adopted:

- **Step 0**: Basic benchmarking - Novaculite:
    - Using primarily fracture topography data from Yasuhara *et al*. (2006), to reproduce the observed flow rate at the start of the experiment only. The objective here is to attempt, if possible, to reconcile the fracture topography data with the observed initial flow rates and the initial conditions for the fracture.
    - Represent simple batch experiments of silicate dissolution in deionised water with no flow in a notional 10 μm aperture fracture and no mechanical coupling at 20 °C, 60 °C and 120 °C.
    - Construct a simple 0D (single volume, lumped parameter model) or 1D (representing the fracture as a single pipe) representation of the fracture with a constant starting aperture up to the start of the first reversal (1292 hr), attempting to reproduce the major features of the experimental results.
- **Step 1**: Attempt to model the novaculite case up to the end of the reversal of flow (isothermal) in 2D (if possible) using fully coupled formulations. Teams to attempt to understand the relative impacts of chemical dissolution versus early mechanical evolution. Teams should also attempt to understand the consequences of coarse or fine representations of the fracture surface.
- **Step 2**: Model the novaculite case up to the end of the experiment. Impacts of temperature are clearly significant in this phase (non-isothermal). Again sensitivities to chemical and mechanical processes are of interest.
- **Step 3**: Basic benchmarking – Granite
    - Represent simple batch experiments of granite dissolution in deionised water with no flow in a notional 10 μm aperture fracture and no mechanical coupling at 25 °C and 90 °C. Compare dissolution rates, solubilities and pH between teams. Teams to optionally look at the impacts of different surface area models as dissolution progresses.
- **Step 4**: Attempt to model the granite case during the initial isothermal (20/25°C) period. Teams to attempt to understand the relative impacts of chemical dissolution versus early mechanical evolution.
- **Step 5**: Attempt to model the granite case over the full experimental period (20/25°C and 90 °C).
- **Step 6**: Application (Optional). The purpose of this exercise is to test the degree of difference between long-term predictions using well-constrained models calibrated against short-term data. The specification for this work has yet to be defined.

The proposed schedule for the project is given in Figure 3-5.

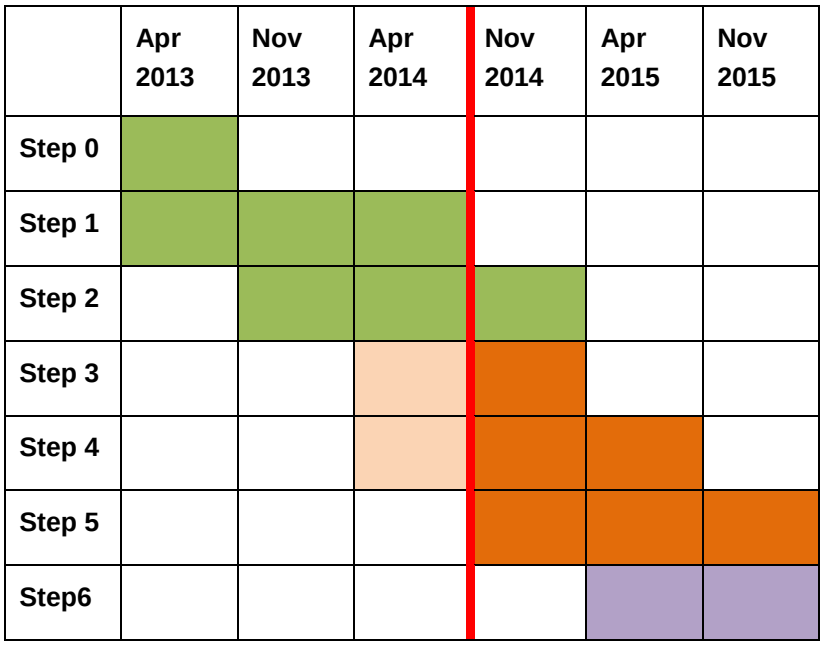

Figure 3-5. Task C1 schedule (from Bond, 2013b). Green cells indicate novaculite steps while the orange cells indicate granite steps. The end of April 2014 is marked with a red line, which is the current point of progress in the project.

It should be noted that the effective start to Task C1 occurred relatively late due to the scope of work not being defined until November 2012. As such, Task C1 is currently a little behind Task A in terms of progress.

3.2 Year 1 Status Summary and Approach

At the end of year one, the RWM team had successfully completed Step 0 by participating in the simple geochemical benchmarks and producing initial models for Step 1 using both a homogenised (QPAC) and discretised (OGS) method. It was decided that the approaches were complementary and provided a useful cross check.

The approach for year 2 was to continue with the two different strands of modelling (discretised and homogenised methods – see Bond *et al*. 2014), but to investigate a wider range of potential processes including 'Stress Corrosion' (see Sections 3.3.1 and 3.4.1), rock matrix diffusion and channelization. The objective was to complete Step 2 by the end of the year and therefore be in a position to start the granite experiments in year 3, if the task management deems it appropriate.

3.3 Step 1 and 2 using the discretised approach

3.3.1 Approach and Overview

The approach of the team to the problem using the 'discretised' approach has been to further develop computational and mathematical methods to simulate the THMC response of the fracture behaviour. To achieve this, the finite element simulator OpenGeoSys (OGS; Kolditz *et al*., 2012) has provided a computational platform to develop ideas and concepts, tested against the experimental data and observations.

A hybrid numerical and analytical solution discussed in more detail in Bond *et al*. (2014) is key to the implementation in OGS, developed by UoE. This is chosen to avoid the computational demands for fully solving the mass balance equations for solute transport and the energy balance equations for stress. Additionally, by using the advantages of the different techniques, upscaling in terms of time and the inclusion of sub-grid-scale information can be included in the solution whilst still maintaining numerical stability. The elements of the solution scheme are listed below and the structure presented in Figure 3-6.

1. (H) Numerical evaluation of the pressure distribution in the fracture
2. (M) An analytical solution for mechanical behaviour
3. (C) An analytical solution for chemical behaviour

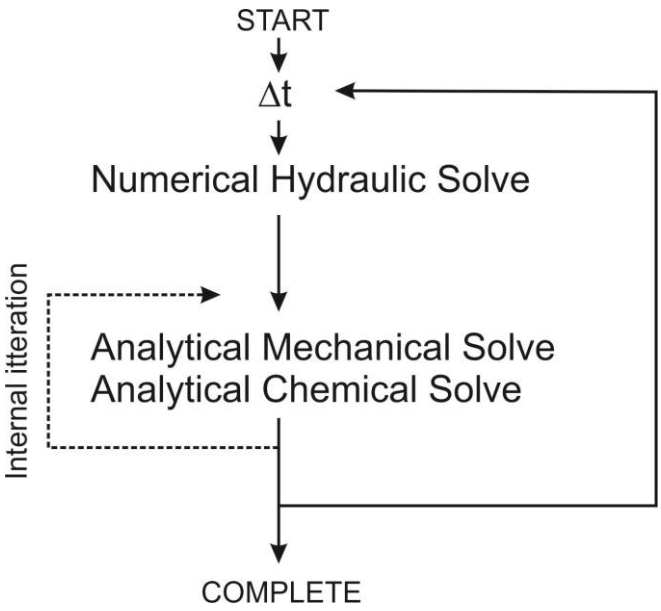

Figure 3-6. Schematic diagram of solution scheme.

In the period April 2013-2014 the following areas were developed. More details are given in the following pages.

Under the (M) analytical solution

- Implementation of a critical stress value for the pressure solution of quartz with consideration of fractal geometry.
- Implementation of non-linear pressure solution of quartz.

Under the (C) analytical solution

- Non-kinetic estimation of parameterisation for the completion of step 2.
- Development of a sub-time step method for kinetic controlled dissolution.
- Application of local velocity vectors to interpret the kinetic behaviour of the fracture surface.
- Approximation of sub-grid-scale channel flow.

In addition, a general consideration as to the value and usefulness of discrete data from the fracture surfaces and a statistical representation of the fracture surface was undertaken.

Several phenomena were considered and the impact on the model fitting of the experimental results investigated. The procedure was kept more at an exploratory nature than a discrete parameter fitting exercise due to data uncertainty. These processes are illustrated in Figure 3-7.

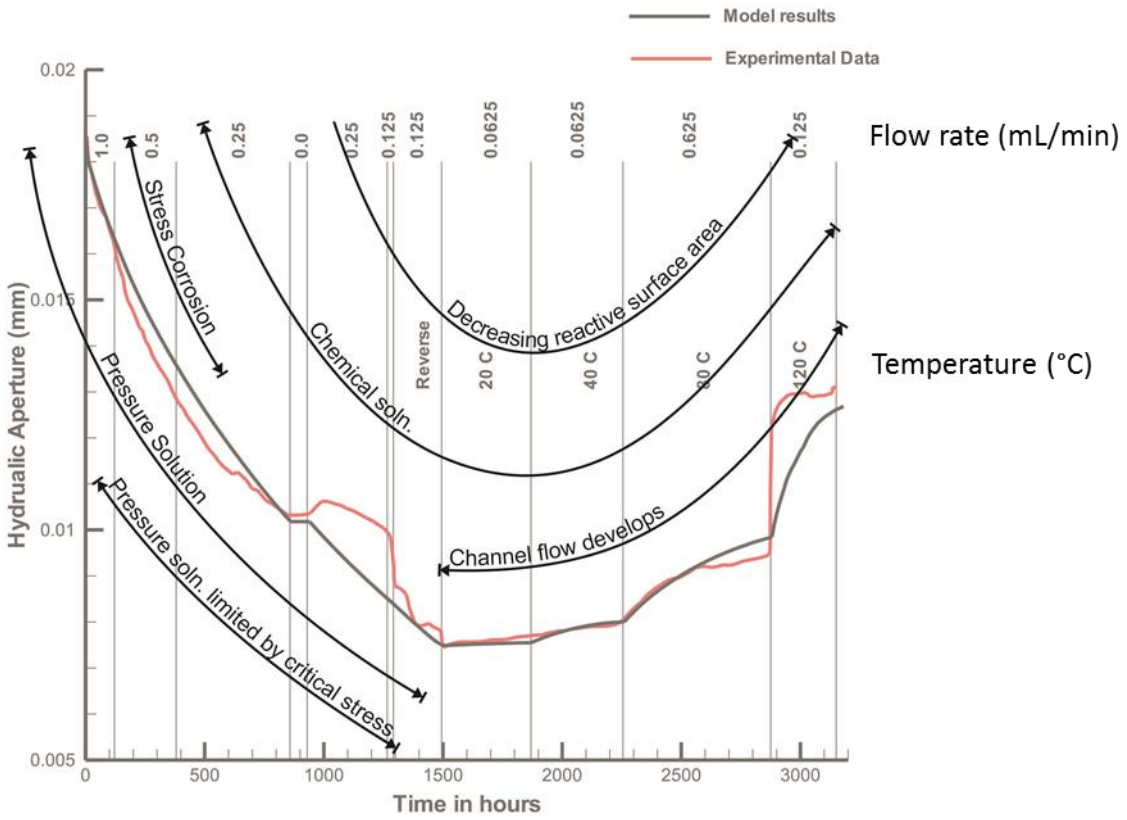

Figure 3-7. Illustration of the components of physical phenomena included in the OGS model by UoE (except stress corrosion).

A fundamental division in the processes operating during the experimental work was considered to occur at about 1500 hours from a pressure and chemical dissolution regime to a chemical solution only controlled regime.

The division between these two regimes was considered to be due to the effect of a critical stress across contacts under which further pressure solution does not occur.

3.3.2 Implementation of a critical stress value for the pressure solution of quartz with consideration of fractal geometry.

Contact stress, $\sigma_{c,}$ is defined as the normal stress across the fracture, σ_n, carried by the contact area of the fracture, *CA* with a fluid pressure of u.

$$\sigma_c = \frac{\sigma_n - u}{CA} \tag{28}$$

A pressure solution limit $\sigma_{l,}$ is discussed by Yasuhara *et al*., (2004) and Revil (1999). Under this pressure no further pressure solution can occur. This is given by

$$\sigma_l = \frac{E_m\left(1-\frac{T}{T_m}\right)}{4V_m} \tag{29}$$

where E_m and T_m are the heat and temperature of fusion respectively (E_m = 8.57 kJ mol^{-1}; T_m = 1883 K for quartz), T is the current temperature in kelvin and V_m is the molar volume 2.27x10^{-5} m^3/mol. This limiting pressure can be calculated to be approximately 80 MPa.

During the mechanical simulation, the contact stress at an element level was calculated, and compared to this critical stress value. A simple evaluation under the experimental conditions demonstrates that, at the scale of the discretisation, the contact stress would be of the order of 30 MPa for a contact area of 5%. However from the experimental results it was clear that pressure solution was continuing at up to circa 20% of the fracture area being in contact. It was clear that in the discrete representation being used for the simulation of the fracture surface, contact stresses in excess of the critical stress at contact areas up to 20% were operating. This sub-grid scale process must be included in the model representation otherwise the simulation of pressure solution would cease prematurely, as demonstrated in Figure 3-8.

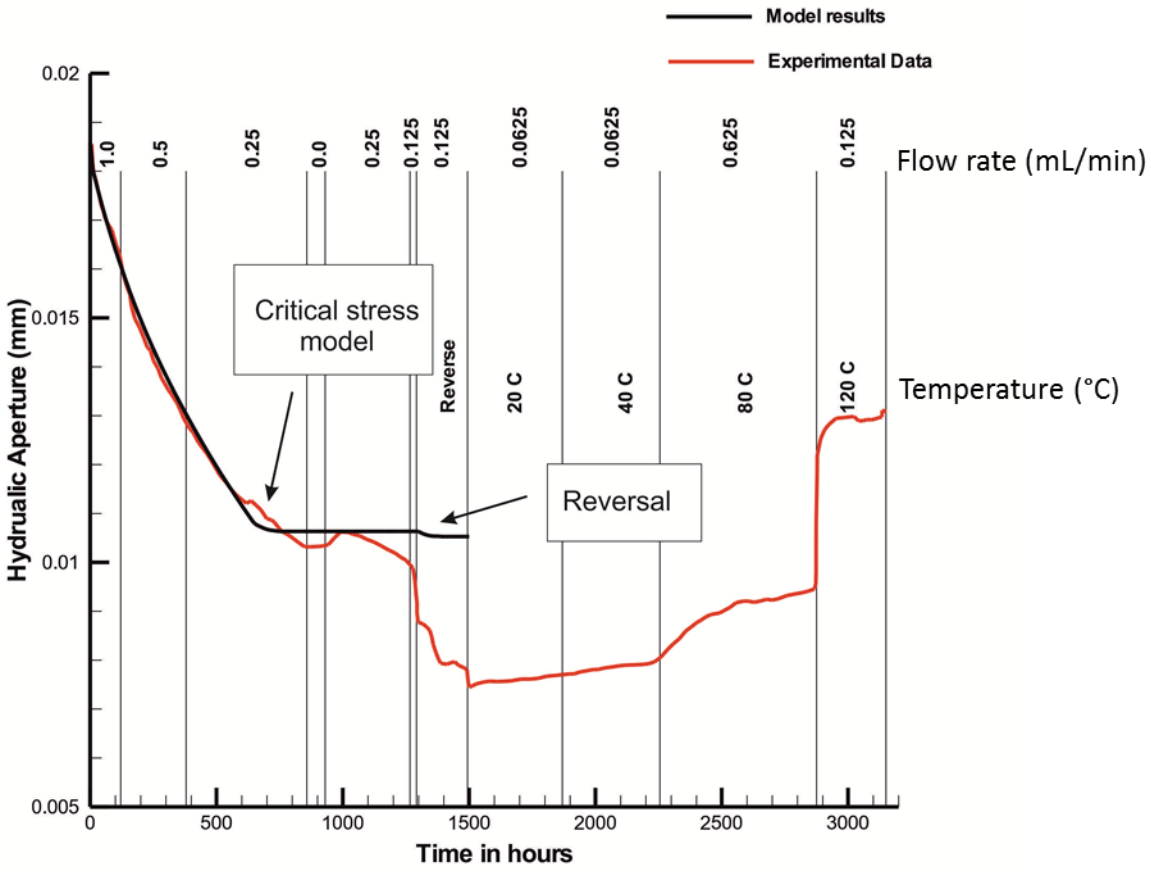

Figure 3-8. Impact of introduction of a critical stress for pressure solution.

To account for this discrepancy the concept of fractal geometry for the statistical distribution of the contacts of the fractures surface (Figure 3-9) was introduced. Here it is assumed that the statistical characteristics of the geometry of the fracture surface contact are independent of length scale, and the control at the scale of discretisation is the same as the control at the element scale. In practice it is assumed that the elements of the fracture surface which are in contact with each other also display a minute surface variation and roughness, but no permeability. This allows the critical stress value to be expressed as

$$\sigma_c = \left(\frac{\sigma_n - u}{CA}\right)\left(\frac{\xi}{CA}\right) \tag{30}$$

where ξ is set to be 1 m^2 for dimensional consistency. This allows a reasonable fitting of the curve by assuming a critical stress value of circa 30 MPa.

Although below the calculated limiting pressure value of 80 MPa, the use of sub-grid scale information has significantly closed the gap between the modelling approximation and the experimental results. Further changes to (30) could include factors to account for the discrete geometry of grain to grain contacts. However the data to validate this are not available in the experimental work undertaken.

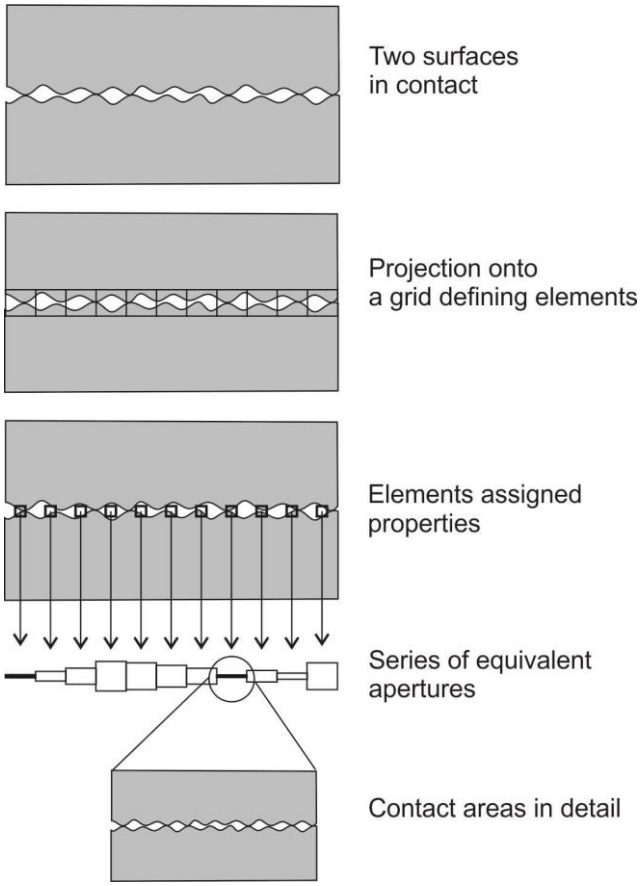

Figure 3-9. Assumption of fractal geometry of fracture surface to evaluate the critical pressure solution stress.

3.3.3 Non-linear pressure solution of quartz.

The pressure solution was also further developed by consideration of the fractal geometry as above:

$$\sigma_c = \left(\frac{\sigma_n - u}{CA}\right)\left(\frac{af(CA)}{CA}\right) = \left(\frac{\sigma_n - u}{CA^{(2-n)}}\right)\xi^{(1-n)} \quad (31)$$

$$\Delta e = -2\alpha_p k_+ V_S(\sigma_c - u)^b \Delta t \quad (32)$$

where $f(CA)$ represents some cross-sectional flow area reduction causing reduction in solution as a result of the geometry of the surface. The definition of equation (32), the change in hydraulic aperture (Δe) over a time interval Δt due to pressure solution, is discussed in Bond *et al*. (2014) and so is not discussed here further. In this work it was found that setting b=1 gave an appropriate aperture response. The calibration parameter *n* could be used to alter the curvature of the hydraulic aperture curve to some degree; a general improvement to the fit could not be obtained by changing this parameter, therefore a value of ~1 was preferred.

3.3.4 Kinetic control on the evolution of the fracture surface

Dissolution of a mineral is often represented using the "Transition state theory" (Eyring, 1935):

$$\frac{dS}{dt} = A(S)k_+\left(1-\frac{Q}{K}\right) = A(S)k_+\left(1-\frac{c}{c_s}\right) \quad (33)$$

where S is the quantity of a solid of interest (mol), t is time (s), $A(S)$ is the mineral reactive surface area (m^2), k_+ is the is the kinetics constant for dissolution or precipitation (mol m^{-2} s^{-1}), Q is the ion activity product for the solid of interest (dimensionless) and K is the equilibrium constant for mineral dissolution (dimensionless). Because the system is dilute, equation (33) can also be expressed as shown using c and c_s as replacements for *Q* and *K* respectively, where c is the concentration (molal) and c_s is the solubility limit (molal). The geochemical benchmark (Bond *et al*. 2014) provides a good indication as to the timescales using literature values for the kinetic controlled development of the concentration of Si within the fracture as a consequence of dissolution. At 20°C, of the order of 100 days is required for a concentration to be reached which would start to inhibit dissolution. At 120°C, noticeable influence of concentration is seen after a contact for a period of ~1000 seconds (10^{-2} days).

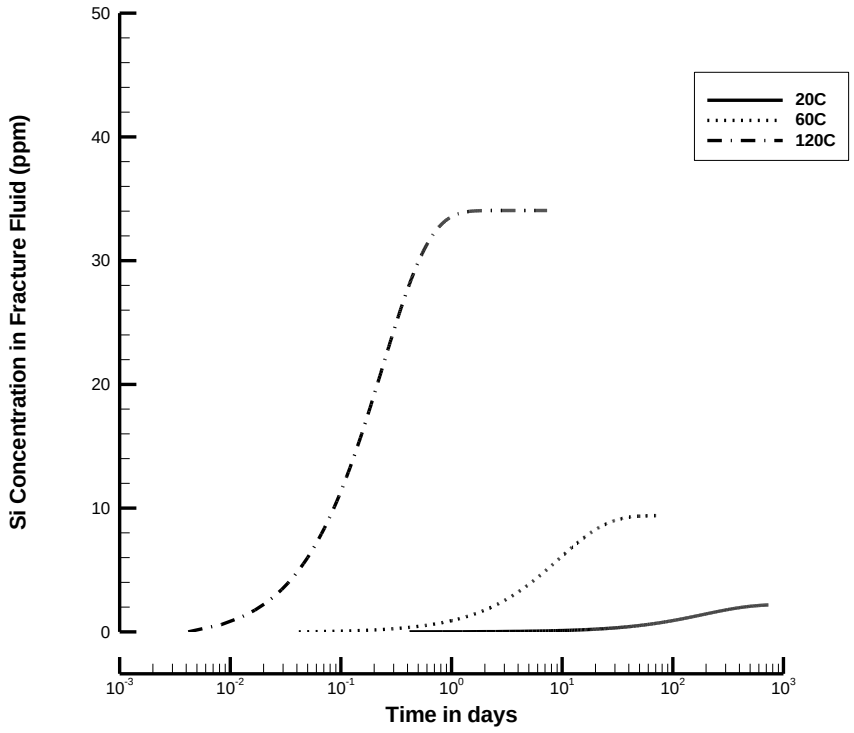

Figure 3-10. 7 Rate of concentration increase within a fracture of similar dimensions to the modelled fracture

The flow velocity within the fracture is such that the residence time of the fluid can be considered to be of the order of 50 seconds. However it is possible that due to the heterogeneity within the fracture surface, some lower permeability and less well connected areas of the fracture surface allow much larger residence times. This therefore means there

is a requirement to include the kinetic effect, particularly at higher temperatures, in the evaluation of the results.

Numerical simulation of advective dominated transport is controlled by the Courant number (Courant *et al*., 1928), which expresses the stable time control of the simulation as a function of the advective velocity and the discrete size of the grid used for the coordinate system of the numerical simulation. For this case, the flow velocity is such that a stable time stepping scheme to capture the advective transport would require time discretisation of the order of a few seconds. However given that the experimental conditions remain constant over several days, evaluation of these periods of time in terms of seconds would prove computationally expensive.

Therefore a time stepping scheme coupled with the advective flow scheme was developed that allows both the development of the concentration profile and the overall influence of the concentration profile on the fracture dissolution rate with time to be captured, without requiring micro-time stepping.

For the numerical solution a time step is chosen independently of the non-linear process of dissolution. For instance, considering dissolution at 120°C, a time step of 10 hours may be taken to evaluate the concentration profile. The amount of fluid passing through an element within the fracture during this period of time is evaluated. The average contact time of the fluid with the element is calculated and used to evaluate the amount of mass dissolved into this package of fluid in the given time.

Kinetic dissolution is non-linear and approximating this with a linear function would not reflect the true relationship . However, when considered in a log-log evaluation, the dissolution can be seen to become approximately linear (Figure 3-11). To better represent the kinetic dissolution, it was controlled by a sub-time step iteration carried out on a log based evaluation of the time step.

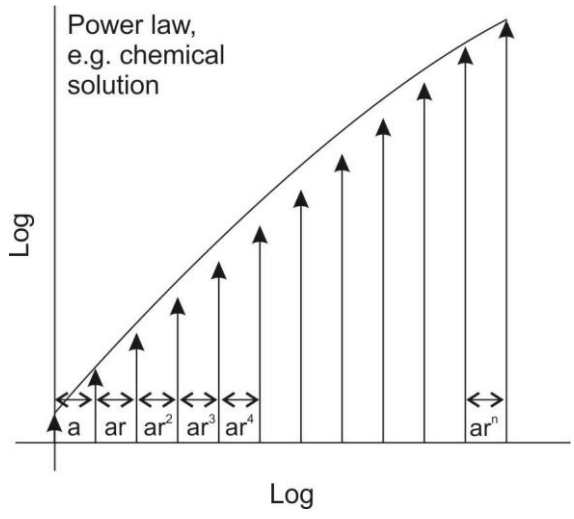

Figure 3-11. Linear approximation on a log-log scale of a non-linear function.

Using this approach it is possible to write:

$$t = a + ar^2 + \cdots ar^n \tag{34}$$

where a, r and n are control variables; a being the size of the initial time step, n being the number of timesteps and r a variable solved below such that equation (35) is satisfied.

Expressed generically for n+1 timesteps this becomes

$$t = \sum_{k=0}^{k=n} ar^k \tag{35}$$

where t is the sum of the sub-time steps. The individual sub-time steps Δt_s being given by

$$\Delta t_s = ar^k \tag{36}$$

where k is an integer from 0 to n.

The sum of a geometrical series for n terms is given as

$$\Delta t_s = a\frac{(1-r^n)}{1-r} \tag{37}$$

This can be expressed as a

$$r^n = -\frac{\Delta t_s}{a}r + \frac{\Delta t_s}{a} - 1 = 0 \tag{38}$$

This non-linear equation can be solved for r using the Newton Raphson method for given values of a and Δt. This approach is used to evaluate n equally-spaced log sub-time steps within a given time step.

The advective transport within the fracture is controlled by the boundary conditions and the distribution of the aperture sizes within the fracture. The flow field is evaluated to provide the advective velocity vectors in each cell. The advective velocity vectors are then used to determine the contribution that each element immediately upstream has on the element under consideration. The element under consideration is termed the “active” element for ease of nomenclature later. This then enables c (equation (33)) to be evaluated for the element. This solution is iterated throughout the fracture surface until a steady state solution is obtained. The concept is illustrated below in Figure 3-12 and the element geometry is given in Figure 3-13.

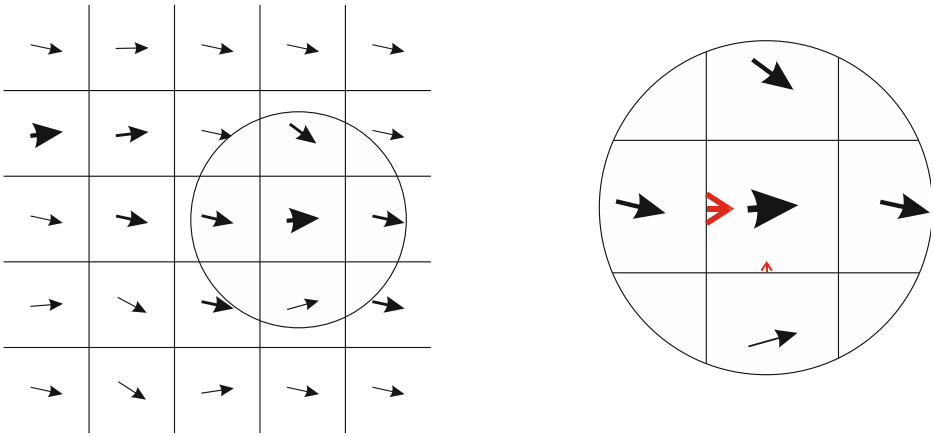

Figure 3-12. Advective velocity vectors used to determine the contribution of upstream elements to current element concentration c_e.

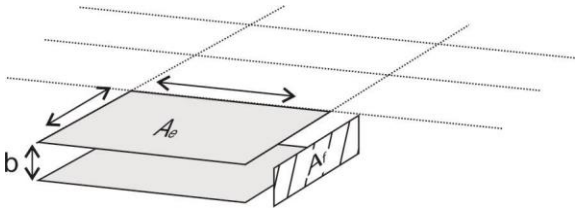

Figure 3-13. Element geometry.

The concentration of the flux (c_{ue}) into the active element from upstream elements (i) is given as a weighted average of the velocity of flow into the element from upstream elements (v_i), the cross-sectional area of these elements (i.e. the fracture apertures) (A_{ft}) and the concentration of flux in the upstream elements (c_i)

$$c_{ue} = \frac{\sum_{i=1}^{i=no.edges} v_i A_{ft} c_i}{\sum_{i=1}^{i=4} v_i A_{ft}} \tag{39}$$

where the cell receives mass from upstream cells.

This is mixed with the volume of fluid in the active element at the start of the time step to give the ion activity product for the active element as

$$c_e = \frac{c_{ue} v_e A_{fe} \Delta t + c_{e(t-1)} A_e b}{f_e} \tag{40}$$

where $v_e A_{fe}$ is the flux of water through the element being considered, A_e is the plan area of the element and b is the fracture aperture. The volume of fluid in the element which comes into contact with the surfaces in a time step is represented by f_e, and v_e is the velocity of the fluid through the element (see equation (41), below).

Sub-time stepping as described above is now used to evaluate the kinetically-controlled change in concentration in the fluid which comes into contact with the fracture surface represented by the active element.

The total volume of fluid that has come into contact with the fracture surfaces represented by the element, in a time Δt, comprising several sub-time steps Δt_s is

$$f_e = v_e \Delta t A_f + A_e b \tag{41}$$

During each sub-time step, first excluding the kinetic terms for clarity, the amount of fracture surface dissolved into the fluid is given by

$$\Delta m_e = 2 k_+ A_e \Delta t_s \alpha_c \tag{42}$$

where α_c is a parameter to take into account the extra surface area available to chemical dissolution as a result of the freshness of the fracture surface, discussed in more detail in Section 3.3.6.

The incremental change in the concentration of the dissolved quartz in the fluid is

$$\Delta c_{e(it)} = \frac{\Delta m_e}{f_e \rho_w} \tag{43}$$

where ρ_w is the water density (kg/m^3). Introducing the kinetic control gives the following

$$\Delta c_{e(it)} = \frac{\Delta m_e}{f_e \cdot \rho_w} \left(1 - \frac{c_{e(t-1)}}{c_s}\right) \tag{44}$$

The initial conditions for the start of the sub-time step iteration (i.e. $t_s = 0$), are $c_{e(t_s-1)} = c_{e(t-1)}$.

The concentration at the end of the sub-time step is given by

$$c_{e(t_s)} = \Delta c_{e(it)} + c_{e(t_s-1)} \tag{45}$$

The sub-time stepping is continued until (35) is satisfied, and the active element flux concentration is updated.

This methodology provides an explicit value for the flux concentration of the active element, and is repeated for every element within the fracture surface (Figure 3-14). However, the final solution of the flux concentration requires an implicit solution including several iterations over all the elements within the fracture surface. This allows changes in the flow field and flux concentrations to be propagated throughout the whole fracture surface. To achieve this, the solution outlined in equations (39) through to (45) is repeated for all the elements until a stable solution within a pre-set minimal tolerance is achieved.

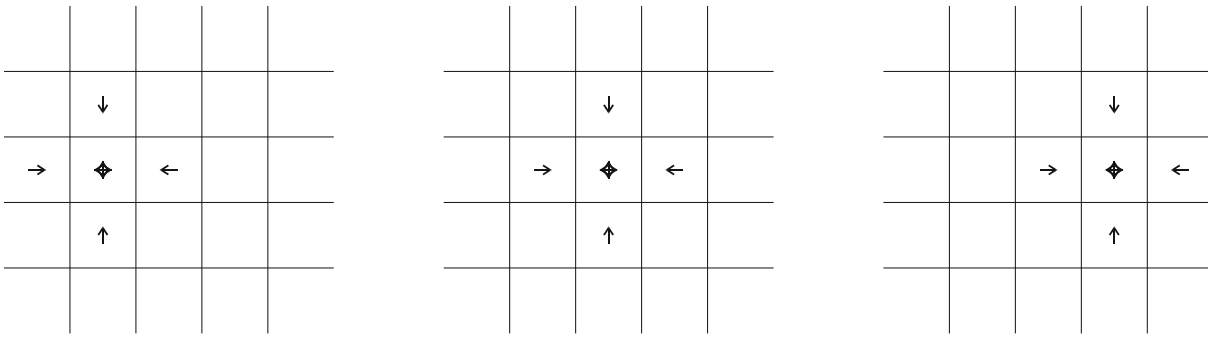

Figure 3-14. The contribution of each element is evaluated in serial and the solution iterated until a steady state solution is calculated.

Using the elements immediately downstream to define the flow contributions to the active element limits the downstream information to one element depth. However, the iteration over the whole fracture surface enables changes in the entire flow system to be taken into account. The advantage of this is that the stream line information (several elements depth) is satisfied, but the only interpretive information required on the behaviour of the flow field at the active element level relates to the flow vectors of the neighbouring elements. This information is readily available.

Using this sub-time stepping approach and the propagation of information across the fracture surface, it is possible to evaluate the advective transport at time steps which would be clearly in violation of the Courant control of advective flow. A simulation time step of 10 hours was used to pick up the main features of the experimental procedure, however a Courant limitation would have required a time step of the order of 10 seconds.

The simulation time saving is significant, as using the standard FE approach would have meant 3600 time steps including a full solution of the advective dispersive transport equations with all the associated stability issues, compared to one time step with sub-time stepping and iteration over a much smaller set of equations in the current approach.

The method was used to match the prescribed geochemical benchmark data with a zero flow field. Further development for consideration will include validation against simplified numerical benchmarks including flow, transport and dissolution.

3.3.5 Approximation of sub-grid scale channel flow

Inclusion of the kinetic control discussed above still produced a quasi-linear response to dissolution. This is considered due to the time frame over which the flow is operating, i.e. even at higher temperatures there is not enough contact time for the fluid in the fracture to demonstrate significant kinetic control. However it is still apparent at 80°C and 120°C that there is a significant non-linear control on the flow through the fracture, Figure 3-15.

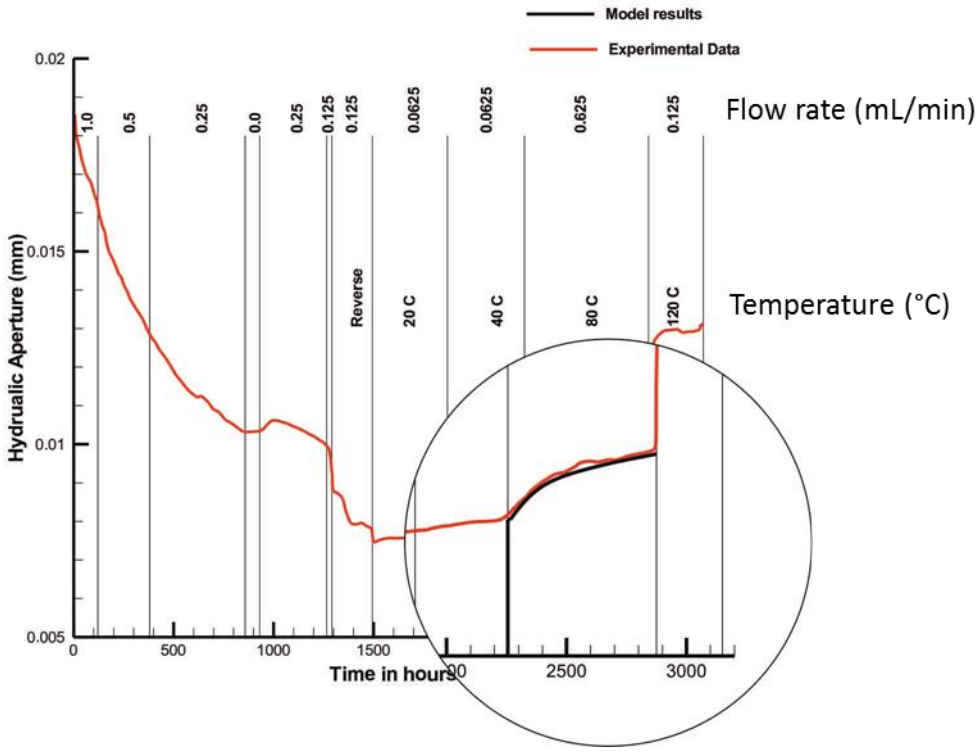

Figure 3-15. Non-linear chemical flow control.

In addition, it is noted that in the experiment the concentration of dissolved SiO_2 over these later phases decreases with time.

The observation is that with time there is a decrease in the rate of increase of the permeability of the fracture system in response to chemical dissolution. Two processes are invoked to explain this observation:

1) The development of channel flow;
2) The reduction in reactive fluid-solid contact area.

In essence both processes could be considered to be the same. In each case the fluid flowing through the fracture removes some solid material, changing the geometry of the contact face with the fluid. In the case of channel flow, it is assumed that the flow causes a contiguous change in the cross-sectional flow area. In the case of reducing contact area the removal of solid material reduces the area available for further dissolution, i.e. a rough surface becomes smoother.

3.3.6 Inclusion of channel flow

Channel flow in fractures is a phenomena which has been studied since the 1980's (e.g. Abelin *et al*., 1994; Barton and de Quadros, 1997; Brown *et al*., 1998; Kalbacher *et al*., 2007; Tsang and Tsang, 1987; Walsh *et al*., 2008). As permeability is controlled by the cube of the aperture (assuming the parallel plate approximation), there is a tendency for natural flow to form channels as the energetically most convenient way of passing through soluble solid

faces. This allows more rapid fluid flow through the rock and leads to reducing amounts of dissolution with time by limiting the contact area of the fluid with the fracture face.

Channels are assumed to form with a cross-sectional flow area much smaller than the 0.8 mm square grid that was simulated explicitly. Simulating the development of channels at 0.8 mm would significantly underestimate their impact, as dissolution of the surface would occur (~linear process), but the corresponding experimentally observed increase in flow rate, which is proportional to the aperture cubed, would not be reproducible. However, the understanding of a fractal surface profile at a sub-grid scale, as discussed earlier, is invoked. To simulate channel flow and the development of preferential flow paths, the dissolution calculated as occurring across the fracture face was redistributed to a limited number of elements within the fracture plane, thereby ensuring there was less of a mismatch between the expected dissolution and the observed increase in flow rate. In practice the fracture plane was divided broadly into a series of slices normal to the flow direction. The amount of dissolution occurring at each of these elements was evaluated, and then the dissolution redistributed in the slices such that the element showing most dissolution collected an extra amount of “dissolution” from the elements showing less dissolution. The total amount of dissolution was kept constant, and the amount redistributed controlled by parameterisation. A certain percentage of the slice cross-sectional flow area was allowed to grow, and also specified as a parameter. The simulation resolution was at a scale of 0.8 mm, with 55 elements comprising a slice, meaning that a minimal channel resolution of ~2% (1/55) of the fracture surface could be represented. In practice to ensure channels developed it was necessary to allow 12% (6/55) of the fracture surface to develop.

Experimentally it is stated (Yasuhara *et al*., 2006) that there was no evidence of channels developing during the experimental work. Numerically the process can be shown to reproduce both the aperture observations and the chemical observations. Evolution of the fracture aperture using the channelling approach outlined above suggests that a very small percentage of the fracture surface area actually controls the fluid flow behaviour, something which may not have been observable with the use of Woods Metal in the experiment.

3.3.7 Inclusion of the changing reactive surface area

It has been shown by all teams in the evaluation of the chemical dissolution of the fracture surface that the dissolution rates are significantly higher than the expected literature values (also discussed in Bond *et al*. 2014). The Surface Area Fitting Parameter α_c in equation (15) is used to take this into account. It was found during parameterisation that the value of α_c could be demonstrably seen to change. This was evaluated for the model as:

1. A function of the cumulative fluid volume which had passed through the fracture, Figure 3-16.
2. A function of the cumulative moles of Si removed from the fracture, Figure 3-17.
3. A function of time, Figure 3-18.

This analysis complements the equivalent comparison performed for the homogenised model, where temperature was considered as a potential factor which might give rise to such scalings.

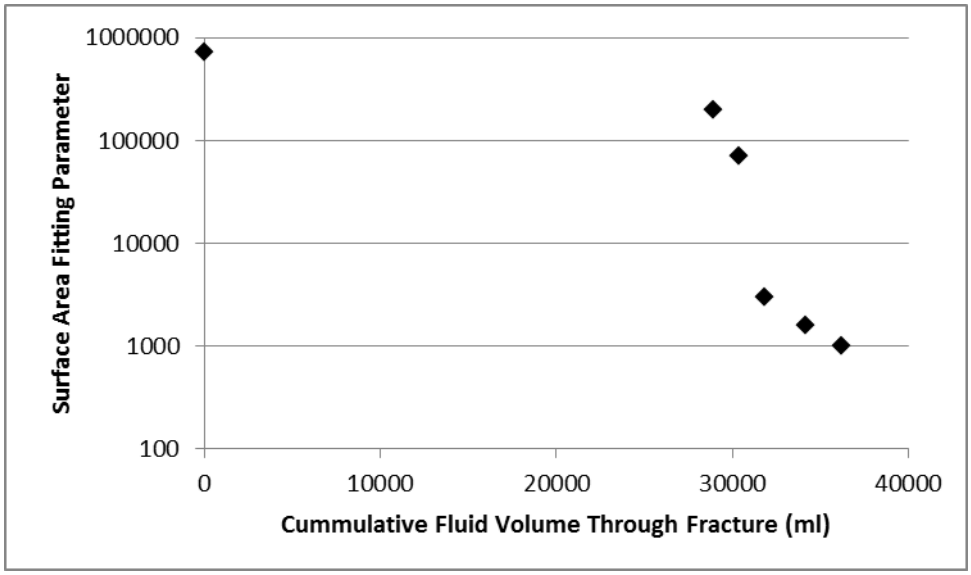

Figure 3-16. Surface area fitting parameter as a function of cumulative fluid volume.

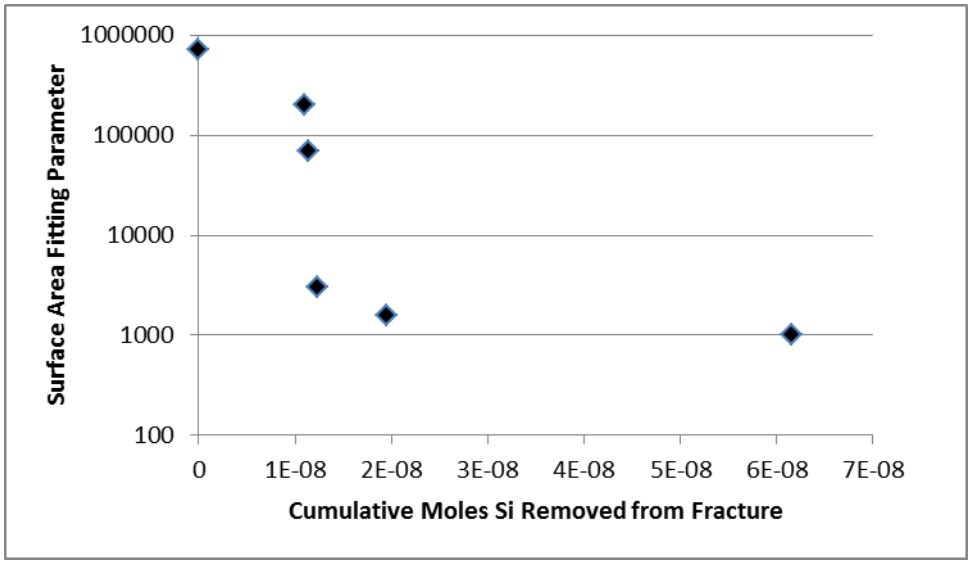

Figure 3-17. Surface area fitting parameter as a function of the cumulative moles of Si removed from the fracture.

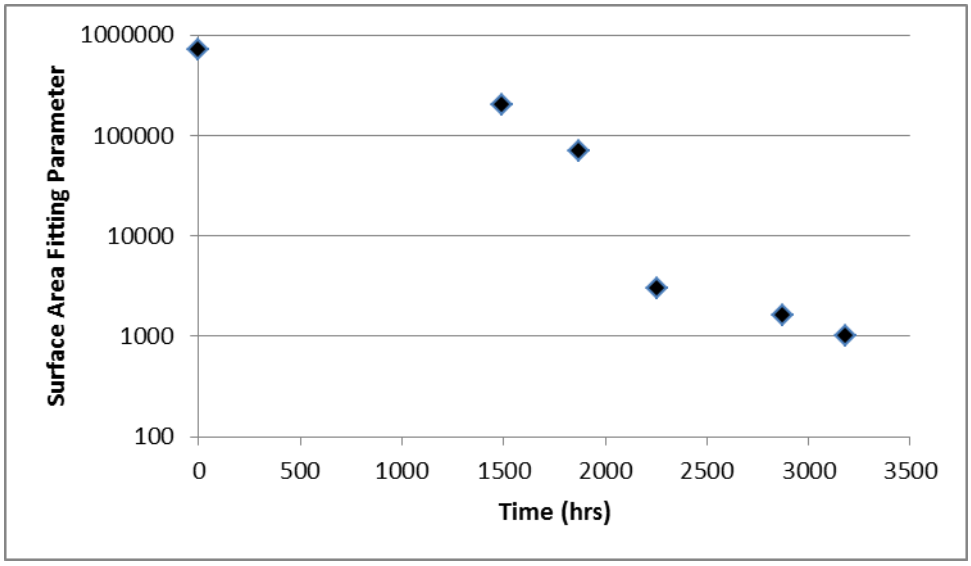

Figure 3-18. Surface area fitting parameter as a function of time.

It is interesting to note that the surface area fitting parameter as a function of time presents the most convincing trend, which effectively states that there is some process that has not been captured that is responsible for the reduction in surface area. However, it may be of note that removing the start point in Figure 3-16 reveals a fairly clear relationship to flow volume, presented below in Figure 3-19.

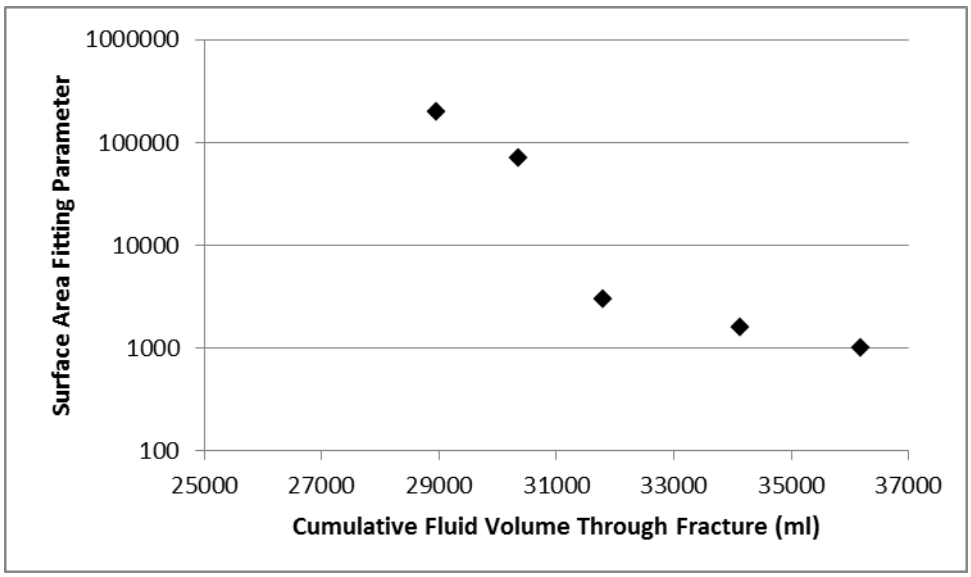

Figure 3-19. Possible relationship of surface area fitting parameter to cumulative fluid volume passing through fracture at later stages.

3.3.8 Discretised Model Summary and Further Work

The discretised modelling approach using OGS has been applied to the whole of the novaculite experiment. The work has shown that it is possible to use the pressure-solution process model, with the addition of a critical stress factor, to represent the evolution of the whole experiment. However, during the non-isothermal period of the experiment it became necessary to reduce the enhanced reactive surface area scaling factor as the experiment progressed in order to obtain a good fit. This factor is opposed to the increase in dissolution rate routinely observed, and implies additional processes are operating that are not well represented in the existing model – this is clearly an area for further investigation and may be illustrative of different spatial scales becoming more or less important (and hence impacting on the reactive surface area) as the fracture surface evolves and the environmental conditions change.

The work has also shown the potential significance in sub-scale channelization in creating the observed curved response in aperture (rather than linear as initially predicted) as the temperature is changed in a stepwise fashion.

In going forward, it seems that attempting to understand the apparent reduction in reactive surface area within a physical and chemical framework should be a priority, and the consideration of the granite experiments may give further insight in this regard to establish whether such effects are peculiar to the novaculite case.

3.4 Step 1 and 2 using the homogenised approach

3.4.1 Stress Corrosion

The Step 0 homogenised models and the Step 1 and 2 discretised models (see previous section) required significant enhancement of the pressure solution process. In particular, the Step 0 homogenised model required a large increase in the pressure solution reaction rate and a reduction of the critical stress.

An alternative process to consider, as raised at the task force workshop in April 2013, is stress corrosion[3]. A model for stress corrosion is presented in Yasuhara and Elsworth (2008), which looks at micro-cracking promoted by stress corrosion (see Figure 3-20).

[3] "In quartz-rich rocks, fracture proceeds through the rupture of Si-O bonds at the crack tip, and this rupture is accelerated when the bonds are strained by external stresses."

– Fundamentals of rock mechanics, 4th edition (Jaeger *et al*., 2007).

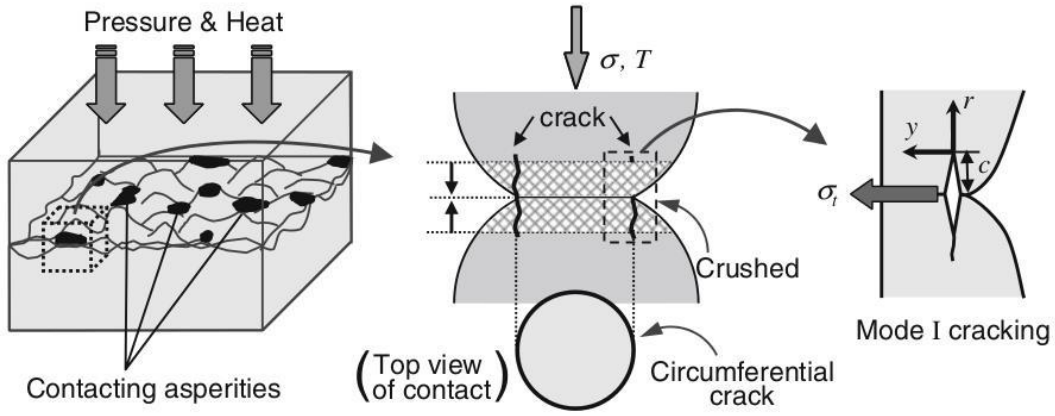

Figure 3-20. Illustration of micro-cracking promoted stress corrosion process from Yasuhara and Elsworth (2008).

Equations (46)-(49) define how stress corrosion relates to an aperture (b) closure rate (from Yasuhara and Elsworth, 2008). The parameters for the various equations are summarised in Table 3-1.

$$\frac{db}{dt} = -(1 - R_c)v_{\mathrm{Si-O}} \quad (46)$$

$$v_{\mathrm{Si-O}} = A_{H2O}\exp\left(\frac{-\Delta H_{H2O}}{RT}\right)\exp(b^*_{H2O}K_I)\left(\theta^{H2O}_{\mathrm{Si-O}}\right) + A_{OH^-}\exp\left(\frac{-\Delta H_{OH^-}}{RT}\right)\exp(b^*_{OH^-}K_I)(\theta^{OH^-}_{\mathrm{Si-O}}) \quad (47)$$

$$K_I \approx \sigma_t\sqrt{2\pi r} \quad (48)$$

$$\sigma_t = \frac{(1-2\nu)}{2}\sigma_a \quad (49)$$

Table 3-1: Details of parameters in stress corrosion equations from Yasuhara and Elsworth (2008, Table 1).

Parameter	Description	Value	Unit
R_c	Contact ratio	From aperture-contact ratio distribution	-
$v_{\mathrm{Si-O}}$	Crack velocity		m s^{-1}
A_i	Pre-exponential factor	A_{H2O} = 1.12×10^{-4} T A_{OH^-} = 2.51×10^{3} T	m s^{-1}
T	Temperature		
ΔH_i	Activation enthalpy	ΔH_{H2O}=6.60×10^{4} ΔH_{OH^-}=8.27×10^{4}	J mol^{-1}
b_i^*	Constant derived from geometry of crack tip for H2O/OH^-	b^*_{H2O}=2.69×10^{-5} $b^*_{OH^-}$=1.78×10^{-5}	N^{-1} $m^{3/2}$
$\theta^i_{\mathrm{Si-O}}$	Fraction Si-O reacting with H2O/OH^-	$\theta^{H2O}_{\mathrm{Si-O}}$ = 0.99921 $\theta^{OH^-}_{\mathrm{Si-O}}$ = 0.00079 (at pH = 7)	-
K_I	Stress intensity factor		N $m^{-3/2}$
r	Infinitesimal crack tip distance	1×10^{-6} – 5×10^{-6}	m
σ_t	Tensile stress		Pa
σ_a	Mean normal stress		Pa
v	Poisson's ratio	0.20	-

3.4.2 Step 1 Model

The Step 0 model is updated for the Step 1 model by replacing the pressure solution process with stress corrosion as described in Section 3.4.1. Since both pressure solution and stress corrosion models calculate an aperture closure rate, the coupling is very similar (as shown in Figure 3-21). The parameterisation is given in Table 3-2.

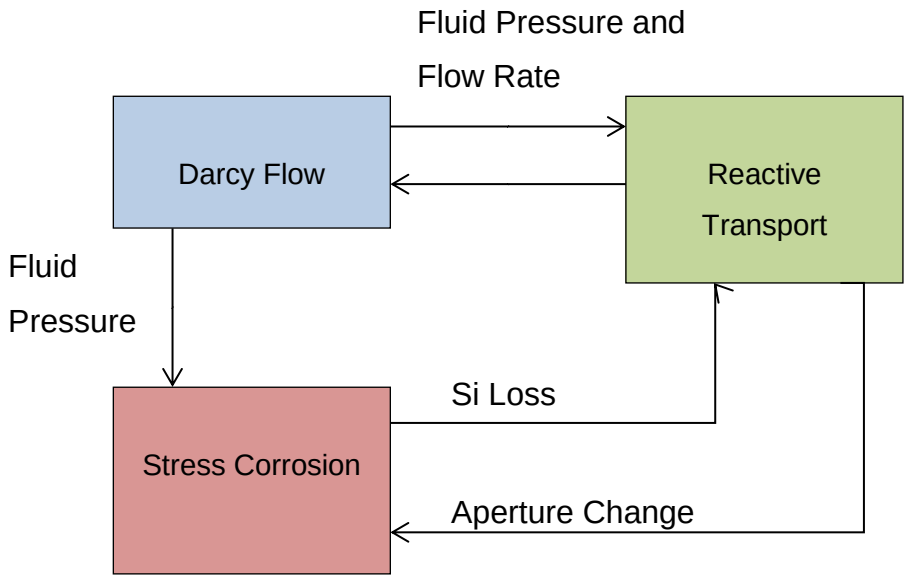

Figure 3-21: Schematic illustration of the coupling in the QPAC Step 1 model.

From Figure 3-22, the initial results of the Step 1 homogenised model (using a 5 μm crack tip distance) show that, with no calibration, stress corrosion does not need as significant an enhancement as was required for pressure solution to produce an aperture closure rate of the right order of magnitude. However, even assuming all quartz enters into solution, the model Si concentration is still low compared to the experiment (Figure 3-23).

Table 3-2: Model constants (excluding stress corrosion parameters listed in Table 3-1).

Parameter	Description	Value	Unit
ρ_w	Density of water	1000	kg m^{-3}
μ_w	Viscosity of water	1.002	mPa s
T	Temperature	20 (during isothermal period)	°C
	Confining stress	1.72	MPa
	Back pressure	345	kPa
V_m	Molar volume of quartz (solid)	22.688	cm^3 mol^{-1}
M_{SiO_2}	Molar mass of quartz	60.0843	g mol^{-1}
M_{Si}	Molar mass of silicon	28.0855	g mol^{-1}
Modified aperture-Contact ratio relationship (original definition in Yasuhara *et al*., 2006)			
b_r	Residual aperture	2.5	µm
b_0	Initial aperture	18.5	µm
R_{c0}	Initial contact ratio	0.02	-
a	Regression curve constant	0.075	-

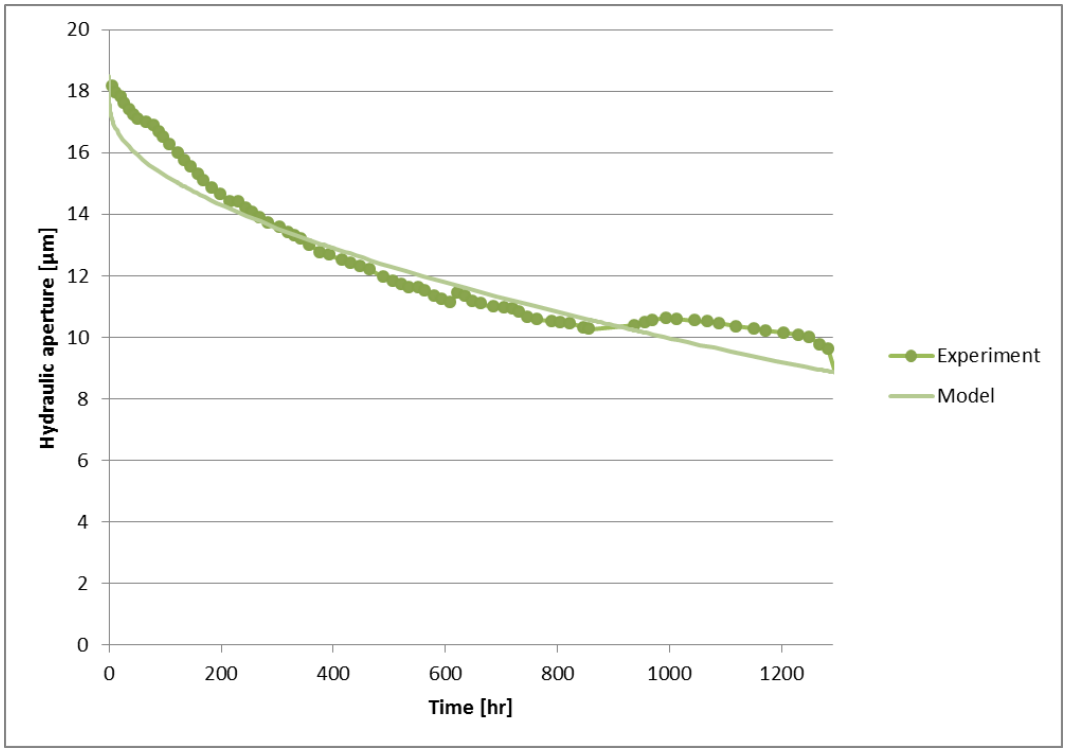

Figure 3-22: Aperture closure from uncalibrated 0D Step1 model (stress corrosion).

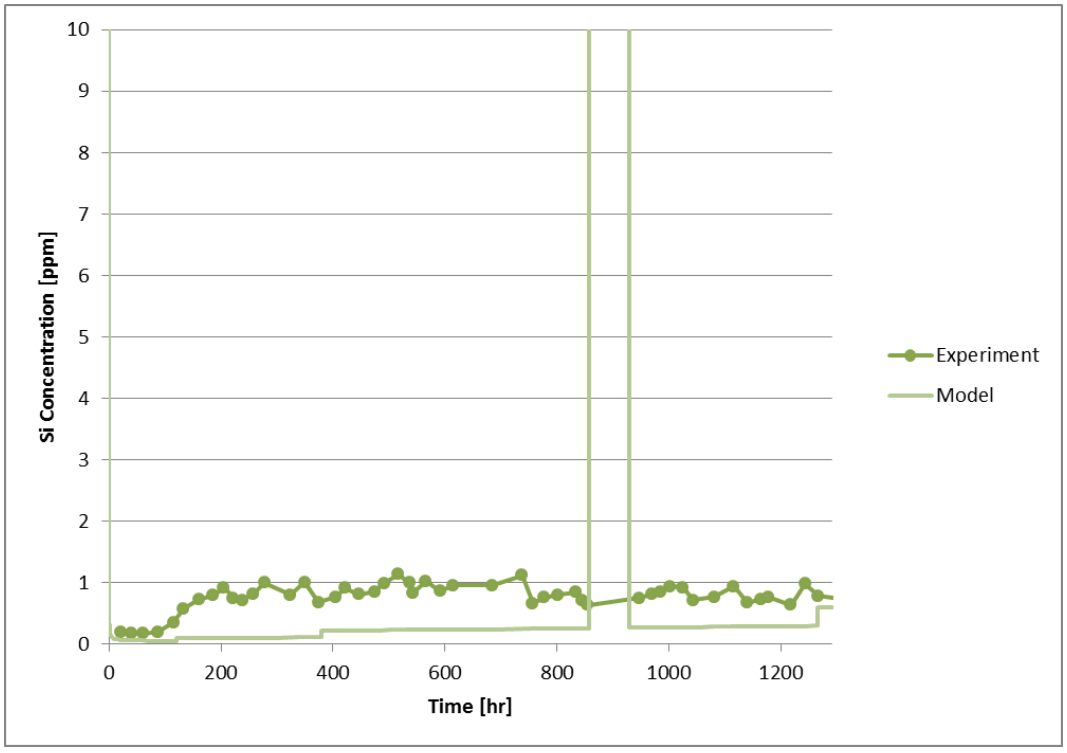

Figure 3-23: Si concentration from uncalibrated 0D Step 1 model (stress corrosion).

Note that the model is sensitive to the infinitesimal crack tip distance (since the stress intensity factor is dependent on this) – for any significant aperture closure to occur with a 1 μm crack tip distance, the initial contact ratio needs to be set as in Yasuhara and Elsworth (2008, Equation 13):

$$R_{c0} = \left(\frac{3\sigma_{eff}\pi(1-\nu^2)}{4E}\right)^{2/3} \quad (50)$$

where E is the Young's Modulus of the rock (MPa) and σ_{eff} is the effective stress (MPa).

The model was calibrated to the experimental data using the 5 μm crack tip distance with an adjusted aperture-contact ratio relationship based on the relationship in Yasuhara *et al*. (2006) with the parameters:

R_{c0} (-)	0.02
a (-)	0.075

Additionally, the stress corrosion process is related to the solubility limit of SiO_2 (to prevent a large jump in Si concentration during the no-flow period), and shut down at the end of the flow reversal period. To reproduce the experimental Si concentration, a 'roughness' factor for free-surface dissolution has been introduced which represents the increase in available reactive surface area with a value of $7x10^5$. The scaling of the dissolution process by such a large factor was a feature of all the task teams' parameterisations (irrespective of the use of stress corrosion or pressure solution) and a similar enhancement factor for pressure solution was required in the discretised modelling (also see Bond *et al*. 2014). Precisely why the dissolution process needs to be enhanced to this degree is unclear, but it was hoped that the non-isothermal results in Step 2 would help constrain the physical understanding of this necessary parameterisation.

The results from running the calibrated model on a coarse 5x6 grid are shown in Figure 3-24, Figure 3-25, and Figure 3-26. Clearly there is a good fit to the experiment, apart from the hydraulic aperture closure and normalised differential pressures during the zero flow period (which is to be expected). Note that unlike the Step 0 model, which calculated the aperture based on porosity, the 2D Step 1 model calculates the net hydraulic aperture from the pressure difference across the fracture, assuming the cubic law; this is why both the hydraulic aperture and normalised differential pressures in the model are affected by the zero flow period.

It is interesting to note that the range of applied normal stresses at the contact points spans 10 MPa – 1000 MPa in the stress corrosion model. The pressure solution critical stress limit, approximately 80 MPa, is within this range, which could mean that pressure solution is still an important process to consider. It is clear from this model and the discretised model that there is a solubility-limited mechanical closure process, and both stress corrosion and pressure solution can be calibrated to fit the experiment data.

It was also found to be possible to obtain very similar results by using higher discretisation grids, or single compartment (1x1; '0D') models. Some parametric adjustment was required at the higher resolutions, but in general the consistency was reasonable.

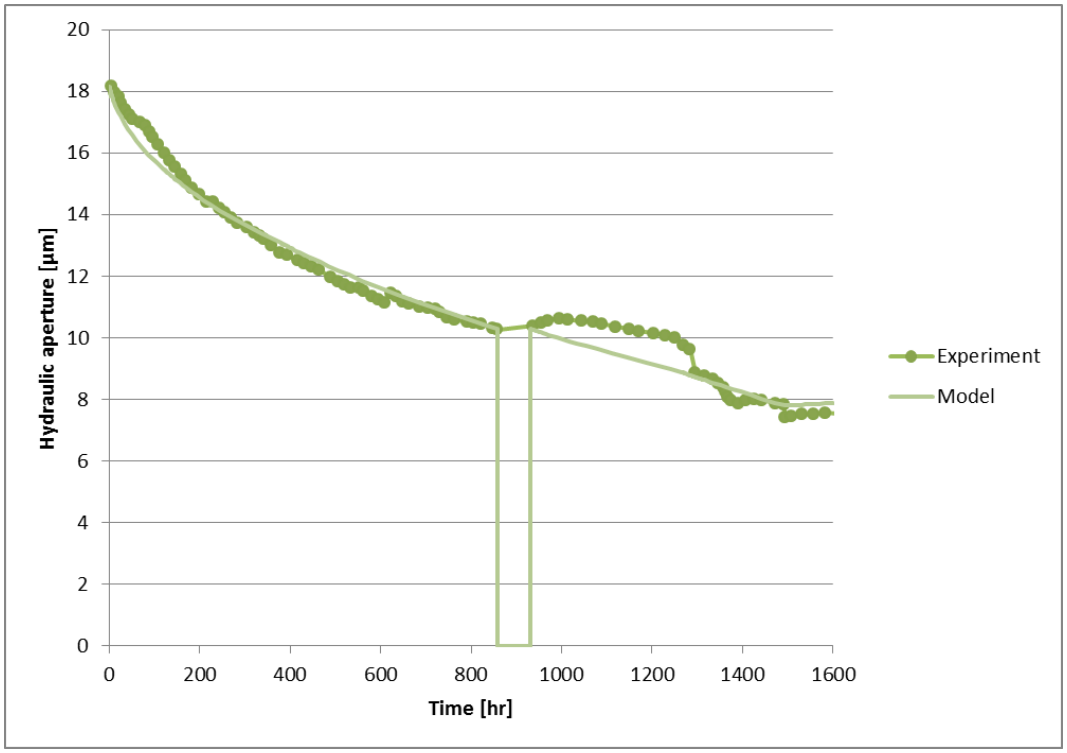

Figure 3-24: Aperture closure from calibrated 5x6 grid Step1 model (stress corrosion).

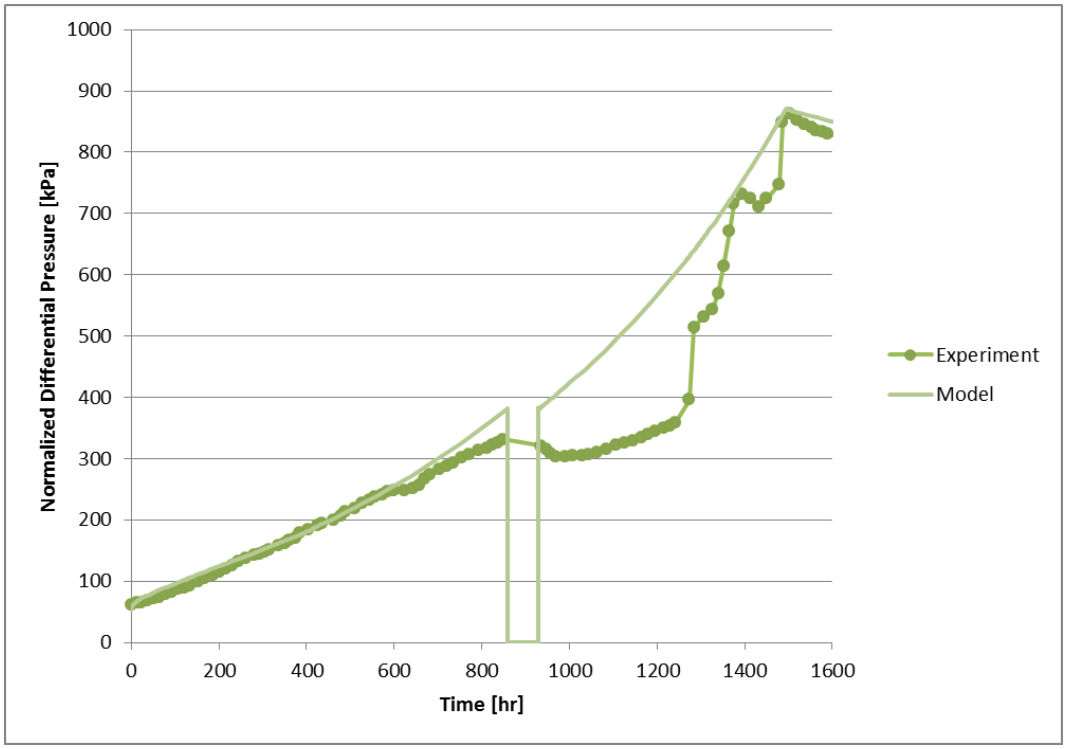

Figure 3-25: Normalised differential pressure from calibrated 5x6 grid Step1 model (stress corrosion).

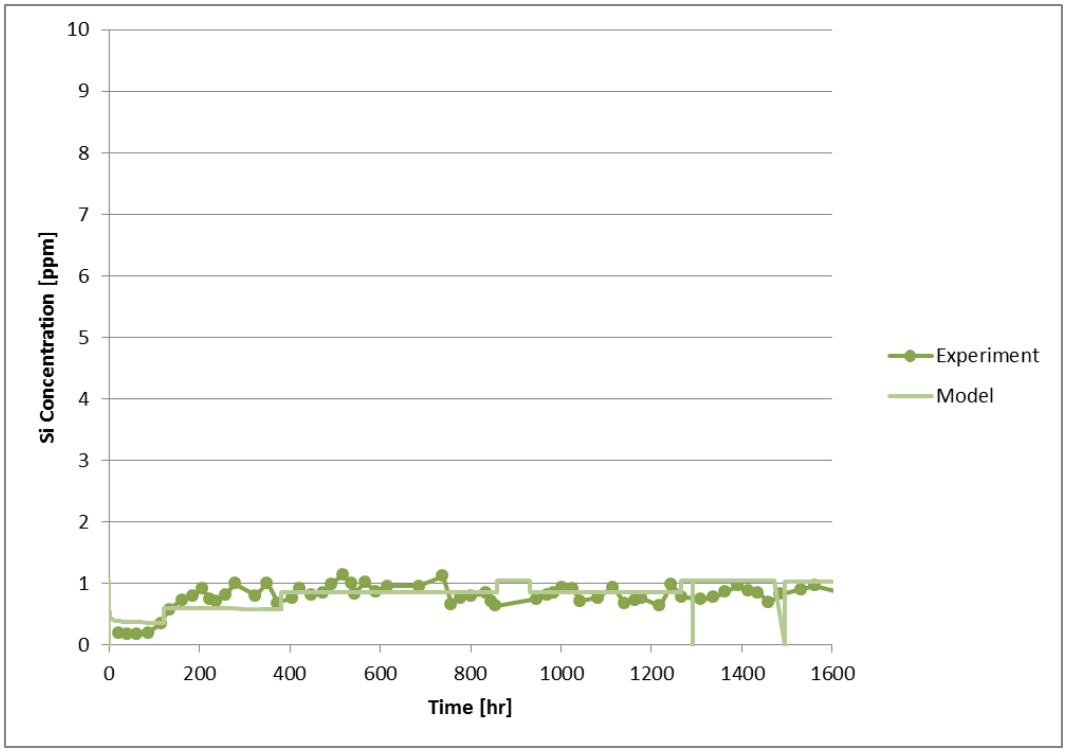

Figure 3-26: Si concentration from calibrated 5x6 grid Step1 model (stress corrosion).

3.4.3 Step 2 Model

In order to facilitate rapid progress and sensitivity checking, the 0D (1x1 grid) homogenised model was modified to run until the end of the experiment period, including the thermal effects.

3.4.3.1 Mechanical Closure Process

The result of running the model with the stress corrosion mechanical closure process used in Step 1 active until the end of the simulation is shown in Figure 3-27, Figure 3-28, and Figure 3-29. Note that this includes the $7x10^5$ 'roughness' factor for free-surface dissolution required in the Step 1 modelling work. It can be clearly seen that this process over-estimates the aperture closure after the flow-reversal period (t > 1494 hrs).

Results of running the model having the stress corrosion process calibrated to shut down after the flow-reversal period are shown in Figure 3-30, Figure 3-31, and Figure 3-32. The aperture closure (and normalised differential pressure) now matches the experimental results more closely, building confidence that this is an appropriate physical representation. Indeed, this is expected from the process-based model discussion in Yasuhara *et al*. (2006), Bond *et al*. (2014) and Section 3.3.

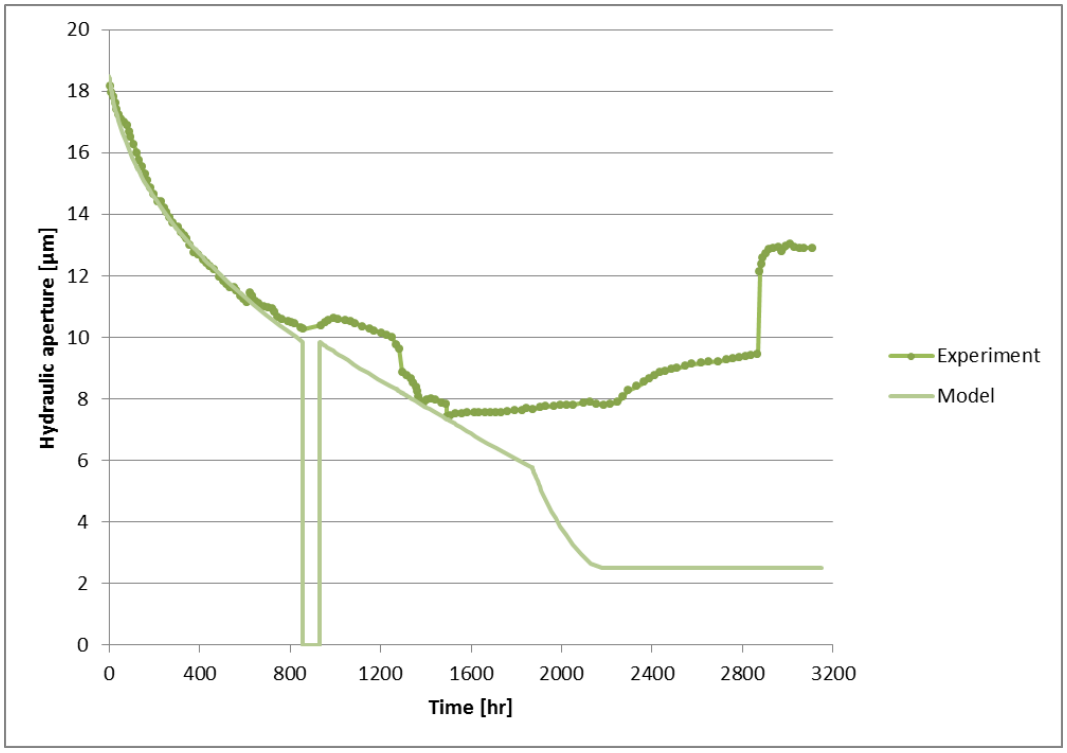

Figure 3-27: Hydraulic aperture closure – stress corrosion process active until the end of the experiment.

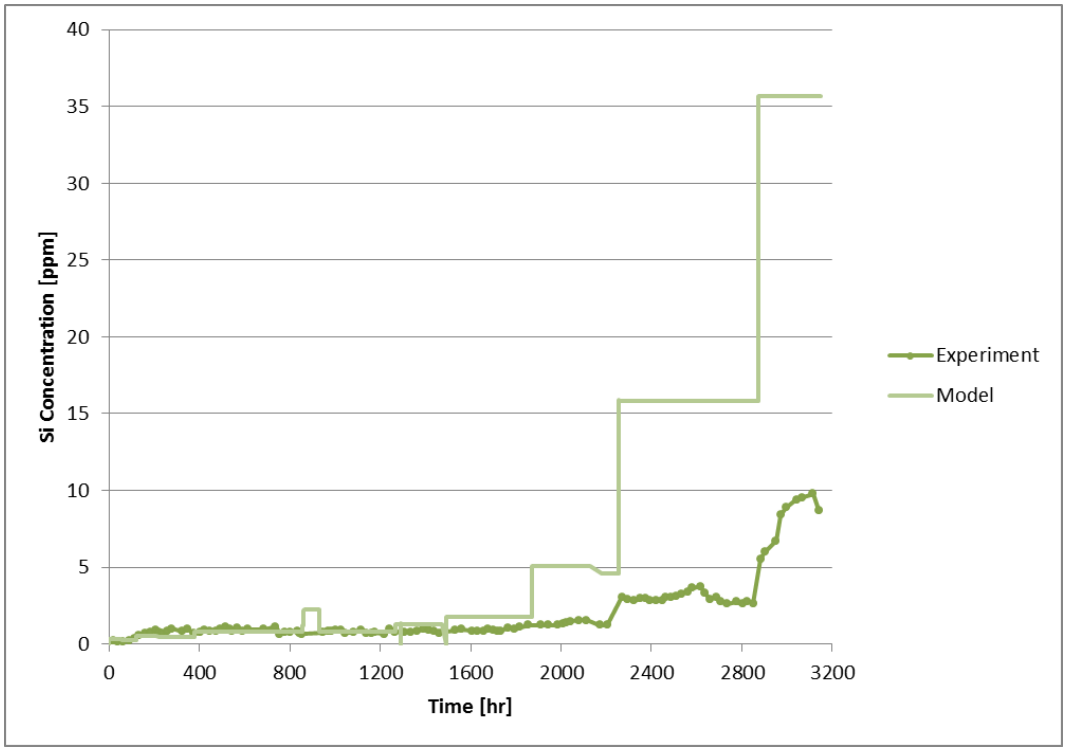

Figure 3-28: Si concentration – stress corrosion process active until the end of the experiment.

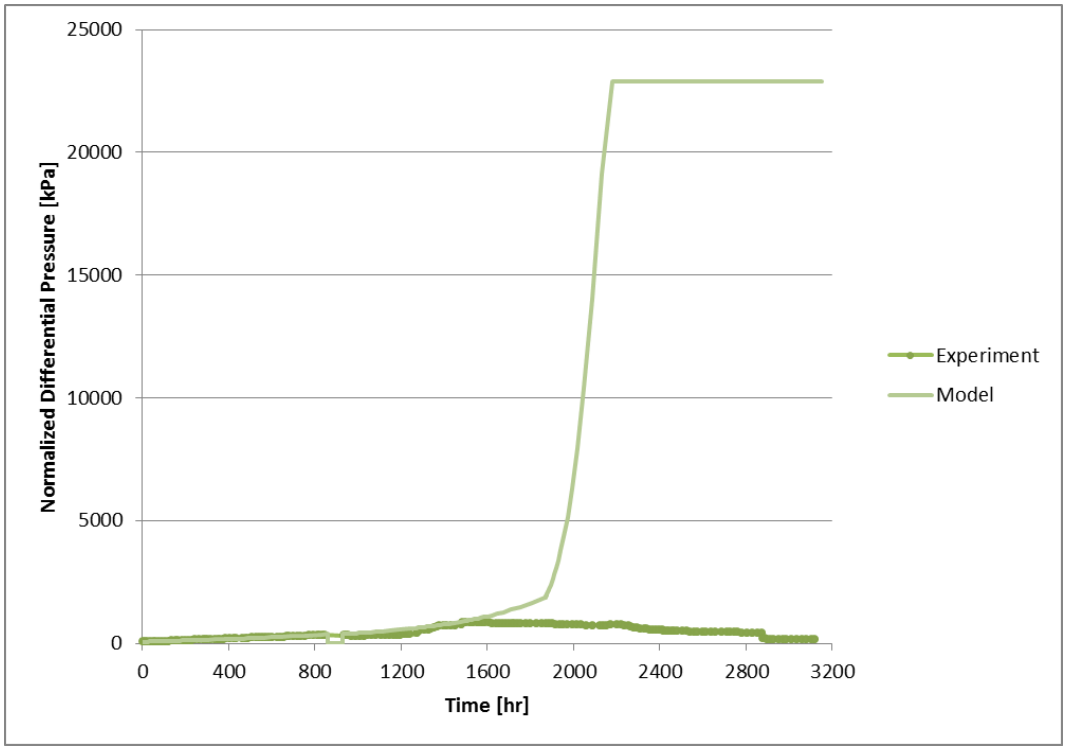

Figure 3-29: Normalised differential pressure – stress corrosion process active until the end of the experiment.

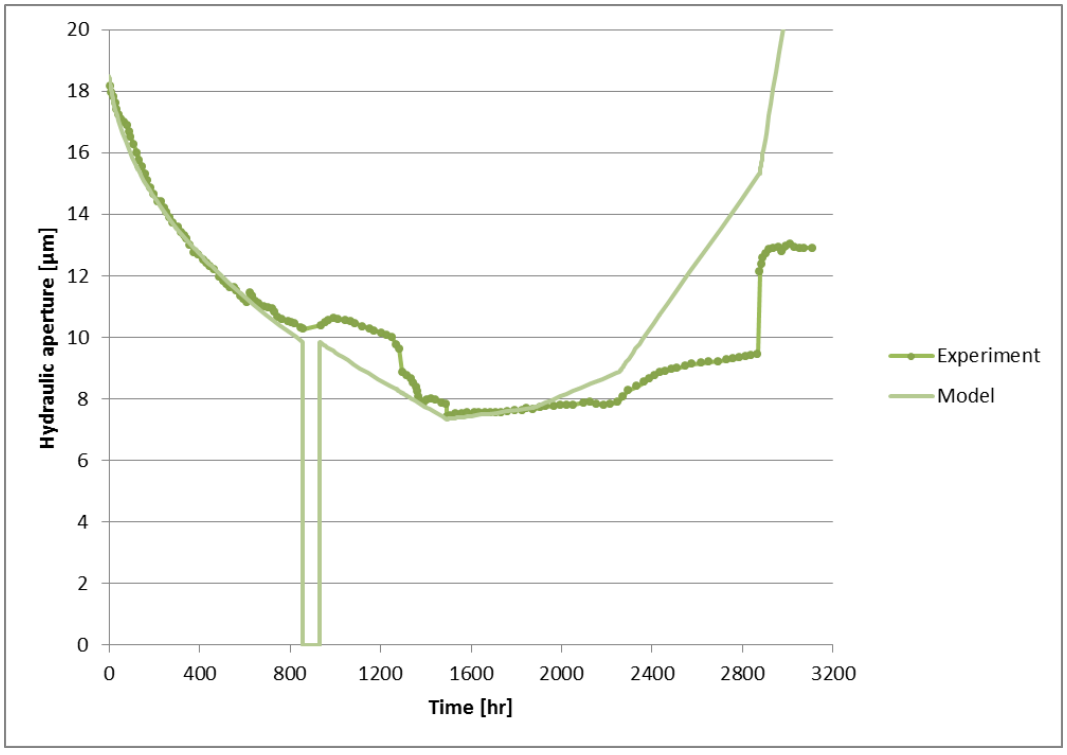

Figure 3-30: Hydraulic aperture closure – stress corrosion process shutdown after flow-reversal.

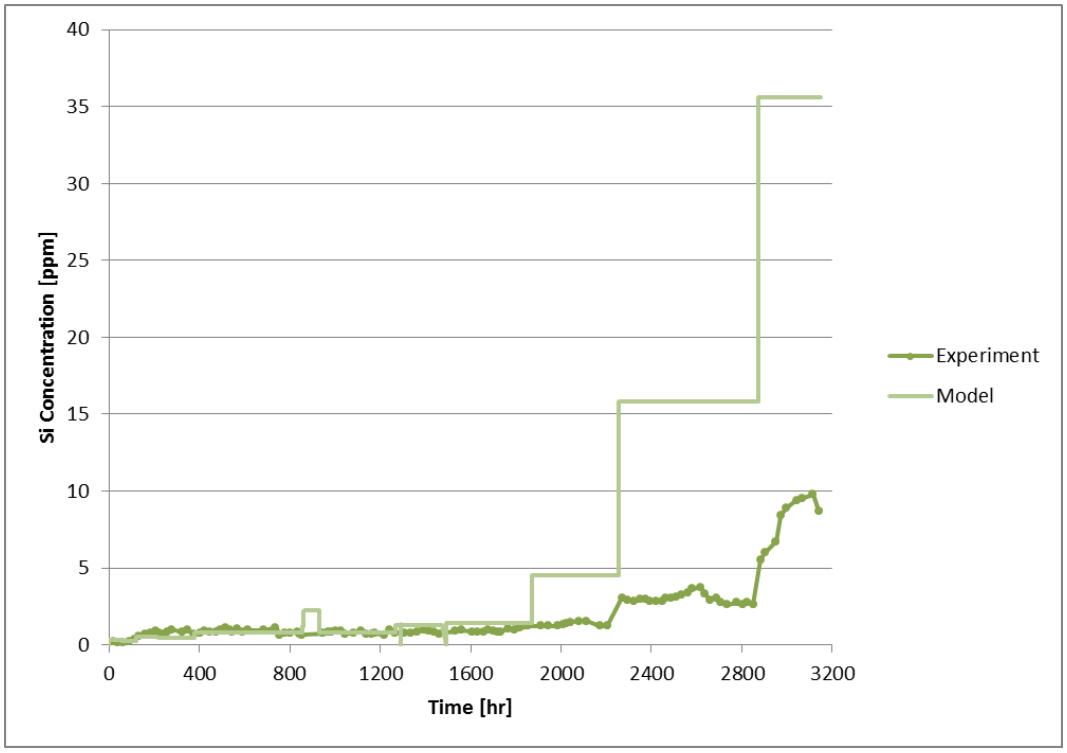

Figure 3-31: Si concentration – stress corrosion process shutdown after flow-reversal.

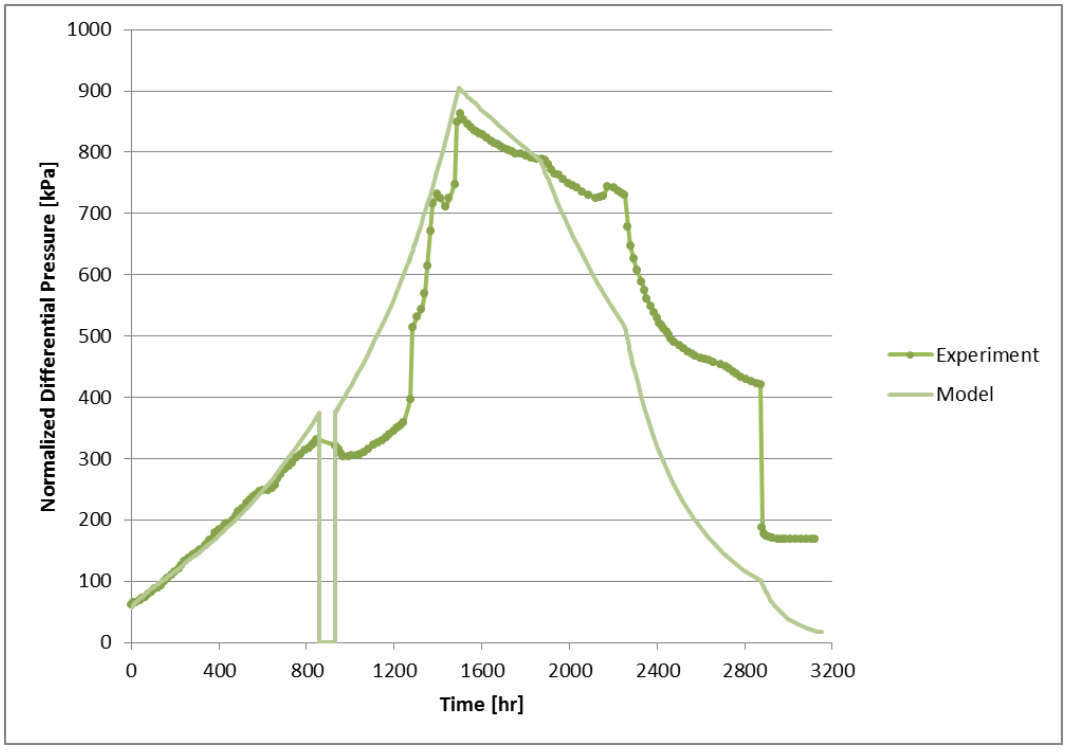

Figure 3-32: Normalised differential pressure – stress corrosion process shutdown after flow-reversal.

3.4.3.2 Reaction Rate Factor

Although the model with stress corrosion shutdown (see Section 3.4.3.1) exhibits a better fit with the experimental aperture closure, Figure 3-31 shows that the Si concentrations are greater at the higher temperatures (40, 80, 120°C; t > 1869 hrs) than the measured concentrations. The aperture change in Figure 3-30 also displays a greater aperture opening than the experimental results. These over-estimations from the model suggest that the 7×10^5 'roughness' factor increases the dissolution rate by too much for modelling the later part of the experiment with the temperature increases. Reducing this roughness factor would improve the later behaviour, but to the detriment of the early time response.

In order to match the experimental Si concentrations, a temperature-dependent reaction rate factor, f_{react} (-), is introduced into the definition of k_0 (mol m^{-2} s^{-1}).

$$k_0 = k_0^{base} f_{react} \tag{51}$$

$$k = k_0 \left(\frac{Q}{K} - 1 \right) \tag{52}$$

The following values for f_{react} match the experimental Si concentrations well:

T (°C)	20	40	80	120
f_{react} (-)	1	0.07	2×10^{-3}	5×10^{-4}

Figure 3-33, Figure 3-34, and Figure 3-35 show the result of running the model using this reaction rate factor, starting the model after the flow-reversal period, with a constant 'roughness' factor as described above. With these values of f_{react}, the aperture change also matches well.

Figure 3-36 illustrates the reaction rate factor values plotted against temperature. The difference between the modified and unmodified quartz dissolution reaction rates are shown in Figure 3-37.

Possible reasons for requiring a temperature-dependent reaction rate factor are:

- The reaction rate requires additional adjustment dependent on temperature. From the size of f_{react} that fit the model to the experiment results (above), this does not fit with the standard Arrhenius relationship for the reaction rate and implies that the rate for higher temperatures is of the same order of magnitude or smaller than the rate at 20 °C.
- The surface area profile for free-surface dissolution could be time- or temperature-dependent. This might reflect enhanced diffusion at higher temperatures effectively decreasing the effective area for dissolution by reducing the importance of very small scale roughness features at or below single grain scale.

Both of these areas have potential for ongoing investigation within DECOVALEX-2015 and may also provide insight into the large scaling factors required to reproduce the experimental results at lower temperatures. It is also possible that there may be an alternative process occurring (i.e. no temperature-dependent reaction rate factor is required). Looking at Figure 3-33 and Figure 3-35, the aperture opening (and normalised differential pressure dropping) rate decreases to an equilibrium (constant opening) at the end of the temperature periods. The work using the discretised model appeared to find a solution to this issue (Section 3.3.6), and implementing an alternative solution suitable for a homogenised representation would be a useful area for future investigation.

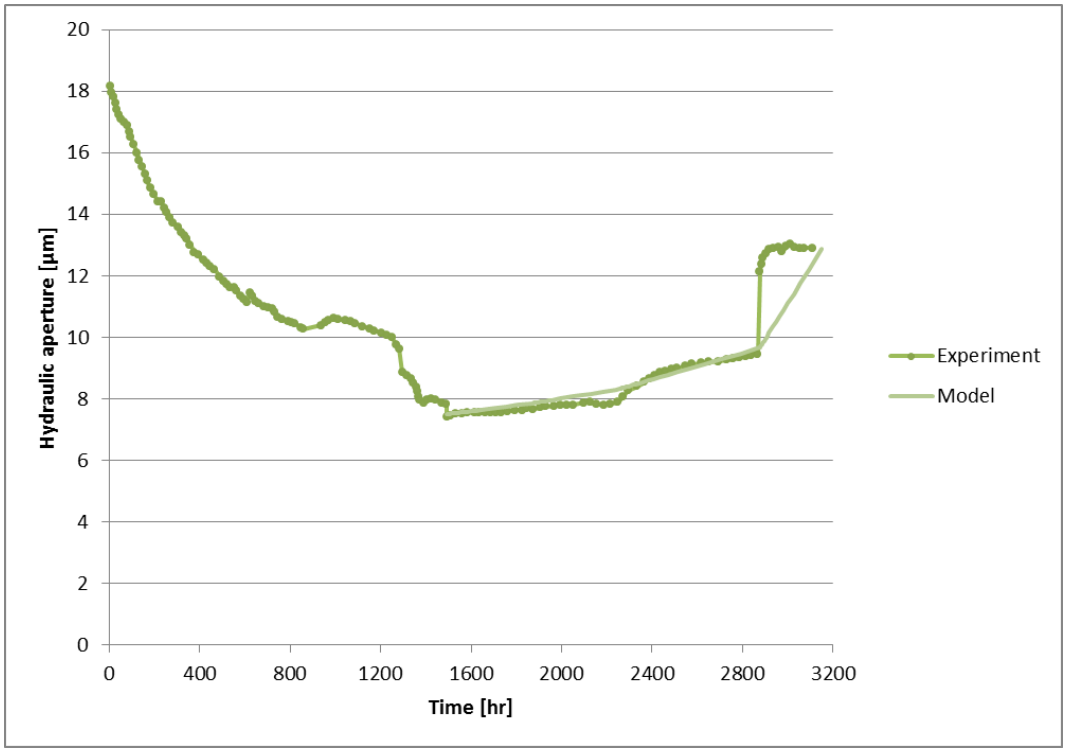

Figure 3-33: Hydraulic aperture closure – dissolution comparison starting after flow-reversal.

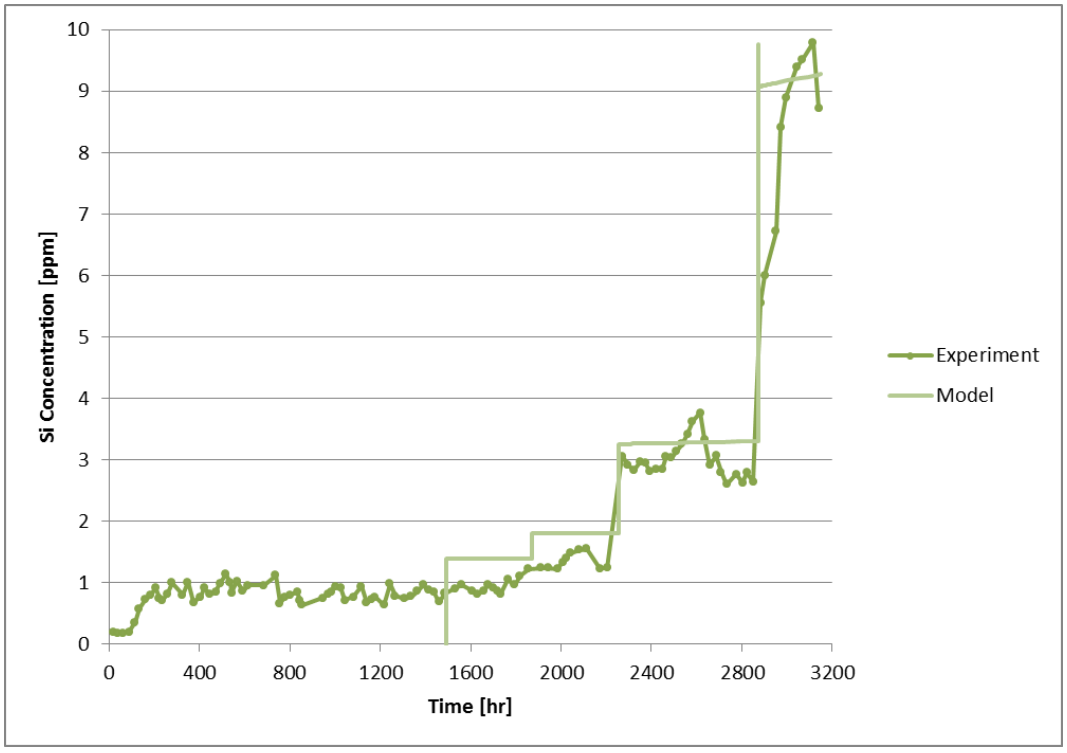

Figure 3-34: Si concentration – dissolution comparison starting after flow-reversal.

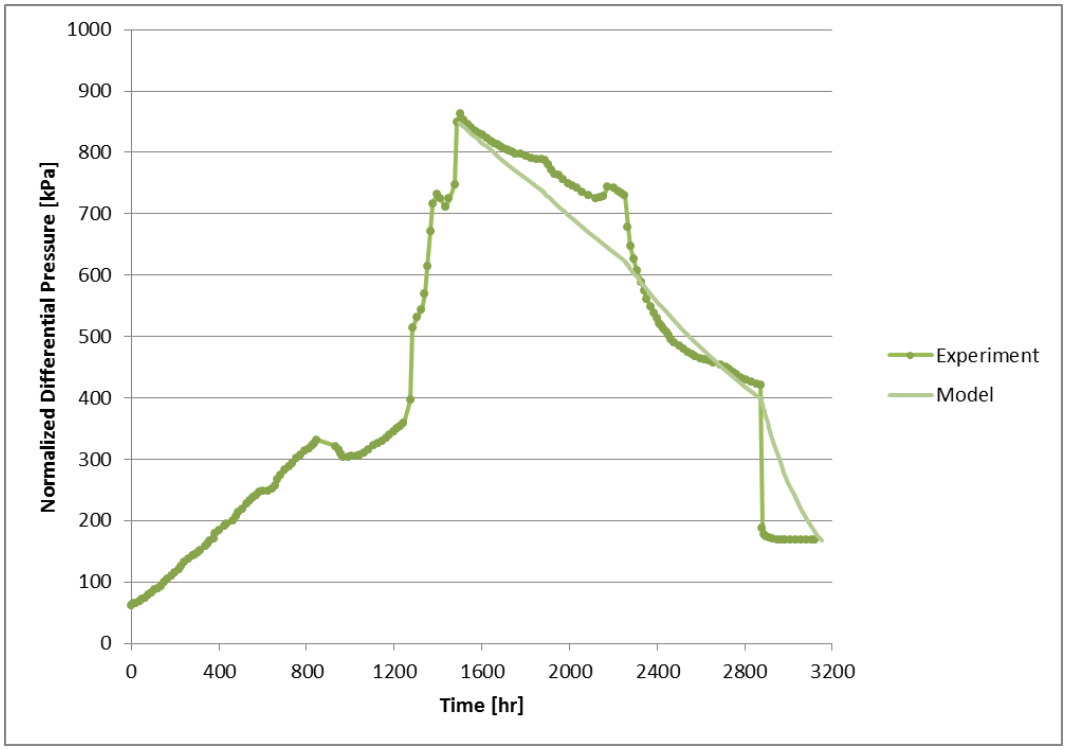

Figure 3-35: Normalised differential pressure – dissolution comparison starting after flow-reversal.

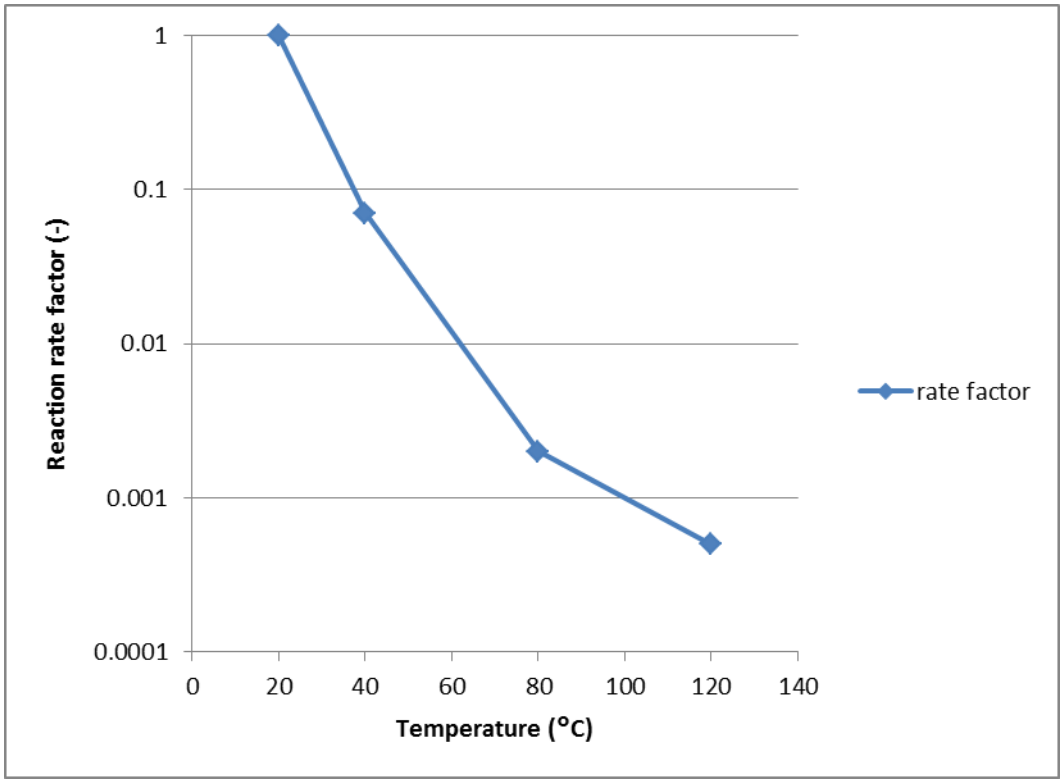

Figure 3-36: Reaction rate factor plotted against temperature.

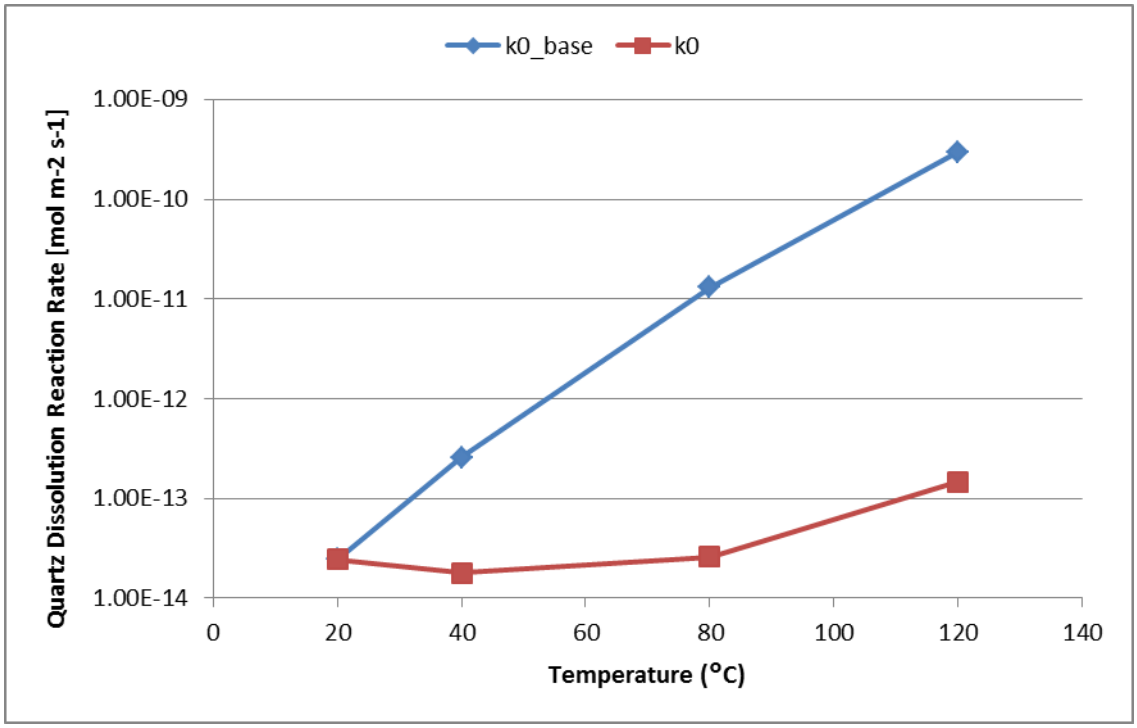

Figure 3-37: Quartz dissolution reaction rate constant including (k0) and excluding (k0_base) the reaction rate factor.

3.4.3.3 Rock Matrix Diffusion

One possible explanation put forward for the large 'roughness' factor required to enhance free-surface dissolution (from Sections 3.4.2 and 3.4.3.2) is that the additional Si concentration, in fact, comes from diffusion out of the rock matrix. To investigate whether this process is significant, the 0D model has been extended with a rock matrix either side of the fracture, as seen in Figure 3-38. In this simple model, the rock matrix consists of five geometrically-sized cells attached to either side of the fracture with an initial height (in the z-direction) of 2 mm, out to a distance of the core sample radius.

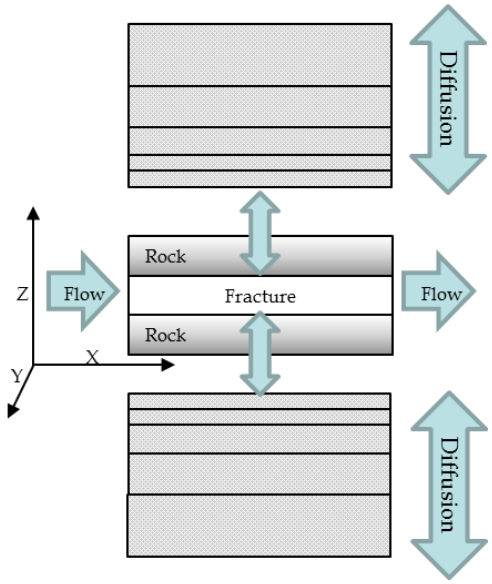

Figure 3-38: Illustration of rock matrix attached to fracture.

The diffusion model used makes the conservative assumptions that: the novaculite is a fully saturated porous medium; temperature changes are instant; and the full core sample radius is available for diffusion. The parameters used for the diffusion model that was implemented using the QPAC Tracer Transport module (Robinson, 2009) are listed in Table 3-3.

Table 3-3: Rock matrix diffusion parameters.

Parameter	Description	Value	Unit
θ	Novaculite porosity	0.01	-
A_{rock}	Rock internal surface area	2.26	$m^2\ g^{-1}$
τ	Tortuosity	0.33	-
D_{pore}	Pore-water diffusion coefficient	1×10^{-9}	$m^2\ s^{-1}$

The model results in Figure 3-39 show that rock matrix diffusion does not appear to be significant at these temperatures for the experimental timescale. However, for higher temperatures and longer time-scales this could be a significant process.

Note that the results presented here are different to some calculations presented by other members of Task C1 (Neretniecks, pers. comm. 2014), where rock matrix diffusion is seen as a more significant process. Investigation into these conflicting results will be carried out going forward as a side task, the significance being as a means to potentially provide an explanation for the required major enhancement of key rates and/or fracture areas in order

to match the experimental data, but the work herein should be regarded as preliminary until the differences are understood.

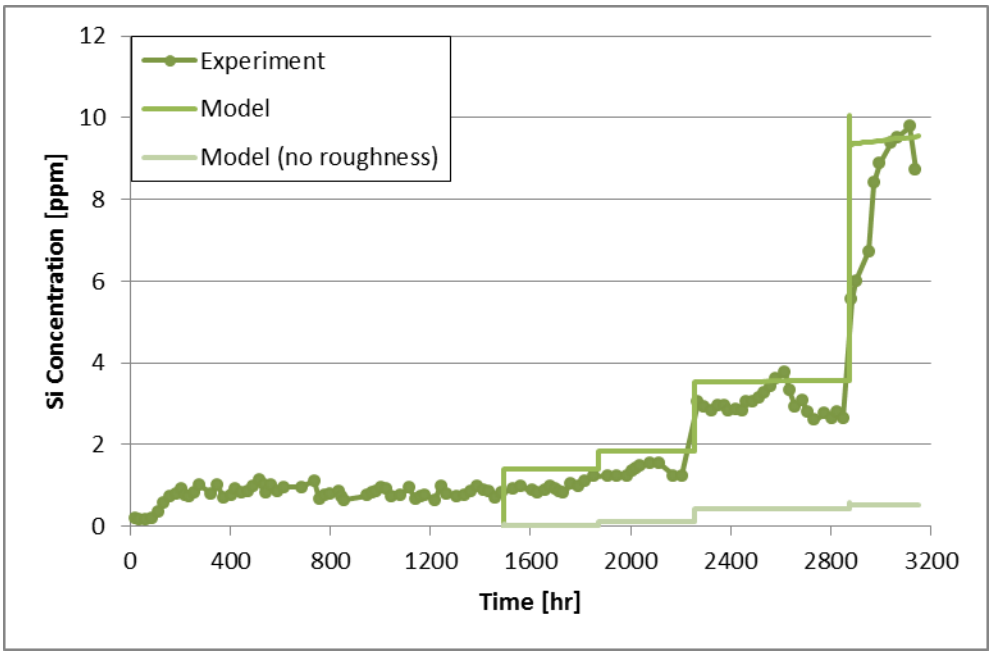

Figure 3-39: Si concentration comparison of the experiment, model using calibrated roughness factors, and model with no roughness factors plus rock matrix diffusion.

3.4.4 Future Work on the Homogenised Model

In the next phase of DECOVALEX Task C1, work will begin on modelling the more geochemically-complex granite experiment (Yasuhara *et al*., 2011). This provides a mechanism to test whether some of the apparently non-physical parameterisations needed to replicate the novaculite experiment are also required for the granite experiment. The novaculite experiment for Steps 0-2 will continue to be considered to resolve any outstanding issues; in particular, the conflicting results on the significance of rock matrix diffusion discussed in Section 3.4.3.3. The aperture-closure processes (pressure solution/stress corrosion) will need updating, where there are multiple minerals.

The granite experiment does not have the same detailed initial surface profile data as the novaculite experiment. In order to model this experiment (and rock fractures in general), a synthetic statistical aperture distribution is required. It is expected that a similar aperture-contact ratio relation as used to model the novaculite experiment needs to be developed on the basis of literature data.

Other components of the model to consider are whether a form of channelization can be implemented in the homogenised models, and the completion of the investigation into the potential importance of rock matrix diffusion, given differing results amongst the task participants.

3.5 More detailed analysis of the fracture topography data

When considering the aperture distribution input to the homogenised and discretised approaches, it was recognised that there was a potential sensitivity to the details of the fracture surface topography data. The laser profilometer data were captured over the area of 89 mm by 45.95 mm on a 50 μm resolution grid (i.e. most, but not all of the surface), with a stated vertical precision of ±10 μm over the duration of the measurement, bearing in mind temperature variations, and 15 μm in the fracture plane. It is also noted in Yasuhara *et al*. (2006) that there is a systematic relative tilt in the topography data that required correction.

Given this observed bias it was decided to analyse the fracture topography data to consider the possibilities and consequences of further bias in the data including:

- Tilt (systematic relative rotation of surfaces in the plane of the fracture);
- Rotation (systematic relative rotation of surfaces out of the plane of the fracture);
- Offset (misalignment of the surfaces in the plane of the fracture).

The possibility of offset over small distances may also come about through the process of initial separation and reassembly of the fracture during the measurement and experimental construction, despite the care taken by the experimentalists in measuring and reassembling the fracture.

An automated 'brute-force' search was conducted by offsetting one surface relative to the other surface by a whole multiple of measurement grid cells in the fracture plane (i.e. multiples of 50 μm), examining the apparent surface difference variance and systematic skews across the profiles in each case. One 'fit', moving the upper surface one measurement grid cell (50 μm) in the negative x-direction, was found to be objectively better than all others, reducing the maximum and minimum difference between surfaces, reducing the variance along profiles across the surface and maximising the visibility of skews in the data. The apparent skew was a simple bilinear feature consistent with the fracture sample not being completely relatively horizontal when measured. The skew correction applied to the top surface was:

$$\Delta z = 1.00265 \times 10^{-4}\, x - 3.5499 \times 10^{-5} y \tag{53}$$

where x, y are the surface coordinates (mm) and Δz is the change in topography to the top surface (mm).

The comparison of the uncorrected offset and offset data with bilinear correction are shown in Figure 3-40. In addition to reducing the range of difference between the surfaces, the application of an offset makes the zero point (no offset between the surfaces has been made in this case, hence a zero value indicates a perfect fit between surfaces) close to the centre of the range of data, allowing the skew along the long axis of the fracture to be visible as well as an apparent radial pattern. Removing the skew (Figure 3-40c) again allows the radial pattern to be visible. Whether this radial pattern is a function of the creation of the fracture, or a reflection of another, smaller scale rotational mismatch between the surfaces is open to interpretation. Making these small changes at the scale of the stated errors of the measurement, clearly improves the 'fit' of the two fracture surfaces.

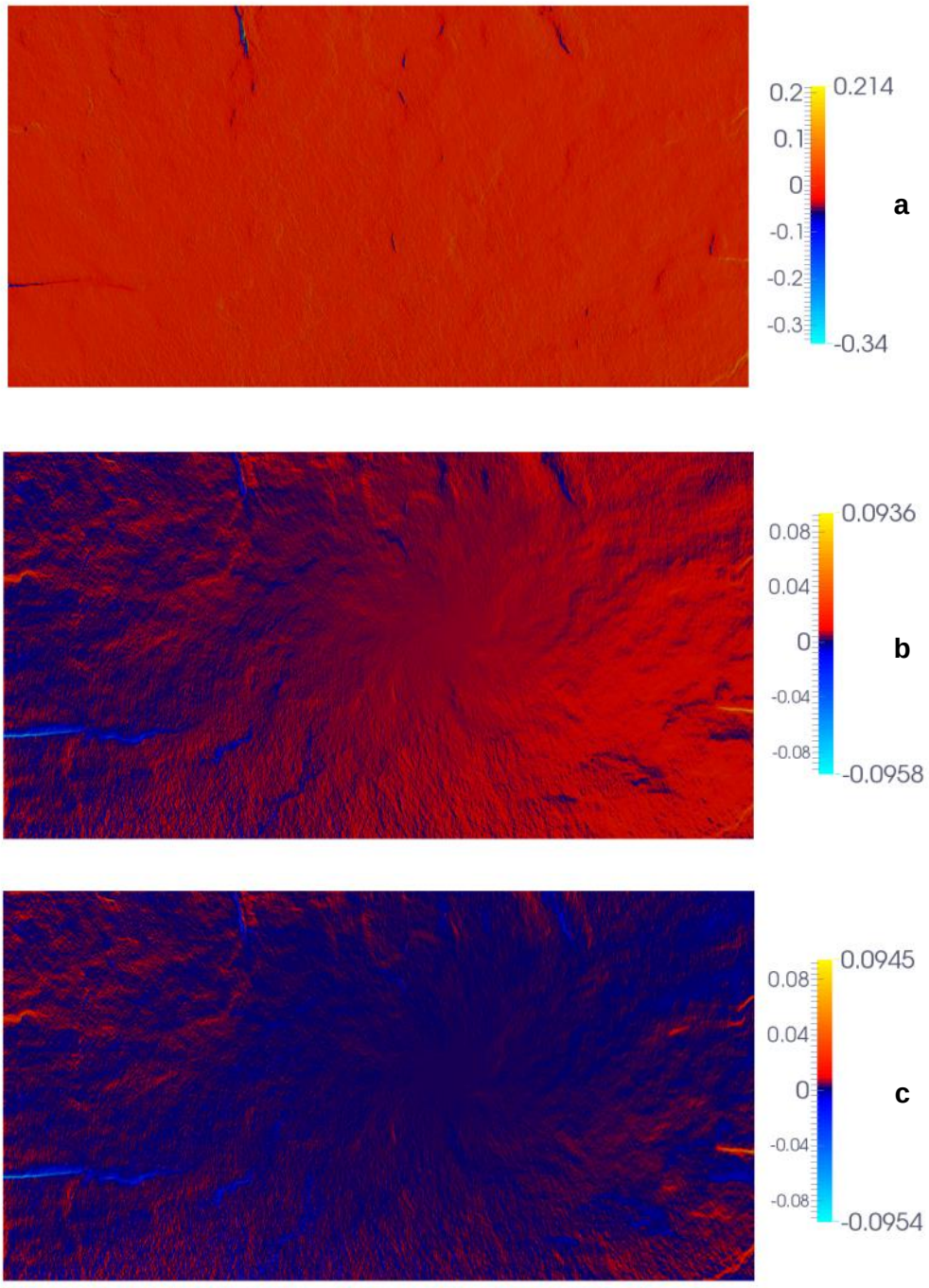

Figure 3-40. Plot of the difference between the top and bottom surfaces (zero datum) with no correction (top - a), offset applied (middle -b) and offset with skew correction (bottom - c). Difference units are mm.

When comparing the effective permeability distributions of the reference data with the corrected data set (having applied an offset between the surfaces to obtain the same net permeability) using the pressure-solution, discretised approach, one can immediately see the corrected data set gives a tighter permeability distribution (Figure 3-41). While this different permeability distribution changed the results significantly, it was found to be possible to recalibrate the model reflecting the difference in contact ratio, reducing the effective rate of pressure dissolution by approximately an order of magnitude (noting this is still small in comparison with the other empirical scaling factors applied to the pressure solution model).

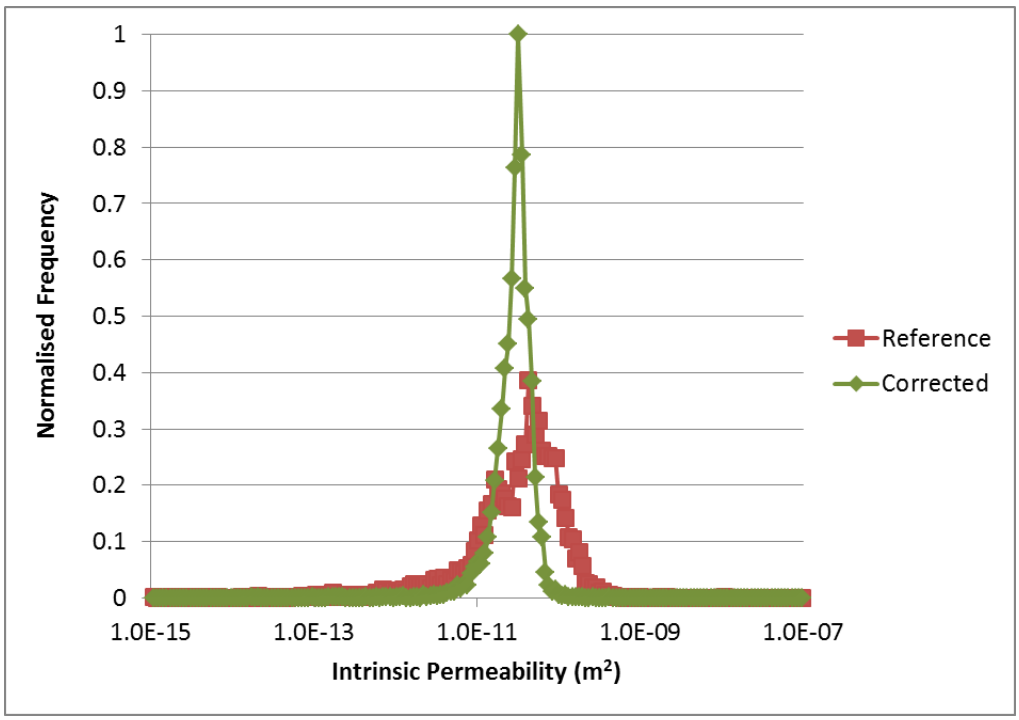

Figure 3-41. Normalised frequency distribution of intrinsic permeability for the reference data set and the corrected data set as corrected to the required initial fracture permeability using the discretised model.

Following this result, it was questioned how useful the profilometer data are in directly deriving the aperture distributions in this case, emphasising the possible importance of statistical, multi-scale representations of the fracture that are based on the experimental data. The discrete data do, however, serve to allow the ongoing investigation of micro-scale processes such as the development of possible channel flow. Other Task members (e.g. Imperial College London and UFZ Leipzig) are actively investigating multi-scale statistical representations of the fracture surfaces and it is hoped that the outcomes from these investigations can be used to inform both the homogenised and discretised approaches.

3.6 Task C1 Summary and Way Forward

Good progress has been made in that both the homogenised and discretised models have been able to replicate the evolution of the novaculite fracture over the entire duration of the experiment. The parallel work has shown that either the stress corrosion or pressure solution physical model can be used to represent the closure of the fracture, and that aqueous dissolution is required to represent the opening of the fracture at later times. Both models agree that at approximately 1500 hours of elapsed experimental time, the fracture reaches a critical state (presumably stress limited) where closure largely ceases. Both models also show that in the non-isothermal period, the rate of increase of dissolution is less than expected and overall the effective area for dissolution has to be reduced at later times and higher temperatures.

The reason for this apparent decrease in effective area at later times is not immediately clear from the data. It seems likely that either the increase in Si diffusivity with increasing temperatures may decrease the apparent roughness (and hence effective area) of the surface or that there may be another time-based process operating. A possible mechanism for the apparent reduction in roughness with enhanced temperature could be due to the increase in diffusion rates with temperature. This has the potential to cause the localised averaging of elevated concentrations adjacent to the rough mineral surfaces being spread over a larger area. This in turn might make the small-scale roughness features become less important as temperatures increase, although without some supporting evidence, this is largely speculation. Overall, this uncertainty appears to be a key area for further work on the novaculite case.

As agreed at the Task C1 task force meeting in Avignon (April 2014), teams who are able to do so are expected to progress onto the granite cases, having done as much work as practicable on the novaculite. Examining the granite gives the opportunity to determine whether similar issues relating to the parameterisation of the process models are also encountered in another set of samples with different mineralogy. This gives an important insight on the potential generality of the issues identified in the novaculite work. Given the position of the two models, the expected contributions from other teams over the next six months and the relative strengths of QPAC and OGS, the following plan for RWM's contribution was agreed:

1) Given the granite experiment has no associated topographic data, so any discretised model would need to use a synthetic topography, the discretised model (OGS) would be best used to attempt to investigate the surface area scaling issues in the novaculite experiment, with the knowledge that other teams (notably Imperial College London and UFZ) would be attempting similar analysis.

2) The homogenised model (QPAC) would be used to move on to the granite experiment, attempting Steps 3 and 4. There would be some ongoing consideration of the possibility of representing some form of small-scale 'channelization' in the homogenised model to improve the fits with the experiment during the non-isothermal phase, as well as further cross-checking of the rock matrix diffusion calculations with other Task participants.

4 Conclusions of the second year of DECOVALEX-2015 work by the AMEC team

4.1 Summary of Progress

Both tasks have progressed well over the last twelve months, meeting the requirements of their respective task schedules with both task leaders acknowledging the useful and high quality input from the RWM team.

Following the discussion of results for Step 1 in Task A, it was revealed that the RWM team was the only team to submit genuinely blind predictions and that those predictions, while not perfect, did bracket the range of response as they were intended to. Given the complexity of the modelling, this is felt to be a significant achievement.

In addition, an 'in-house' variant of the BBM has been developed, implemented in QPAC, which has been extremely instructive in understanding the variation in approaches to hydro-mechanical modelling of bentonite used by the wider scientific community, as well as understanding the experimental data in the task. Such a version of the BBM, and the experience to use it, may be valuable to RWM in future research in the UK context. The Task A work has also produced two novel candidate models for hydro-mechanical modelling of bentonite. These models attempt to simplify the parameterisation of hydro-mechanical models of bentonite by linking the input parameters directly to general empirical data, rather than the BBM approach of adopting a very large number of free parameters which appear to require calibration in nearly every application. Early application of these candidate models to Step 0 and 1 has been promising, but the restricted form of the data under these steps prevents analysis of which of the range of models developed is objectively 'better'.

Under Task A, Step 2 has also been completed. This work, while relatively simple from the process perspective, has nevertheless identified interesting aspects of the WT-1 test, which will have a bearing on modelling a full SEALEX emplacement in Step 3. This work has been excellent preparation for Step 3, but also demonstrated that relatively simple models of complex systems can give rise to useful insights.

For Task C1, Steps 1 and 2 were completed by both the homogenised and discretised modelling approaches. The complementary nature of the modelling has demonstrated value by illustrating that many aspects of the system can be modelled in a simplified sense (for example in a manner that might be suitable for a multiple fracture model), and these results can be cross-checked by additional insights from the discretised model. Both approaches were able to reproduce the experimental results across the whole experimental duration and utilised very similar empirical corrections to the parameterisation in order to adequately represent the fracture during the non-isothermal part of the experiment.

The use of both models also illustrates that there is considerable uncertainty in the aperture closure process, where either pressure solution and stress corrosion processes could be used successfully. Overall the work has illustrated that such models are practicable and useful in understanding physical processes and should make a significant contribution to

further experimental design and conceptual understanding for coupled THMC processes in fractures.

4.2 Issues of Potential Significance to RWM

Following on from the first year of the project, Task A has continued to illustrate the complexity of constructing predictive hydro-mechanical models of bentonite using the currently available range of approaches. Of particular concern is the use of models with a very large number of free parameters (such as the BBM), which are then calibrated to a relatively restricted data set. It has been shown that multiple calibrations to a given data set might exist with such a model, which can manifest in significantly different blind predictions. This outcome shows that, if a disposal concept is sensitive to the accurate prediction of bentonite behaviour, a significant effort in terms of laboratory work to support such predictive models may be required. It is also clear that changes in initial conditions and bentonite composition can all have a significant impact on model parameterisation, so unless RWM uses the same bentonite compositions in a very similar manner to another well-studied case, using data and models directly from the literature may be difficult. Nonetheless, it is likely that 'bounding' calculations can help to establish the likely range of behaviour and may be sufficient in some cases.

However, the work to date has also illustrated that there is potential to simplify these models through various techniques and this may reduce the data needed to sufficiently parameterise a predictive model. Such approaches are as yet unverified and are undergoing development, but if RWM plan to use bentonite within a safety-sensitive role, continued engagement with the wider community of bentonite experimentalists and modellers, as well as maintenance of a capability to understand and develop expertise with bentonite, is likely to be of long-term value to RWM.

Under Task C1, it appears to be the case that it is possible to represent the complexities of THMC interactions in single fractures, but there is considerable uncertainty in which physical-chemical processes are actually operating and the parameterisation to support those processes, especially around apparently simple concepts such as the effective fracture area. At the current level of understanding, it appears clear that additional experimental work and modelling support beyond DECOVALEX-2015 will be required to address these uncertainties, although it is expected that additional insights using the existing data will be obtained over the coming year.

The Task C1 work has also illustrated the difficulty in using topographic fracture data to directly construct aperture maps of a single fracture. While the topography data might be useful to construct statistical representations of the topography and aperture, the direct use of such data to attempt to directly evaluate aperture in experiments should be considered very carefully with respect to the experimental design, and hence the likelihood that the derived data, when used in this manner, are likely to be representative. The work has also illustrated that (assuming the process uncertainties can be reduced), simplified THMC representations across multiple fractures may be practicable, subject to the typical concerns around the physicality of discrete fracture network representations (Black *et al*. 2007).

4.3 Way Forward

For Task A it is planned that the next step will be attempted using the range of models developed thus far in an attempt to make an objective judgement as to which gives the best

representation, bearing in mind the complexity of the input and hence the data burden required to support each model. Over the next year it is expected that the candidate models which tie the hydraulic and mechanical representation more closely together (ILM and non-linear elastic) will have been tested against Step 3 and if possible, other data from the literature. More minor work is also planned against Step 2 to attempt to resolve some of the remaining uncertainties with that experiment, especially regarding the hydraulic behaviour of the open test hole, which may have implications for other experiments.

For Task C1 it is planned to split effort between attempting to resolve the process uncertainties with the novaculite experiment using the discretised model in OGS and moving forward to examine the granite case using the homogenised model in QPAC.

5 References

Abelin, H., Birgersson, L., Widen, H., Agren, T., Moreno, L., and I. Neretnieks. (1994). Channeling experiments in crystalline fractured rocks: *Journal of Contaminant Hydrology*, v. 15, no. 3, p. 129-158.

Barton, N., and E. F. de Quadros. (1997). Joint aperture and roughness in the prediction of flow and groutability of rock masses*: International Journal of Rock Mechanics and Mining Sciences*, v. 34, no. 3–4, p. 251-252.

Brown, S., Caprihan, A., and R. Hardy. (1998). Experimental observation of fluid flow channels in a single fracture: *Journal of Geophysical Research - Solid Earth*, v. 103, no. B3, p. 5125-5132.

Biot M.A. (1965). *Mechanics of Incremental Deformation.* John Wiley & Sons, Inc., New York/London/Sydney.

Black J.H., Barker J.A. and N.D. Woodman. (2007). An investigation of 'sparse channel networks' Characteristic behaviours and their causes. SKB Report R-07-35.

Bond, A.E., Thatcher, K.E., Chittenden, N., McDermott, C., and A. Fraser-Harris. (2014). NDA RWMD Participation in DECOVALEX-2015. First Annual Report for DECOVALEX Tasks A and C1. AMEC report 18040-TR-002 v2.0, Quintessa report QRS-1612A-R1-v2.0.

Bond, A. E. (2013a). A mechanical module for QPAC. Quintessa Report QRS-QPAC-MECH-1 v1.0.

Bond, A. E. (2013b). Specification for DECOVALEX-2015: Task C1. Steps 0, 1 and 2. Quintessa Report to the DECOVALEX-2015 Project. QRS-1612B-S-0-1v1.4.

Courant, R., Friedrichs, K., and H. Lewy. (1928). Über die partiellen Differenzengleichungen der mathematischen Physik: *Mathematische Annalen*, v. 100, no. 1, p. 32-74.

CoRWM (2009). Report on National Research and Development for Interim Storage and Geological Disposal of Higher Activity Radioactive Wastes, and Management of Nuclear Materials. Committee on Radioactive Waste Management Report to Government. CoRWM document 2630.

Department for Environment, Food and Rural Affairs (Defra), Department for Business, Enterprise and Regulatory Reform, Welsh Assembly Government, and Northern Ireland Department of the Environment (2008). Managing Radioactive Waste Safely: A Framework for Implementing Geological Disposal. Cm 7386, ISBN 0101738625.

Department of Energy and Climate Change (DECC) (2014) Implementing Geological Disposal: A Framework for the long-term management of higher activity radioactive waste. URN 14D/235

Dueck, A. (2004). Hydro-mechanical properties of a water unsaturated sodium bentonite, Laboratory study and theoretical interpretation, PhD thesis, Lund Institute of Technology, Sweden. ISBN 91-973723-6-6.

Eyring, H. (1935). The Activated Complex and the Absolute Rate of Chemical Reactions: *Chemical Reviews*, v. 17, no. 1, p. 65-77.

Gens, A., & Alonso, E. E. (1992). A framework for the behaviour of unsaturated expansive clays. *Canadian Geotechnical Journal*, *29*, 1013–1032.

Houlsby G.T. (1985). Use of a variable shear modulus in elastic-plastic models for clays. *Computers and Geotechnics* 1: 3-13.

IRSN (2012). Task A: The SEALEX in-situ experiments. Presentation at 2nd DECOVALEX-2015 Workshop, Leipzig, given by J-D Barnichon, IRSN.

Jacinto, A. C., Villar M. and A Ledesma. (2012). *Geotechnique* 62, No. 8, 657–667.

Jaeger J.C., Cook N.G.W. and R Zimmerman. (2007). Fundamentals of Rock Mechanics (4th edition). Wiley-Blackwell 488pp.

Kalbacher, T., Mettier, R., McDermott, C., Wang, W., Kosakowski, G., Taniguchi, T., and Kolditz, O. (2007), Geometric modelling and object-oriented software concepts applied to a heterogeneous fractured network from the Grimsel rock laboratory: *Computational Geosciences*, v. 11, no. 1, p. 9-26.

Kristensson, O. and Åkesson, M. (2008), Mechanical modeling of MX-80 – Quick tools for BBM parameter analysis. *Physics and Chemistry of the Earth* 33, S508–S515.

Kolditz, O., S. Bauer, L. Bilke, N. Böttcher, J. O. Delfs, T. Fischer, U. J. Görke, T. Kalbacher, G. Kosakowski, C. I. McDermott, C. H. Park, F. Radu, K. Rink, H. Shao, H. B. Shao, F. Sun, Y. Y. Sun, A. K. Singh, J. Taron, M. Walther, W. Wang, N. Watanabe, Y. Wu, M. Xie, W. Xu and B. Zehner. (2012). "OpenGeoSys: An open-source initiative for numerical simulation of thermo-hydro-mechanical/chemical (THM/C) processes in porous media." Environmental Earth Sciences 67(2): 589-599.

Kröhn K-P. (2003). New conceptual models for the resaturation of bentonite. *Applied Clay Science*. *23, 1-4,* 25-33.

Likos, W. J., and Lu, N. (2006). Pore-scale analysis of bulk volume change from crystalline interlayer swelling in Na+ and Ca^{2+} smectite. *Clays and Clay Minerals*, *54*, 515-528.

Millard, A. and Barnichon, J-D. (2013). DECOVALEX D-2015: description of Task A (SEALEX experiment): Version 2 - Steps 0 and 1.

Millard, A. and Barnichon, J-D. (2014). DECOVALEX D-2015: description of Task A (SEALEX experiment): Version 5 – Step 2.

Millard A., Barnichon J-D., Mokni N., Thatcher K., Bond A. and R. Blaheta. (2014). Modelling benchmark of a laboratory test on hydro-mechanical behavior of bentonite. *Proceedings of UNSAT-2014*. In-press.

NDA (2012). Geological Disposal: RWMD Approach to Issues Management. Nuclear Decommissioning Authority Report NDA/RWMD/081 Version 1 March 2012, Harwell.

Quintessa (2013). QPAC: Quintessa's General-Purpose Modelling Software. QRS-QPAC-11. http://www.quintessa.org/qpac-overview-report.pdf.

Revil, A. (1999). Pervasive pressure-solution transfer: A poro-visco-plastic model: Geophysical Research Letters, v. 26, no. 2, p. 255-258.

Rutqvist J., Ijiri Y. and H. Yamamoto. (2010) Implementation of the Barcelona Basic Model into TOUGH–FLAC for simulations of the geomechanical behavior of unsaturated soils. LBNL Paper LBNL-4209E.

Rutqvist J., Ijiri Y. and H. Yamamoto. (2011). Implementation of the Barcelona Basic Model into TOUGH–FLAC for simulations of the geomechanical behavior of unsaturated soils. *Computers and Geosciences* 37:751-762.

Robinson, P. C. (2009). A tracer transport module for QPAC. Quintessa Report QRS-QPAC-TTM-1 v1.0.

Stewart D.I., Studds P.G. and T.W. Cousens. (2003). The factors controlling the engineering properties of bentonite-enhanced sand. *Applied Clay Science* 23:97–110.

Taron, J., Elsworth, D. and K.B. Min. (2009) .Numerical simulation of thermal-hydrologic-mechanical-chemical processes in deformable, fractured porous media. *International Journal of Rock Mechanics and Mining Sciences*. Volume 46, Issue 5, Pages 842–854.

Tsang, Y. W., and C. F. Tsang. (1987). Channel model of flow through fractured media: *Water Resources Research*, v. 23, no. 3, p. 467-479.

Walsh, R., C. McDermott and O. Kolditz. (2008). Numerical modeling of stress-permeability coupling in rough fractures. *Hydrogeology Journal* 16(4): 613-627.

Wang Q. (2012). Hydro-mechanical behaviour of bentonite-based materials used for high-level radioactive waste disposal. PhD Thesis, Université Paris-Est.

Wang Q., Tang A. M. , Cui Y., Delage P., and B. Gatmiri. (2012). Experimental study on the swelling behaviour of bentonite/claystone mixture. *Engineering Geology* 124 59-66. DOI : 10.1016/j.engeo.2011.10.003.

Wang, Q., Tang, A.M., Cui, Y.J., Delage, P., Barnichon, J.D., and Ye, W.M. (2013). The effects of technological voids on the hydro-mechanical behaviour of compacted bentonite-sand mixture. *Soils and Foundations*, Vol. 53(2): 232–245.

Yasuhara, H., Elsworth D. and A Polak. (2004). Evolution of permeability in a natural fracture: Significant role of pressure solution. *Journal of Geophysical Research*, Vol. 109, B03204.

Yasuhara H. and D. Elsworth. (2008). Compaction of a rock fracture moderated by competing roles of stress corrosion and pressure solution. *Pure and Applied Geophysics*, vol. 165, no. 7, pp. 1289–1306.

Yasuhara, H., Polak, A., Mitani, Y., Grader, A., Halleck, P., and D. Elsworth. (2006). Evolution of fracture permeability through fluid-rock reaction under hydrothermal conditions. *Earth and Planetary Science Letters* 244: 186–200.

Yasuhara, H., Kinoshita, N., Ohfuji, H., Lee, D. S., Nakashima, S., and , K. Kishida. (2011). Temporal alteration of fracture permeability in granite under hydrothermal conditions and its interpretation by coupled chemo-mechanical model. *Applied Geochemistry* 26: 2074–2088.

AMEC
Registered Address:
Booths Park
Chelford Road
Knutsford
Cheshire
WA16 8QZ